UNIVERSITÀ
DEGLI STUDI
DI PADOVA

Sede Amministrativa: Università degli Studi di Padova
Dipartimento di Ingegneria Industriale

Scuola di Dottorato di Ricerca in Ingegneria Industriale
Indirizzo: Ingegneria dell'Energia
Ciclo XXVII

VARIABLE SPEED ROTOR HELICOPTERS: OPTIMIZATION OF MAIN ROTOR – TURBOSHAFT ENGINE INTEGRATION

Direttore della Scuola : Ch.mo Prof. Paolo Colombo

Coordinatore d'indirizzo: Ch.ma Prof.ssa Luisa Rossetto

Supervisore: Ch.mo Prof. Ernesto Benini

Dottorando: Gianluigi Alberto Misté

Zwei Dinge erfüllen das Gemüt mit immer neuer und zunehmenden Bewunderung und Ehrfurcht, je öfter und anhaltender sich das Nachdenken damit beschäftigt: Der bestirnte Himmel über mir, und das moralische Gesetz in mir.
(Immanuel Kant)

Sommario

I rotori a velocità di rotazione variabile (*Variable Speed Rotors*, VSR) rappresentano un argomento di ricerca innovativo per lo sviluppo di nuove configurazioni di velivoli a decollo verticale, quali l'elicottero o il convertiplano. La possibilità di modificare la velocità di rotazione del rotore principale, in funzione della specifica condizione di volo, permette di ottenere prestazioni ottimali e significative riduzioni del consumo di carburante. Tuttavia, le problematiche connesse all'impiego di una velocità di rotazione variabile sono numerose e richiedono un approccio di analisi interdisciplinare. Il presente studio si configura come il primo esempio in letteratura di analisi prestazionale eseguita con simulazioni accoppiate rotore e motore turbo-albero per un modello di VSR.

Due strumenti di simulazione sono stati implementati al fine di effettuare la suddetta analisi accoppiata: un codice di simulazione di turbomotori a gas (TSHAFT) e un software per la stima dell'assetto e delle prestazioni di un elicottero (TCOPTER). La validità del concetto di rotore a velocità variabile è stata testata su un caso reale: a tale scopo i modelli di un elicottero UH-60 Black Hawk e di un motore turbo-albero GE T700 sono stati implementati e sottoposti a validazione su dati sperimentali. Successivamente, si è proceduto alla costruzione di una routine di ottimizzazione capace di individuare le velocità ottimali del rotore, in funzione delle diverse condizioni di volo dell'elicottero; tali velocità corrispondono alla condizione di minimo consumo di carburante.

Sono state analizzate a livello puramente prestazionale due differenti tipologie di VSR: la prima contempla l'utilizzo di una trasmissione tradizionale a rapporto di riduzione fisso (*Fixed Ratio Transmission*, FRT); la seconda prevede l'impiego un'ipotetica trasmissione a variazione continua (*Continuously Variable Transmission*, CVT). Nel caso FRT, poiché le velocità di rotazione della turbina e del rotore principale sono in un rapporto fisso, la velocità ottimale è stata calcolata come il miglior compromesso tra la velocità ottimale del rotore principale e quella della turbina. Nel caso CVT, invece, lo studio è stato effettuato assumendo che le velocità di rotore e turbina fossero libere di ruotare alle rispettive velocità ottimali.

Diversi casi di simulazione sono stati analizzati, al fine di quantificare i benefici legati alla possibilità di operare alla velocità ottimale del rotore in

funzione delle condizioni di volo, dell’altitudine e del peso dell'elicottero. L'accoppiamento del modello dell'elicottero e del modello di motore turbo-albero è risultato determinante per un’adeguata individuazione della velocità corrispondente a consumo minimo. La massima riduzione nei consumi di carburante è stata stimata attorno al 13%.

Infine, sono state studiate possibili soluzioni progettuali in grado di apportare ulteriori margini di miglioramento a elicotteri operanti con VSR. In particolare, è stato effettuato un tentativo di riprogettazione preliminare della turbina di potenza del GE T700 con l’obiettivo di incrementarne l’intervallo di funzionamento a massima efficienza. In sostanza si è cercato di rendere le prestazioni della turbina meno sensibili alle variazioni nel numero di giri, cercando di estendere la zona di rendimento massimo attorno al punto di progetto.

Abstract

Variable speed rotors (VSRs) represent an innovative research field for the development of new rotorcraft designs. The possibility to change the rotational speed of a helicopter rotor, as a function of the specific flight condition, makes it possible to achieve optimum performance and relevant fuel consumption reductions. However, issues related to employing a main rotor variable speed are numerous and require an interdisciplinary approach. The present study represents the first effort in the open literature aimed at understanding the performance implications of coupling helicopter trim and turboshaft engine simulations for a VSR model.

A gas turbine simulation code, TSHAFT, and a helicopter performance tool, TCOPTER, have been implemented in order to be able to carry out the coupled analysis. Following this, the VSR concept has been tested on a real helicopter case: the models of a UH-60 Black Hawk helicopter and a GE T700 turboshaft engine have been implemented and validated against experimental data. Subsequently, an optimization routine has been employed to find the optimal main rotor speeds which minimize fuel consumption in different helicopter flight conditions.

Two different approaches to VSRs have been analyzed: the former employing a traditional fixed ratio transmission (FRT), the latter assuming a continuously variable transmission (CVT). In the FRT case, since the turbine and main rotor speeds are in a fixed ratio, the optimal speed has been calculated as the best compromise between optimal main rotor speed and optimal turbine speed. In the CVT case, the study has been carried out assuming that main rotor and turbine speeds were free to rotate at their optimal speeds.

Different simulation cases have been analyzed in order to quantify the benefits related to the optimal main rotor speed depending on flight conditions, altitude and helicopter gross weight. It has been found that coupling both the helicopter and engine model is important to adequately determine the correct rotational speed corresponding to minimum fuel consumption. More than 13% fuel saving has been shown to be feasible.

Finally, possible improvements to the VSR concept have been studied. In particular, a trial has been made to redesign the power turbine of the GE T700 in order to improve the efficiency of the engine in a wide speed variation range.

Contents

List of Figures

List of Tables

Nomenclature

Latin Symbols

A	Main rotor disk area
b	By-pass ratio
c	Chord length
C_d	Drag coefficient
C_l	Lift coefficient
C_m	Meridional flow velocity
c_p	Specific heat at constant pressure
C_P	Power coefficient
C_T	Thrust coefficient
C_{TTR}	Tail rotor thrust coefficient
D	Aerodynamic drag
e	Hinge offset
f	Fuel-air ratio
fm	Mass fraction
f_{ST}	Stoichiometric fuel-air ratio
F_x	Blade contribution to main rotor longitudinal force in helicopter axes
F_{xb}	Force along x direction in blade axes
F_{xs}	Force along x direction in shaft axes
F_y	Blade contribution to main rotor lateral force in helicopter axes
F_{yb}	Force along radial direction in blade axes
F_{ys}	Force along radial direction in shaft axes
F_z	Blade contribution to main rotor vertical force in helicopter axes
F_{zb}	Force along z direction in blade axes
F_{zs}	Force along z direction in shaft axes
h	Specific enthalpy
H_{MR}	Horizontal force acting on main rotor (quasi-steady)
h_{TR}	Distance along z axis between main rotor and tail rotor
H_u	Upper heat of combustion

I_β	Blade moment of inertia
k	Ratio of specific heats
K_{trans}	Transmission ratio
K_x	Linear inflow coefficient
L	Aerodynamic lift
l_{TR}	Distance along x axis between main rotor and tail rotor
M	Molecular mass
Ma	Mach Number
$\dot{m}$	Mass flow
$\dot{m}_{corr}$	Corrected mass flow
$\dot{m}_f$	Engine fuel consumption
M_x	Blade contribution to main rotor rolling moment in helicopter axes
M_{xMR}	Main rotor rolling moment
M_y	Blade contribution to main rotor pitching moment in helicopter axes
M_{yfus}	Fuselage pitching moment
M_{yMR}	Main rotor pitching moment (quasi-steady)
M_z	Blade contribution to main rotor torque in helicopter axes
M_{zMR}	Main rotor torque
M_β	Flapping moment
n	Number of moles
N	Rotational speed in RPM
N_b	Number of blades
N_{corr}	Relative corrected speed
N_{FPT}	Free power turbine RPM
$\widehat{N}_{FPT}$	Free power turbine optimal RPM
p	Pressure
P_A	Accessory power
P_{load}	Engine power load
P_{MR}	Main rotor power
P_{TR}	Tail rotor power
Q	Heat per unit mass
r	Generic radial position from hinge
r	Pressure ratio, or pressure loss

R	Main rotor radius
R	Gas constant
Re	Reynolds number
s	Specific entropy
SFC	Specific fuel consumption
T	Temperature
T	Thrust
t	time
T_{MR}	Main rotor thrust (quasi-steady)
TR	Transmission ratio
T_{TR}	Tail rotor thrust
V	Forward speed (true airspeed)
V_{AS}	Airfoil section speed in wind axes
V_i	Induced velocity
V_P	Airfoil perpendicular speed in wind axes
V_R	Airfoil radial speed in wind axes
V_T	Airfoil tangential speed in wind axes
W	Helicopter weight
x_{CG}	Distance along x axes between main rotor and center of gravity
y_{CG}	Distance along y axis between main rotor and center of gravity
Y_{MR}	Lateral force acting on main rotor (quasi-steady)
z_{CG}	Distance along z axis between main rotor and center of gravity

Greek Symbols

α	Angle of attack
α_{MR}	Main rotor angle of attack
β	Beta function
β	Blade flapping angle
β_0	Coning angle
β_{1c}	Longitudinal flapping angle
β_{1s}	Lateral flapping angle
δ	Tail rotor cant angle
η_{eng}	Engine thermal efficiency

η_{is}	Isentropic efficiency
η_m	Mechanical efficiency
η_{trans}	Transmission efficiency
Θ	Helicopter pitch attitude
ϑ	Blade pitch angle
ϑ_0	Collective pitch angle
ϑ_{1c}	Lateral pitch angle
ϑ_{1s}	Longitudinal pitch angle
θ_{FP}	Flight path angle
θ_s	Shaft pitch angle
λ	Induced velocity parameter
Λ	Blade yaw angle with respect to wind
λ_i	Induced velocity parameter for linear inflow model
λ_{i0}	Inflow coefficient for uniform inflow
λ_{TR}	Tail rotor induced velocity parameter
μ	Rotor advance ratio
$\nu\beta$	Dimensionless flap frequency
ξ	Dimensionless hinge offset
ρ	Air density
υ	Kinematic viscosity
φ	Local inflow angle
Φ	Helicopter roll attitude
χ	Wake skewness
ψ	Blade azimuthal angle
Ω	Angular speed
Ω	Overall system optimal angular speed (minimum fuel flow)
Ω_{FPT}	Free power turbine angular speed
$\widehat{\Omega}_{FPT}$	Free power turbine optimal angular speed (maximum FPT efficiency)
Ω_{MR}	Main rotor angular speed
$\widehat{\Omega}_{MR}$	Main rotor optimal angular speed (minimum power)

Superscripts

0	Total conditions

Subscripts

amb	Ambient
bd	Bleed duct
comb	Combustor
comp	Compressor
d	Dynamic inlet
fus	Fuselage
is	Isentropic
MR	Main rotor
n	Nozzle
ref	Reference
stat	Static
tot	Total
TR	Tail rotor

Acronyms

BEMT	Blade Element Momentum Theory
CNRL	Constant Speed Running Line
CFD	Computational Fluid Dynamics
CVT	Continuously Variable Transmission
FPT	Free Power Turbine
FRT	Fixed Ratio Transmission
GGT	Gas Generator Turbine
ONRL	Optimal Speed Running Line
RPM	Revolutions per minute
UAV	Unmanned Air Vehicle
VSR	Variable Speed Rotor
VTOL	Vertical Take-Off and Landing

Chapter 1

Introduction

1.1 Motivation of the Present Research

Current trends in civil aviation are imposing to the aerospace industry greater demands on reducing environmental impact. In Europe, a number of environmental goals have been set by the Advisory Council for Aeronautics Research (ACARE), which include reductions in carbon dioxide (CO_2) and nitrogen oxides (NO_x) emissions of the order of 50% and 80%, respectively [1]. For this reason, the need to address these targets pushes the rotary-wing community towards implementing specific actions to reduce engine fuel consumption.

In order to achieve these goals, several European Projects were proposed in the last turn of European funded research (2007-2013), namely the *Seventh Framework Programme (FP7)*. Regarding specific aeronautical subjects, the Clean Sky (see www.cleansky.eu for more elucidations), a European Joint Technology Initiative (JTI), represents one of the largest European research projects ever launched. Its mission was to develop breakthrough technologies in order to reduce the environmental impact of airplanes and air transport. The JTI consisted of 6 integrated technology demonstrators (ITD) that provided the development of in-flight and ground demonstrators. Among these projects the Green Rotorcraft (GRC) stood out for its contribute in improving VTOL (Vertical Take Off and Landing) aircrafts.

The University of Padova participated in several GRC project sub-tasks, mainly focused on the reduction of rotorcraft components drag, so as to increase airframe and non-rotating systems efficiency. The new EU research funding programme, *Horizon 2020*, is about to begin, and therefore new ideas and concepts which can be implemented in order to achieve the abovementioned goals will have to be proposed.

In the present doctoral thesis, a possible way to reduce rotorcraft fuel consumption is described. To this aim, a promising research field is represented by employing a Variable Speed Rotor (VSR) in rotorcrafts. As will be clear in the next sections, for a series of reasons normal helicopter operation requires a nearly

constant main rotor rotational speed for the entire steady state flight envelope of the aircraft. The same holds also for the engine power turbine which is mechanically linked to the main rotor by means of a reduction gearbox.

Variable speed safe operation is difficult to be achieved in practice, mainly because of vibrational problems; however, it is of major interest to understand the possible performance gains related to the introduction of this technology. We want to understand if variable speed could represent a valuable solution to the fuel consumption issue. If it does, research towards the solution of the arising vibrational problems could be justified; it is also of great importance to identify the zones inside the operating envelope in which it is worth to apply the variable speed technology. A partial application of the variable speed concept, seen as the best compromise between performance improvement and vibration issues, could probably represent the optimal solution to the problem.

State of the art research upon rotorcraft dynamics usually employs the use of linearized models of the turboshaft engine, which are not sufficiently accurate to understand the effects of power turbine speed variation. One of the goals of the research proposed here is therefore to build or collect all the simulation tools needed to reliably predict the performance of a rotorcraft employing a variable speed main rotor and power turbine.

1.2 Review on Variable Speed Rotors: Potential Issues and Advantages

As stated in section 1.1, a promising research field, aimed at fuel consumption reduction, is represented by introducing a variable speed power turbine-main rotor inside VTOL aircrafts, among which the most interesting, for commercial and military use, are helicopters and tilt-rotors.

A typical helicopter configuration is visible in Figure 1.1; let us focus directly on the engine and main rotor components, which are linked together via the transmission gearbox. One or more engines can be employed to provide the sufficient power required by the helicopter. Note that engine output speed and main rotor speed are in a fixed ratio; another fixed, but different ratio exists between main rotor and tail rotor. The engine power is delivered to the transmission gearbox, which redistributes it to the main rotor, tail rotor, and other accessories at different speeds and torques.

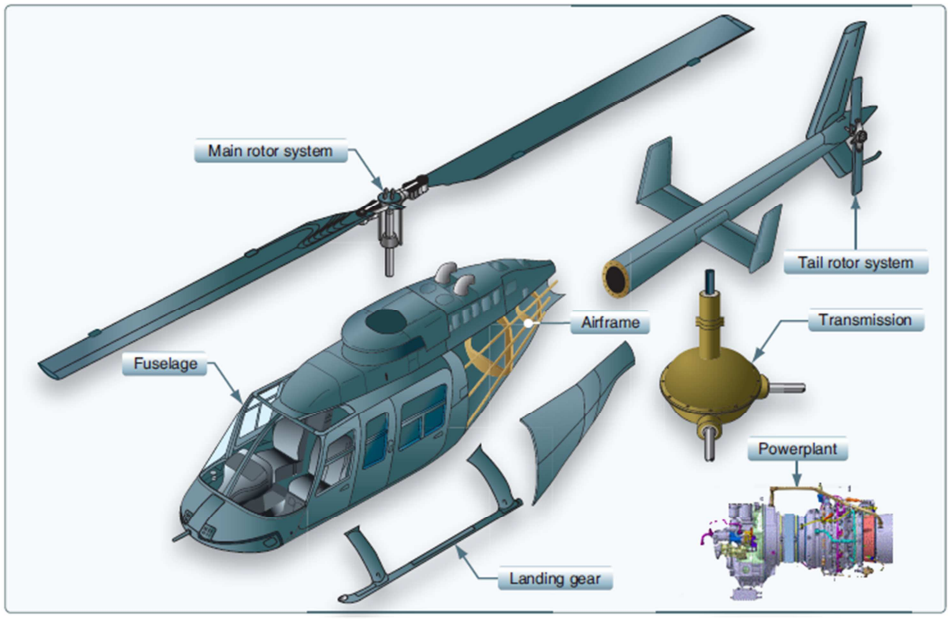

Figure 1.1 Typical helicopter configuration and components (adapted from [2]).

For this reason, the speeds of the different components are all strictly dependent on the engine output rotational speed. Modern helicopters are usually powered by turboshaft engines; we restrict our analysis to this type of engine, not considering small helicopters which operate with an internal combustion engine (ICE). An overview of a typical turboshaft engine assembly can be found in next chapter (section 2.1); usually, even if there are numerous exceptions[§], the engine mounted is a two spool configuration type, employing a constant speed free power turbine (FPT). This means that the engine output speed coincides with the FPT speed, whereas on another shaft, namely the gas generator shaft, a compressor and a turbine operate to produce high enthalpy (and pressure) gas, that can be used by the FPT to produce power. The gas generator shaft is free to vary its speed as a function of the external load; the FPT shaft, instead, is directly linked to the main rotor via a reduction gearbox, and its speed is kept almost constant in each flight condition by an electronic control. In fact, the Full Authority Digital Engine Control (FADEC) adjusts the amount of fuel injected, ensuring that the FPT speed (and the main rotor speed consequently) is maintained as constant as possible for each type of flight maneuver. Typical permitted variations in engine output speed do not exceed 15% [3]; main rotor speed acceptable variability is usually even

[§] Small ultra-light helicopters can employ a single spool turboshaft engine; this means that not only one turbine is constrained to operate at a multiple speed of the main rotor, but also the compressor.

lower. But why helicopters are built with such a constraint? The are two main reasons for choosing a constant rotational speed across the whole flight envelope:

1. **Decrease in engine efficiency at part load**. Turboshaft engines operate at high efficiencies only in a narrow power turbine RPM range. The component most affected by variable speed is the FPT, whose speed (and thus also efficiency) is strictly dependent on helicopter main rotor speed. There are two different ways of dealing with this problem. The first possibility consists in improving the design of the FPT stages in order to increase the high efficiency range of the turbine; this approach is thoroughly discussed in section 1.3. The second solution can be found in breaking the interdependence between FPT rotational speed and main rotor RPM, typical of a fixed ratio transmission. This can be achieved by employing a variable speed transmission, in either the form of a multiple speed gearbox or a more innovative, continuously variable transmission concept (see section 1.4 for more details).
2. **Resonant frequencies.** Resonant vibrations may occur not only due to shaft critical speeds, but also in the airframe [4], where a particular rotor speed inside the operating envelope could excite the rotorcraft structure. The vibrational load analysis is strongly dependent on the particular helicopter design and requires a model complexity which is beyond the scope of the present paper. There are some possible ways to solve the vibrational problem by means of different damping techniques. One possible solution could be represented by Active Vibration Control, a technology already present on the UH-60 which could be improved to withstand VSR operation. Another solution is given by bringing up composites into the airframe, which can reduce the dynamic stresses and vibratory loads transmitted to the hub [5]; see [6] for a review on high damping composites. Recent practical examples of VSRs built with composites are Boeing's A160 Hummingbird (see [7]) and Bell Helicopter's Eagle Eye UAV, both employing a VSR. However, their rotational speed is not free to vary in a continuous manner, it is constrained to two or more discrete rotational speeds.

The focus of the present thesis is on performance estimation; the models employed do not permit us to understand the variation in dynamic and vibratory loads given by VSR operation. These issues are beyond the scope of this study, even if they are extremely important since they determine the feasibility of the VSR concept, and will be addressed in future works. It is expected that

performance gains achieved by optimum rotor speed operation will have to be constrained by limitations due to vibrational issues. However, from a performance standpoint, it is interesting to analyze different types of variable speed rotor arrangements in order to understand the usefulness of such implementations.

A valuable work in this direction was made by Steiner [8], who ran various simulations using a trim model of the UH-60 Black Hawk helicopter. He examined the possibility of main rotor power reductions through variation of engine RPM. From his results, the biggest reduction in helicopter power demand provided around 17% improvement for the airspeed range of 25-60 m/s (50-120 kts) and 12% in hover. The simulations were performed at sea level conditions for a helicopter gross weight of 8,300 kg (18,300 lbs). In a more recent work by Mistry and Gandhi [9], the possibility of coupling main rotor RPM and radius variations, with the aim to reduce rotor power, was analyzed for the UH-60. They considered +17% to –16% variation in radius and ±11% variation in RPM about the baseline, over a range of different airspeeds, gross weights, and altitudes. More than 20% reduction in main rotor power under “high-and-heavy” conditions was feasible, as a result of the combined RPM reduction and radius increase.

These studies have been focused on main rotor and helicopter attitude simulation, without modeling the turboshaft engine. However, from an overall performance standpoint, the most interesting parameter to be studied is certainly fuel consumption, which is one of the most relevant driving parameters in a new design choice. Therefore, the required power reduction has to be translated in fuel flow variation using a turboshaft model.

This aspect was first addressed by Garavello and Benini [10], who studied the impact of choosing an optimal main rotor speed for the UH-60 on overall engine performance. They implemented a simple performance model of the helicopter, able to calculate the required power using basic momentum theory and blade element theory equations. Using this model they calculated the values of main rotor speed minimizing helicopter power for various advancing speeds; in addition, they used these power levels as an input inside a model of the GE T700 turboshaft engine and they calculated fuel flow variation, assuming a traditional mechanical gearbox. From their results, it becomes apparent that minimizing total helicopter power is not equivalent to minimizing fuel consumption. Instead, in more than one case, the constant speed simulation was characterized by lower fuel consumption than the optimized one. The main reason for this phenomenon is found in the fact that the turboshaft engine FPT has its own optimal speed, which is generally different from the main rotor one.

FPT optimal speed ($\hat{\Omega}_{FPT}$) is not a fixed value, but mainly depends on shaft torque and also on ambient conditions, which affect overall engine performance. It is defined as the speed which maximizes engine efficiency at a particular power level.

*Main rotor optimal speed ($\hat{\Omega}_{MR}$), instead, depends on the advancing speed, weight, flight path angle and also the ambient conditions***.** It is defined as the speed which minimizes total helicopter power (whose most important fraction is main rotor power) in a particular flight condition.

In a fixed-ratio transmission helicopter, when using a variable RPM rotor, particular attention must be paid to the interaction between the main rotor and the turboshaft engine: as the main rotor RPM are strictly dependent on the engine FPT rotational speed, a trade-off among the requirements of the two systems has to be determined. Thereby, a correct determination of the optimum speed value which minimizes fuel consumption requires the integration of the helicopter and turboshaft engine models inside the same optimization routine. *This global optimal speed does not coincide, in principle, with neither $\hat{\Omega}_{MR}$ or $\hat{\Omega}_{FPT}$, but is instead determined as the best trade-off between the two.*

This task was performed by Misté and Benini [11], once more on the UH-60 helicopter. First, using the same main rotor model of Ref. [10], they studied how optimal main rotor speed affected turboshaft engine performance, finding that the most significant component was the FPT, as expected. Subsequently, they studied FPT optimal speed alone to understand its pattern. Finally, they built up an optimization algorithm, able to search for the minimum fuel consumption, merging together both the engine and helicopter model. The results given by their analysis stated that for intermediate advancing speeds minimizing main rotor power was almost equivalent to minimizing fuel consumption. However, at high and low forward speed velocities, this is no longer true, since the FPT efficiency reduction due to main rotor speed variation is higher than the benefits given by overall power reduction; the highest fuel reduction detected was about 16%. These promising preliminary results justify a deeper analysis to assess the validity of the simplifying assumptions used. In fact, in both [10] and [11], the main rotor model is very simple and does not take into account the attitude of the helicopter, nor important blade compressibility and stall effects. The optimizations carried out were constrained to a generic “safe boundary”, in which stall and high Mach numbers were avoided. In the present thesis the models presented in [11] will be described and these new important helicopter features will be introduced inside the optimization loop.

Till now our considerations have been based on the assumption that FPT speed and main rotor speed are strictly dependent, as is required when using a traditional fixed-ratio transmission. In fact, all the research papers regarding this subject found in the literature deal only with this type of VSR. But what happens if we are able to introduce a variable speed transmission? Well, as stated earlier, we are able to break the interdependence between FPT and main rotor speed. This means that we could theoretically achieve optimal speed operation for both FPT and main rotor, without the necessity to find a compromise speed. This obviously is not inexpensive; the main drawbacks of such approach are given by a likely increase in weight and efficiency loss of the of the mechanical transmission, as well as potential problems connected with its reliability and production (and even certification) costs.

Before going further, we should emphasize in sections 1.3 and 1.4 the conceptual distinctions between these two possible research approaches when dealing with VSRs, underlining pros and cons.

In the preliminary design of a new helicopter, the main decisional factor in choosing one of these two approaches might simply be given by research costs. However, for helicopters currently in use, the variable speed FPT approach can represent a reasonable way of reducing fuel consumption without introducing new or additional mechanical parts. The worthiness of this reduction will be clearly different for every single different helicopter case and can be achieved, in practice, by modification of the control system software.

1.3 Fixed Ratio Transmission, Variable Speed FPT

Fixed ratio transmissions represent the state-of-the-art technology for helicopter drivetrains. The most common fixed ratio gear type for a helicopter main rotor is a planetary stage (the main module in Figure 1.2) which features an output shaft driven by several planets [12]. An advantage of the planetary stage compared to a simple parallel shaft arrangement is that each planet gear must transmit only a part of the total torque. This load sharing results in a smaller, lighter transmission. A valid alternative to planetary stages is given by split torque stages (Figure 1.3). Split torque design transmissions offer several advantages over conventional planetary gears arrangements, such as lower weight, lower energy losses, higher reduction ratio and reliability [12],[13].

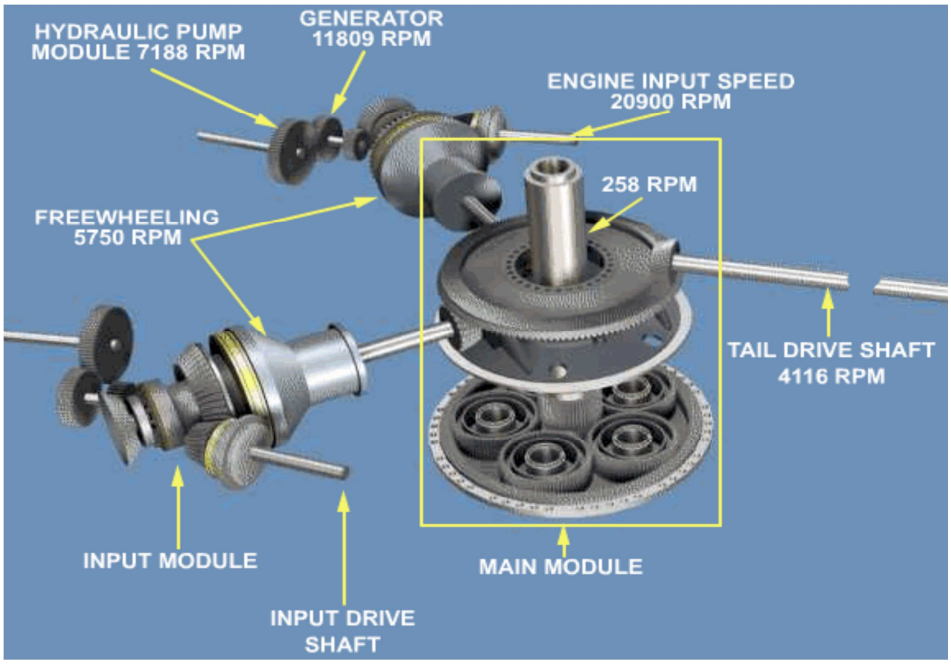

Figure 1.2. UH-60 transmission employing a planetary stage (main module).

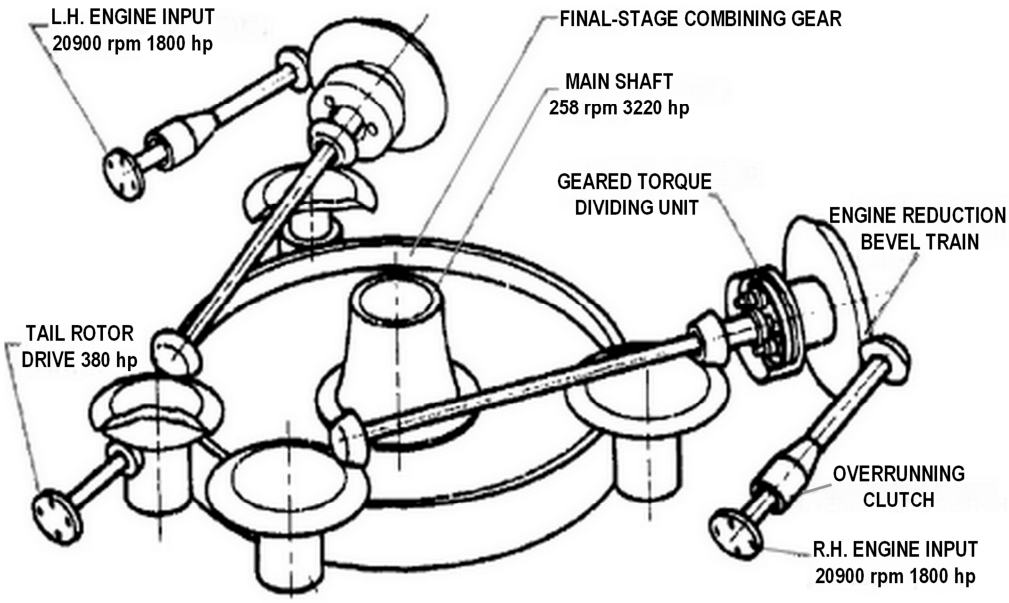

Figure 1.3. Split torque transmission design compatible with the UH-60 (adapted from [12]).

FRT efficiencies usually range from 97% to 99% in helicopter applications [14]; this is an important value to be considered for comparison with variable speed transmissions.

Due to the fixed ratio transmission the rotational speed of the main rotor is strictly dependent on engine RPM, as can be seen by transmission ratio definition:

$$TR = \frac{\Omega_{FPT}}{\Omega_{MR}} = const \tag{1.1}$$

As a consequence, optimal speed operation implies a trade-off among the requirements of the main rotor and engine subsystems. The research effort is mainly dedicated to solving the problem of turboshaft engine efficiency losses in conditions far from the engine design point, which can be solved by improving the FPT stages design in order to widen the high efficiency interval of the turbine. The work carried out by D'Angelo [15] is the first analysis found in literature upon a wide speed range turboshaft. Recent studies at the NASA Glenn Research Center are also pointed towards this objective: with the aim of assessing the feasibility of a variable speed tilt-rotor concept, Welch et al. [16] studied the redesign of the FPT in order to obtain a good performance on the entire RPM interval, from 100% (take off) to 54% (cruise). The new turbine design is characterized by high work factors in the cruise condition and wide incidence angle variations in vanes and blades among the entire operating speed envelope. The rotordynamic feasibility of this FPT design is treated in a different paper by Howard [17], in which he analyzes the problems concerned with placing shaft critical speeds in the operating speed envelope. The results derived from these different research works state that operating the turboshaft engine at variable speed without losing too much efficiency is viable.

1.4 Variable Speed Transmission

A wide variety of variable speed transmissions are technically available for standard applications; unfortunately, very few seem to be suitable for the case of high, helicopter specific power loads. Stevens et al. [18] exclude the possibility to use any traction/friction drive and fluid-traction transmissions, widely used in the automotive industry, for rotary wing applications, mostly because of low reliability, excess weight and heat generation problems.

Litt et al. [3], instead of using CVT, propose a solution to the problem by means of multiple speed gearboxes. A sequential shifting control algorithm for a twin-engine rotorcraft that coordinates both the disengagement and engagement of the two turboshaft engines is developed with the objective to vary main rotor speed smoothly over a wide range, still maintaining the engines within their prescribed speed bands.

However, from a functional point of view, the idea of CVT is highly desirable contrasted to the operability of a discrete multispeed drive [18] for various reasons,

one of them being the possibility for CVTs to reach optimal speed continuously depending on the flight condition.

Lemanski [19] patented an innovative variable speed transmission, the pericyclic CVT (P-CVT), which is a non-traction nutating drive mechanism incorporating positive engagements of rollers and cams. The main advantages given by this type of CVT are much higher torque density and power transmission efficiency than any other known continuously variable mechanical power transmission systems. The pericyclic mechanism (Figure 1.4) can operate both as a fixed transmission or a CVT, whether the speed of the reaction control component is held to zero or is varied by means of a speed control unit. The following is the main drawback of the P-CVT: two different power inputs are needed in order to achieve speed variability. If the speed input to the reaction control member has to be varied continuously, the most plausible power input has to be electromechanical. In a paper on CVT for hybrid vehicle applications, Elmoznino and Lemanski [20] suggested a power flow configuration in which part of the mechanical energy produced by an internal combustion engine is converted in electrical power and then reconverted in mechanical energy, providing the necessary torque and speed for the reaction control member (Figure 1.5). The worthiness of this double conversion depends on the energy conversion efficiency and the power flow magnitude into the two different members, i.e. the input shaft and the reaction wheel. In fact, if only a small part of the power is flowing in the reaction wheel member, even poor energy conversion efficiency could be acceptable. The application of pericyclic CVT to helicopter main rotors is discussed by Saribay [21],[22] and Hameer [23]. In their studies, they discovered that in various configurations in which the output speed was varied between 50% to 100% of the design point value, the power flow in the reaction member could be as high as 50% of the total power coming from the turboshaft engine, which implies very large energy conversion devices. Thus, using electric generators as variable control units is not a viable solution for helicopters, for mainly three reasons: weight, energy conversion efficiency and reliability. Research has still to be done in order to understand if there are possible alternative power paths which can reduce loading on the reaction wheel. However, the pericyclic transmission is a very promising mechanism, since it was demonstrated that more than 40% drivetrain weight reduction was possible when compared to previous gear designs (planetary and split torque) [23].

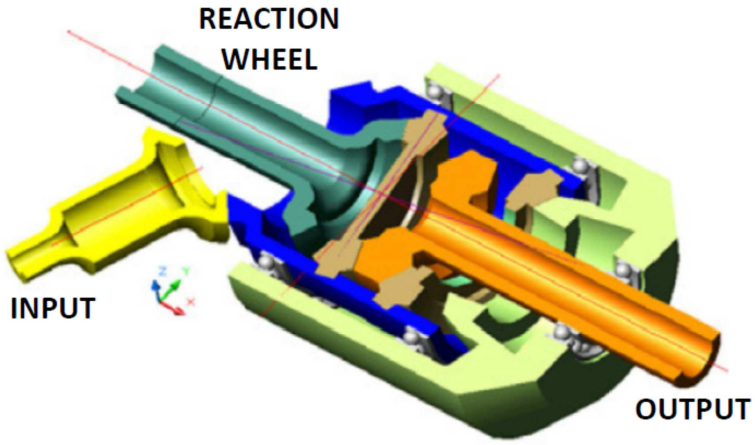

Figure 1.4. Example of pericyclic transmission [23].

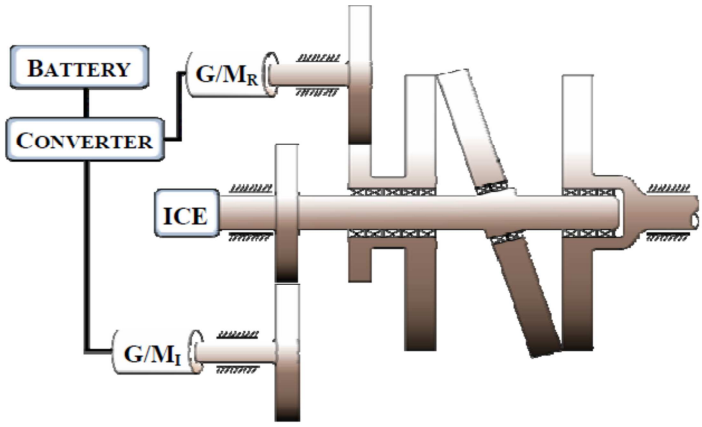

Figure 1.5. Hybrid vehicle P-CVT: a part of the mechanical energy produced by the internal combustion engine (ICE) has to be converted in electricity by the generator G/M_I and reconverted by G/M_R at the desired speed.

A possible innovation in helicopter drivetrain technology could be represented, instead, by magnetic gears. A magnetic gear uses permanent magnets to transmit torque between an input and output shaft without mechanical contact (Figure 1.6). Instead of using mechanical teeth, it uses permanent magnets, which have a similar function; this analogy is even more supported by the fact that the ratio between the number of outer and inner magnets determines the speed ratio. One may argue that in order to transmit high torques, very big and heavy gears would be needed. This is not true, since in a magnetic gear (of the type seen in Figure 1.6) all the magnets are engaged, whereas in a mechanical gear only few teeth can be engaged. As a consequence, weight-to-torque ratios of certain types of magnetic gears have weight-to-torque ratios comparable to their mechanical counterpart [24].

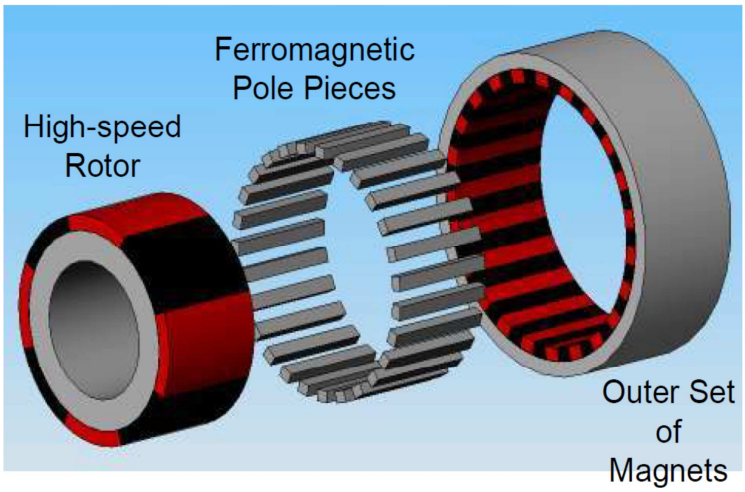

Figure 1.6. Exploded view of a magnetic gear

Atallah [25] invented and demonstrated the first high-torque magnetic gear in 2001; it was still a fixed ratio transmission, though. Compared to mechanical gears, such technology is claimed to offer advantages including reduced maintenance, improved reliability, no need for lubricants, higher efficiency (>99%), high torque density, reduced drivetrain pulsations, low noise, and inherent overload protection. However, this last feature is not only positive: even if the magnetic transmission prevents damage and failure in case of high torque loads by letting the magnetic gears to slip between each other, this same slip motion can be responsible for instantaneous loss of torque in particularly rapid transient maneuvers.

Briefly speaking, an efficient magnetic CVT concept for rotorcraft applications has still to be invented and proven reliable. However, the specific features of the magnetic gear, and mainly the possibility to modify the speed ratio by varying the magnetic field between inner and outer gears, make it one of the most promising devices for efficient variable speed operation. The rotorcraft industry is quite reluctant to the introduction of revolutionary components in a sector in which safety and design experience are the dominating factors; in addition, from a strict economic perspective, new transmission configurations have to undergo costly certification processes, which may not justify the research effort.

Nevertheless, fixed ratio magnetic gears seem to have already found important technical applications and appear to be a promising alternative to mechanical gears: Davey et al. [26] state that preliminary assessments of magnetic gears with TR=50:1 are characterized by weight-to-torque ratios of 0.018 lbs/ftlbs

(based on an 8 MW capability) which are torque densities even higher with respect to normal helicopter gearing. Moreover Magnomatics®, a company cofounded by Atallah, claims that an efficient magnetic variable speed technology has been already developed, along with wind turbine applications [27]. The variable speed capability of such a transmission is in its early stages of development. At the moment the speed change is obtained by varying the magnetic field using electrical current flowing in external coils. A certain amount of auxiliary power is therefore required to achieve rotational speeds different from the design value, and the ratio between auxiliary power and transmitted power has still to be investigated. As for the P-CVT, the worthiness of such solutions depends on the values of additional electrical power that has to be absorbed by the CVT to work properly; a trade-off study has to be made between performance gains grace to a CVT and power loss due to correct CVT operation.

In conclusion, all the possible variable speed transmission types presented here are still in the concept design phase and it is still not well defined which of the ones presented would be the most suitable for helicopter operation. Magnetic gears seem to be promising, but still no research has been done inside the rotorcraft industry to the knowledge of the author.

The research effort in this particular field may lead to interesting results and is justified by the fact that employing a variable speed transmission makes it possible for both main rotor and turboshaft engine to operate at their optimal speeds.

1.5 Performance Estimation of a VSR

In order to understand in which of the two abovementioned approaches it is worth to put our research efforts, it is necessary to quantitatively compare the respective performance of both of them. For this to be done, we need at least two reliable simulation tools:

- a gas turbine simulation code, able to perform steady state turboshaft engine design and off-design simulations;
- a helicopter trim flight simulator, able to determine the total power consumed in each quasi-steady level flight condition.

The methodology adopted for the present research study consisted in engine computer simulations by using a helicopter simulation software, TCOPTER, and an in-house implemented gas turbine performance simulator, TSHAFT. The two codes, implemented in MatLab® language, have been validated with experimental

performance data found in literature and through comparisons with a commercially available software. TSHAFT was also employed to assess the installation performance of the ERICA tilt-rotor (*Enhanced Rotorcraft Innovative Concept Achievement*), a subtask related to the *Clean Sky GRC-2* research project.

The necessity of having clear indications about the trade-offs and the possible improvements obtained through application of the variable speed rotor concept underlines the need of more accurate simulations for correct engine and rotorcraft performance prediction. The current trend is pointing towards integration of models referred to different rotorcraft segments (engine model, main rotor model, emissions model, etc.), in order to build a more sound and reliable model of the complete rotorcraft.

1.6 Thesis Objectives

The objectives of the present thesis can be summarized as follows:

1. Implementation of a methodology able to estimate helicopter performance variation when variable speed technology is employed. The tools needed for such an approach are to be validated against experimental data and other reliable simulation data that can be found in the open literature.
2. Quantification of possible performance improvements given by VSR operation by testing the methodology upon a real helicopter case.
3. Determination of the pros and cons in employing a variable speed transmission; quantification of possible improvements with respect to the standard fixed ratio transmission.
4. Investigation regarding possible improvements to the VSR concept and concrete proposals.
5. Implementation of a FPT redesign routine in order to reduce FPT efficiency degradation when operating at far from design rotational speeds.

1.7 Thesis Outline

The thesis is organized as follows: first, the two simulation codes needed to carry out our study are presented. **Chapter 2** represents a thorough description of the TSHAFT code, along with the model equations used to calculate engine design and off-design performance. TSHAFT extensive code validation is presented in **Chapter 3**, with a series of comparisons with other commercial validated software and OEM's engine deck. **Chapter 4** contains the model

equations employed by TCOPTER along with its numerical trim calculation procedure.

Following the presentation of the models, an overview is given with reference to the optimization process implemented to find the optimal rotor speed corresponding to minimum fuel consumption. Since we want to quantify the possible performance gains of the VSR concept, a real case study is analyzed in **Chapter 5**: the helicopter simulated is the UH-60 Black Hawk. Both helicopter trim and engine models are built and their validation to experimental data is shown. An analysis with a traditional fixed-ratio transmission is carried out. Optimal main rotor-FPT speed is calculated for level flight conditions from 0 to 90 m/s (0-175 kts). Three different altitudes are considered, and three different helicopter weights are simulated, in order to let the reader understand in which particular flight conditions the variable speed concept achieves the best reductions in fuel consumption. **Chapter 5** represents the application of the VSR concept on a real helicopter case, without changing any components, but simply calculating the optimum performance points in different flight conditions. **Chapter 6**, instead, deals with the theoretical introduction of a CVT gearbox in the UH-60; since main rotor-FPT speed interdependence is broken, the maximum fuel consumption reduction can be obtained by employing both main rotor optimal speed $\hat{\Omega}_{MR}$ and FPT optimal speed $\hat{\Omega}_{FPT}$. The flight conditions analyzed are the same encountered in **Chapter 5**, in order to make a performance comparison between the two VSR concepts.

Chapter 7 introduces new ways to improve the VSR concept. In fact, till **Chapter 6**, only calculations related to existing designs of helicopter and engine are made. What if we try to redesign helicopter components explicitly for variable speed operation? The first choice falls on the FPT component, since it is the one mostly affected when traditional fixed-ratio transmissions are used. Therefore, an analysis will be presented related to the FPT redesign techniques available to flatten the efficiency curve with respect to RPM variation.

Finally, in **Chapter 8** the most important conclusions resulting from this study and the recommendations for future work activities are outlined.

1.8 References

[1] I. Goulos, V. Pachidis, R. D'Ippolito, J. Stevens, and C. Smith, *An Integrated Approach for the Multidisciplinary Design of Optimum*

Rotorcraft Operations, Journal of Engineering for Gas Turbines and Power, September 2012, Vol. 134.

[2] VV. AA., *Helicopter Flying Handbook*, U.S. Department of Transportation, Federal Aviation Administration (FAA), 2012. Available online at www.faa.gov/regulations_policies/handbooks_manuals/aviation/helicopter_flying_handbook/media/helicopter_flying_handbook.pdf (last consultation Jan. 2015).

[3] J. S. Litt, J. M. Edwards, and J. A. DeCastro, *A Sequential Shifting Algorithm for Variable Rotor Speed Control*, NASA TM 214842, 2007.

[4] W. Johnson, *Helicopter Theory*, Dover Publications Inc., New York, 1980.

[5] R. Ganguli, I. Chopra, *Aeroelastic optimization of a helicopter rotor to reduce vibration and dynamic stresses*, Journal of Aircraft, Vol. 33, No. 4 (1996), pp. 808-815.

[6] H. Lu, X. Wang, T. Zhang, Z. Cheng and Q. Fang, *Design, Fabrication, and Properties of High Damping Metal Matrix Composites—A Review*, Materials, 2009, 2, 958-977.

[7] A. E. Karem, *Optimum Speed Rotor*, U.S. Patent No. 6,007,298, 1999.

[8] J. H. Steiner, *An Investigation of Performance Benefits and Trim Requirements of a Variable Speed Helicopter Rotor*, MSc Thesis, The Pennsylvania State University, 2008 (also available online at www.engr.psu.edu/rcoe/theses/Steiner_Jason.pdf, last consultation Jan. 2015).

[9] M. Mistry and F. Gandhi, *Helicopter Performance Improvement with Variable Rotor Radius and RPM*, Journal of the American Helicopter Society, Volume 59, Number 4, October 2014, pp. 17-35(19).

[10] A. Garavello and E. Benini, *Preliminary Study on a Wide Speed Range Helicopter Rotor/Turboshaft System*, Journal of Aircraft, 2012, Vol.49: 1032-1038, 2012.

[11] G. A. Misté and E. Benini, *Performance of a Turboshaft Engine for Helicopter Applications Operating at Variable Shaft Speed*, ASME Gas Turbine India Conference 2012 Proceedings, Mumbai.

[12] T. L. Krantz, M. Rashidi and J.G. Kish, *Split Torque Transmission Load Sharing*, NASA TM 105884, 1992.

[13] J. J. Coy and R.C. Bill, *Advanced Transmission Studies*, NASA/TM 100867, 1988.

[14] G. J. Weden and J. J. Coy, *Summary of Drive-Train Component Technology in Helicopters*, NASA/ TM 83726, 1984.

[15] M. D'Angelo, *Wide speed range turboshaft study*, NASA Contractor Report 198380, General Electric Company, 1995.

[16] G. E. Welch, A. B. McVetta, M. A. Stevens, S. A. Howard, P. W. Giel, A. A. Ameri, W. To, G. J. Skoch, and D. R. Thurman, *Variable-Speed Power-Turbine Research at Glenn Research Center*, American Helicopter Society 68th Annual Forum Proceedings, Fort Worth, May 1-3, 2012.

[17] S. A. Howard, *Rotordynamic Feasibility of a Conceptual Variable-Speed Power Turbine Propulsion System for Large Civil Tilt-Rotor Applications*, American Helicopter Society 68th Annual Forum Proceedings, Fort Worth, May 1-3, 2012.

[18] M. A. Stevens, R. F. Handschuh and D.G. Lewicki, *Variable/Multispeed Rotorcraft Drive System Concepts*, NASA TM—2009-215456, March 2009.

[19] A. J. Lemanski, *Variable Speed Power Transmission System*, 2006, U.S. Patent No. 7,147,583, B6.

[20] M. Elmoznino, K. Kazerounian and A. Lemanski, *An electro-mechanical Pericyclic CVT (P-CVT)*, 12th IFToMM World Congress, Besançon (France), June 18-21, 2007.

[21] Z. B. Saribay, *Analytical Investigation of the Pericyclic Variable-Speed Transmission System for Helicopter Main-Gearbox*, Ph.D. Thesis submitted to the Graduate School of Aerospace Engineering, Pennsylvania State University, 2009. Available online at www.engr.psu.edu/rcoe/theses/Saribay_Zihni.pdf

[22] Z. B. Saribay, E.C. Smith, A.J. Lemanski, R.C. Bill, K.W. Wang and S. Rao, *Compact Pericyclic Continuously Variable Speed Transmission Systems: Design Features and High-Reduction Variable Speed Case Studies*, Proceedings of the American Helicopter Society 63rd Annual Forum, Virginia Beach, Virginia, May 1-3, 2007.

[23] S. Hameer, *A Comparative Study and Application of Continuously Variable Transmission to a Single Main Rotor Heavy Lift Helicopter*, Ph.D. Thesis submitted to the School of Aerospace Engineering, Georgia Institute of Technology, 2009. Available online at http://smartech.gatech.edu/handle/1853/33969 (last consultation Jan. 2015).

[24] X. Li, K.T. Chau, M. Cheng and W. Hua, *Comparison of Magnetic-Geared Permanent-Magnet Machines*, Progress In Electromagnetics Research, Vol. 133, 177-198, 2013.

[25] K. Atallah and D. Howe, *A Novel High-Performance Magnetic Gear*, IEEE Transactions on magnetics, Vol. 37, No. 4, July 2001.

[26] K. Davey, M. Werst, and G. Wedeking, *Magnetic Gears – An Essential Enabler for the Next Generation's Electromechanical Drives*, Proceedings of the ASNE 2008. Available online at https://www.navalengineers.org/SiteCollectionDocuments/2008%20Proceedings%20Documents/EMTS%202008/Davey%20Paper.pdf

[27] www.magnomatics.com.

Chapter 2

TSHAFT: a Gas Turbine Simulation Code

2.1 Engine Thermodynamic Model

The first step to assess the performance modifications due to different type of VSR configurations on a particular helicopter is to implement a thermodynamic code able to predict the impact on fuel consumption of different rotor RPM values. To this purpose, TSHAFT, a lumped-parameters performance prediction software, was implemented and utilized. The code, written in MatLab® language, has been validated through comparisons with engine performance data given by commercially available software and experimental data found in literature; see Chapter 3 for an extensive presentation of the validation results. TSHAFT is able to perform steady state and transient simulations of different gas turbine types (turboshaft, turbojet, multi-spool, etc.); however, for the purpose of the present study, only steady state turboshaft configurations (an example of which can be found in Figure 2.1) will be considered.

In the following part of this section, a description of the theoretical bases and physical assumptions implemented in TSHAFT is given. Firstly, the turboshaft engine is modeled by linking one or more of the following components:

- inlet (or intake);
- compressor;
- bleed duct;
- combustor (or combustion chamber);
- gas generator turbine (GGT), mechanically connected to a compressor;
- free power turbine (FPT), which is connected to an external load, such as a main rotor or a propeller, by means of a power shaft;
- nozzle or exhaust duct;
- external load.

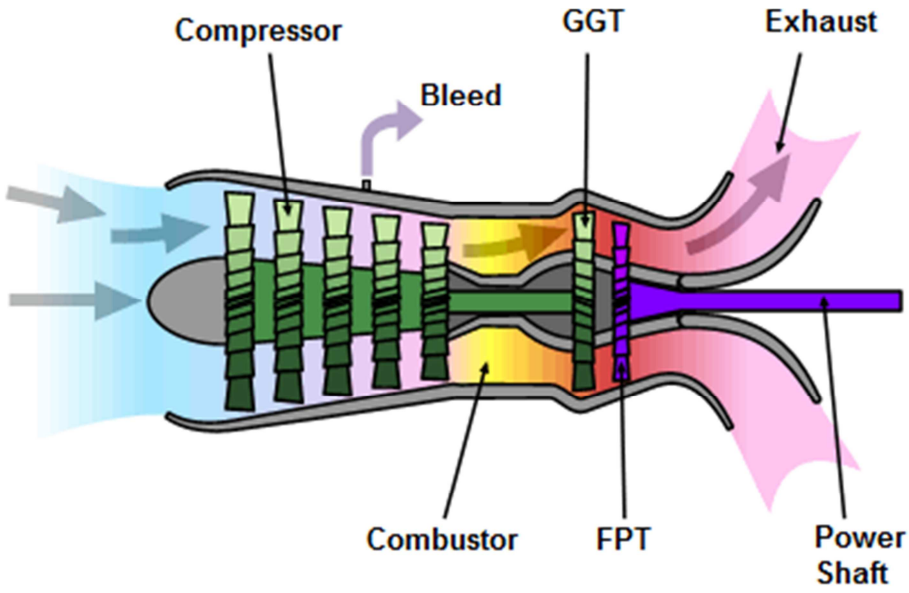

Figure 2.1. Example of typical turboshaft engine configuration.

In addition, the physical assumptions for the engine model are the following:

1. Steady state operation (i.e. no transient rotational speed variations are considered);
2. Lumped parameters model (or zero-dimensional approach): each component is represented by a block in which the thermodynamic state is determined only by input and output values of state variables which do not vary within the component;
3. Working fluid consisting of a mixture of ideal gases with variable specific heats;
4. Adiabatic components: each component has no heat exchange with the outside;
5. The irreversibilities are included in calculations through the use of different types of efficiency. For intakes, compressors and turbines total-to-total isentropic efficiencies are used, whereas for nozzles total-to-static isentropic efficiency is employed. Combustor efficiency is defined as the ratio between the actual heat released in the operating fluid and the ideal heat that would be generated if complete burning of the fuel injected in the combustion chamber could take place. The loss in real heat is considered only due to unburned fuel.

2.2 Fluid Composition

The operating fluid used in all the performed simulations is dry air, assumed as an ideal gas, for which the following constitutive relation will be used throughout all the models:

$$\frac{p}{\rho} = RT \tag{1.1}$$

where R is the specific gas constant which can be derived from the ratio between the universal gas constant and the molecular mass. The air mass fraction composition considered in the present analysis, especially useful when calculating the reacting species in the combustion chamber, can be read in Table 2.1.

Gas Species	Mass Fraction
O_2	0.2314
N_2	0.7553
H_2O	0.0000
CO_2	0.0005
Ar	0.0128

Table 2.1: Operating fluid composition [1].

The ambient conditions are determined by altitude and temperature selection; an ISA standard model is implemented to relate altitude to the values of static pressure and temperature (see Figure 2.2).

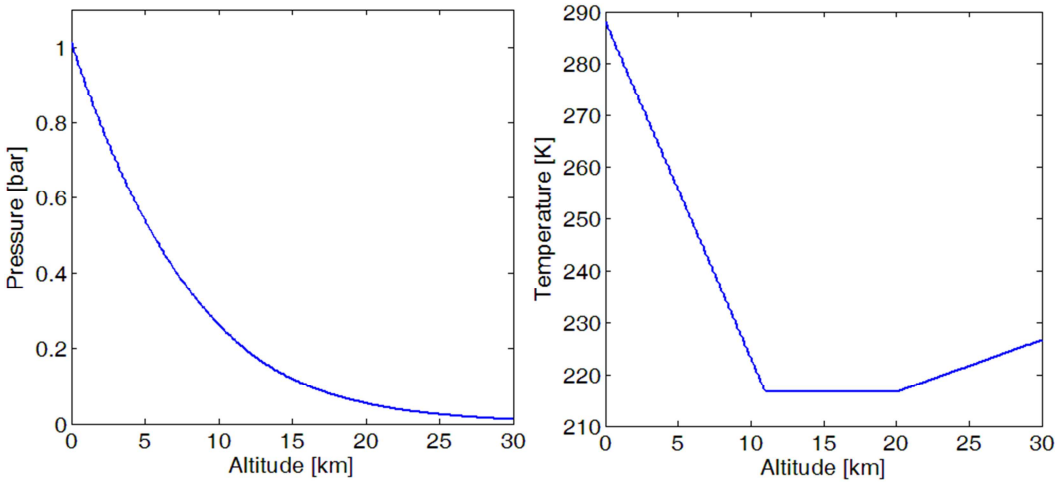

Figure 2.2. ISA temperature and pressure variation with altitude.

2.3 Specific Heat

To account for specific heat variation with temperature, the Shomate equation is used:

$$c_p = A + BT + CT^2 + DT^3 + ET^{-2} \tag{1.2}$$

where the coefficient values for each species composing the fluid are provided by NIST tables [2]. Since enthalpy and entropy are:

$$h(T) = h_{ref} + \int_{T_{ref}}^{T} c_p dT \tag{1.3}$$

$$s(T, p) = s_{ref} + \int_{T_{ref}}^{T} c_p \frac{dT}{T} - R \ln \frac{p}{p_{ref}} \tag{1.4}$$

where h_{ref} and s_{ref} are the standard reference conditions at T_{ref} = *288.15 K* and p_{ref} = *101325 Pa*. In each component of our model, the value of these state variables can be computed as follows:

$$h = AT + B\frac{T^2}{2} + C\frac{T^3}{3} + D\frac{T^4}{4} - \frac{E}{T} + F \tag{1.5}$$

$$s = A\ln(T) + BT + C\frac{T^2}{2} + D\frac{T^3}{3} - \frac{E}{2T^2} + G - R\ln\frac{p}{p_{ref}} \tag{1.6}$$

2.4 Ambient Conditions

Once flight altitude is determined, ambient pressure and temperature are derived from the ISA standard model interpolation. Together with flight Mach number definition, the conditions at the engine inlet are determined. In fact, inlet total values are calculated with the usual relations:

$$T_1^0 = T_{amb}\left(1 + \frac{k-1}{2} Ma_1^2\right) \tag{1.7}$$

$$p_1^0 = p_{amb}\left(1 + \frac{k-1}{2} Ma_1^2\right)^{\frac{k-1}{k}} \tag{1.8}$$

However, TSHAFT leaves the user free to insert arbitrary values for temperatures and pressures which are not dependent on the ISA atmosphere model, if needed.

As a result, all the variables necessary to establish the value of total enthalpy and entropy functions at the entrance of the air intake are known. Therefore, it is possible to start with the analysis of the engine cycle.

2.5 Thermodynamic Equations for Design Point Calculations

Before performing off-design performance calculations, a design point model of the engine must be defined which virtually fixes the geometry of the turboshaft engine. Output data from this model will be used as initial guess for the subsequent off-design simulations, and will also be employed to rescale component characteristic maps.

Here below the thermodynamic relationships used in the model are given for each component. They are a very important tool, since they also highlight the abovementioned model assumptions. The subscript 1 is related to the flow entering each specific component block, while the subscript 2 represents the exit conditions. The following equations given for each component, together with eq. (1.5) and (1.6), uniquely determine the output values of pressure, temperature, enthalpy, entropy and mass flow, from prior knowledge of the inlet conditions. For components in which external work exchange with the operating fluid takes place, performance parameters such as consumed or generated power are also calculated using isentropic efficiencies. Finally, in section 2.5.8 a formal definition of overall engine performance parameters is exposed.

2.5.1 Intake

$$p_2^{\,0} = r_d \, p_1^{\,0} \tag{1.9}$$

$$T_2^{\,0} = T_1^{\,0} \tag{1.10}$$

$$\dot{m}_2 = \dot{m}_1 \tag{1.11}$$

2.5.2 Compressor

$$p_2{}^0 = r_{comp}\, p_1{}^0 \tag{1.12}$$

$$s(T_{2is}^0, p_2{}^0) - s(T_1^0, p_1{}^0) = 0 \tag{1.13}$$

$$\Delta h_{is}^0 = h^0(T_{2is}^0) - h^0(T_1^0) \tag{1.14}$$

$$\Delta h^0 = \frac{\Delta h_{is}^0}{\eta_{comp}} \tag{1.15}$$

$$h^0(T_2{}^0) - h^0(T_1^0) - \Delta h^0 = 0 \tag{1.16}$$

$$\dot{m}_2 = \dot{m}_1 \tag{1.17}$$

$$P_{comp} = \dot{m}_1 \Delta h^0 \tag{1.18}$$

2.5.3 Bleed Duct

$$p_2{}^0 = r_{bd}\, p_1{}^0 \tag{1.19}$$

$$T_2{}^0 = T_1^0 \tag{1.20}$$

$$\dot{m}_2 = (1-b)\dot{m}_1 \tag{1.21}$$

2.5.4 Combustor

$$p_2{}^0 = r_{comb}\, p_1{}^0 \tag{1.22}$$

$$f = \frac{\dot{m}_f}{\dot{m}_1} \tag{1.23}$$

$$q = \dot{m}_1 f H_u \tag{1.24}$$

$$Q = f H_u = \Delta h^0 \tag{1.25}$$

$$\Delta h^0 = h^0(T_2{}^0) - h^0(T_1^0) \tag{1.26}$$

$$\dot{m}_2 = (1+ f)\dot{m}_1 \tag{1.27}$$

2.5.5 Gas Generator Turbine (GGT)

$$P_{ggt} = \frac{P_{comp}}{\eta_m} \tag{1.28}$$

$$\Delta h = \frac{-P_{GGT}}{\dot{m}_1} \tag{1.29}$$

$$\Delta h_{is} = \frac{\Delta h^0}{\eta_{GGT}} \tag{1.30}$$

$$h^0(T_2{}^0) - h^0(T_1{}^0) - \Delta h^0 = 0 \tag{1.31}$$

$$h^0(T_{2is}^0) - h^0(T_1{}^0) - \Delta h_{is}^0 = 0 \tag{1.32}$$

$$s(T_{2is}^0, p_2{}^0) - s(T_1{}^0, p_1{}^0) = 0 \tag{1.33}$$

$$\dot{m}_2 = \dot{m}_1 \tag{1.34}$$

2.5.6 Free Power Turbine (FPT)

$$P_{fpt} = \frac{P_{load}}{\eta_m} \tag{1.35}$$

$$\Delta h^0 = \frac{-P_{FPT}}{\dot{m}_1} \tag{1.36}$$

$$\Delta h_{is}^0 = \frac{\Delta h^0}{\eta_{FPT}} \tag{1.37}$$

$$h^0(T_2{}^0) - h(T_1{}^0) - \Delta h^0 = 0 \tag{1.38}$$

$$h(T_{2is}^0) - h(T_1{}^0) - \Delta h_{is}^0 = 0 \tag{1.39}$$

$$s(T_{2is}^0, p_2{}^0) - s(T_1{}^0, p_1{}^0) = 0 \tag{1.40}$$

$$\dot{m}_2 = \dot{m}_1 \tag{1.41}$$

2.5.7 Nozzle

$$T_2^{\,0} = T_1^{\,0} \tag{1.42}$$

$$s(T_{2is}, p_{amb}) - s(T_1^{\,0}, p_1^{\,0}) = 0 \tag{1.43}$$

$$\Delta h_{tot/stat-is} = h(T_{2is}) - h(T_1^{\,0}) \tag{1.44}$$

$$\Delta h_{tot/stat} = \Delta h_{tot/stat-is}\eta_n \tag{1.45}$$

$$h(T_2) - h(T_1^{\,0}) - \Delta h_{tot/stat} = 0 \tag{1.46}$$

$$\dot{m}_2 = \dot{m}_1 \tag{1.47}$$

$$C_{m2} = \sqrt{2(-\Delta h_{tot/stat})} \tag{1.48}$$

$$A_2 = \frac{\dot{m}_2}{\rho_2 C_{m2}} \tag{1.49}$$

2.5.8 Overall engine performance parameters

$$\eta_{eng} = \frac{\dot{m}_f H_u}{P_{FPT}} \tag{1.50}$$

$$SFC = \frac{\dot{m}_f}{P_{FPT}} \tag{1.51}$$

2.6 Combustion Model

In section 2.5.4, a few basic equations valid for combustion chamber state variables calculation are exposed. However, the operating fluid changes in species composition across the combustor, and this leads to different gas properties at the GGT entry. To account for this variation, some chemical considerations are needed to relate combustion efficiency with gas composition.

Firstly, combustion is modeled as an infinitely fast exothermic reaction between the air and fuel; chemical kinetics is therefore neglected. The species employed are the same used for the air composition (see section 2.2) plus the ones

contained in the fuel. The stoichiometric reaction implemented for one mole of a generic fuel is written as follows:

$$C_x H_y + n_{O_2} O_2 \rightarrow n_{CO_2} CO_2 + n_{H_2O} H_2O \tag{1.52}$$

and thus the following constraints must hold:

$$n_{O_2} = \frac{\left(2n_{CO_2} + n_{H_2O}\right)}{2} \tag{1.53}$$

$$n_{CO_2} = x \tag{1.54}$$

$$n_{H_2O} = \frac{y}{2} \tag{1.55}$$

For example, when the fuel is dodecane, eq. (1.52) becomes:

$$C_{12}H_{24} + 18O_2 \rightarrow 12CO_2 + 12H_2O \tag{1.56}$$

Species not supposed to react, such as argon, are excluded from the chemical balance. In this combustion model, NO_x production is not taken into account; in fact, its effect on gas properties variation is very small and thus it is negligible when the scope of the model consists in calculating thermodynamic engine performance. An external routine able to predict NO_x values can be added to the model, but this will not affect thermodynamic performance calculations. Furthermore, some complex chemical phenomena, such as dissociation effects, which are typically significant above 2000 K, are also neglected.

Once the type of reaction (1.52) is known, it is possible to determine the stoichiometric fuel-air ratio f_{st}:

$$f_{st} = \frac{(xM_C + yM_H)}{n_{O_2} M_{O_2}} \, fm_{O_2} \tag{1.57}$$

The species not participating in the reaction have a final mass fraction *fmb* different from the initial one (*fm*) because, while not varying in their absolute mass fluxes, their new mass fraction *fmb* do vary due to the fact that new mass is added by fuel injection. So, for those species which are not supposed to react, we have:

$$fmb = \frac{fm}{1+f} \tag{1.58}$$

For the calculation of the species that take part in the reaction, however, we must distinguish two separate cases, depending on whether the fuel-air ratio is less than or more than stoichiometric. Here only the first case will be analyzed, which represents the normal operating condition of excess air combustion, common to all aircraft engines.

Therefore, in excess air conditions, one can divide the air mass in two parts, the first corresponding to the stoichiometric mass and the second related to the remaining part. The only reagent inside the air mass is stoichiometric oxygen, whose mass fraction, however, does not completely react, because combustion efficiency in real processes is never unitary. We define combustion efficiency as the fraction between burned fuel and total injected fuel:

$$\eta_{comb} = \frac{\dot{m}_{f-burned}}{\dot{m}_{f-injected}} \tag{1.59}$$

Note that this is also equal to the ratio between reacting oxygen and stoichiometric oxygen (i.e. the quantity of oxygen needed for an ideal combustion with $\eta_{comb}=1$). Therefore the net amount of reacted oxygen referred to the total mass composing the mixture can be defined as:

$$fmb_{O_2-reacted} = \frac{\frac{f}{f_{st}}\eta_{comb}}{(1+f)}\, fm_{O_2} \tag{1.60}$$

At this point, since we know the relationships between the moles of oxygen and the combustion products, we can derive the mass fractions of water vapor and carbon dioxide:

$$fmb_{CO_2} = \frac{fm_{CO_2}}{1+f} + fmb_{O_2-reacted}\frac{n_{CO_2}}{n_{O_2}}\frac{M_{CO_2}}{M_{O_2}} \tag{1.61}$$

$$fmb_{H_2O} = \frac{fm_{H_2O}}{1+f} + fmb_{O_2-reacted}\frac{n_{H_2O}}{n_{O_2}}\frac{M_{H_2O}}{M_{O_2}} \tag{1.62}$$

where the first terms on the right-hand side of the two equations describe quantities which are already present in the air mixture prior to combustion and

therefore are not products of the reaction. As far as the calculation of the final oxygen fraction, we have:

$$fmb_{O_2} = \frac{\left(1-\frac{f}{f_{st}}\right)}{1+f} fm_{O_2} + \frac{\frac{f}{f_{st}}(1-\eta_{comb})}{1+f} fm_{O_2} \tag{1.63}$$

where the first term on the right-hand side identifies the excess air oxygen and the second term represents the residual oxygen inside the stoichiometric air, unreacted due to a non-unitary combustion efficiency. Eq. (1.63) can be further simplified to obtain the following expression:

$$fmb_{O_2} = \frac{\left(1-\frac{f}{f_{st}}\eta_{comb}\right)}{1+f} fm_{O_2} \tag{1.64}$$

Finally, the mass fraction of unburned fuel is simply computed as:

$$fmb_{unburned} = f\frac{(1-\eta_{comb})}{1+f} \tag{1.65}$$

Even if all the chemical species present in the air entering the combustor are determined along with their mass fractions, it is not possible to accurately compute the composition of the unburned fuel. In fact, at high temperatures the hydrocarbon chains tend to decompose in much simpler compounds. This phenomenon depends strictly on the flame temperature and on the particular composition of the fuel. Clearly, the more complex the chain of hydrogen and carbon atoms composing the fuel, the greater the likelihood of finding unburned complex hydrocarbons. Normally, in the combustion process of aeronautical kerosene, for temperatures above 700 K, complex compounds like decane and dodecane decompose into simpler substances (such as methane, ethane, ethylene, butadiene, etc.). The simulations that will be presented throughout this thesis were carried out assuming $C_{12}H_{24}$ fuel type, using ethylene (C_2H_4) as the sole unburned species; this assumption preserves the same mass fraction of carbon atoms and hydrogen atoms as the starting fuel. The variation in the type of chemical species composing the unburned gases affects physical properties of the air mixture, such as the gas constant R, the molecular mass M, and the specific heat c_p. However, considering ethylene as the only species constituting the totality of unburned gases, even for different types of hydrocarbon, is reasonable for two reasons:

1. The unburned species are a limited percentage of the fuel flow only, which in turn constitutes a small fraction of the mixture.
2. At high temperatures, the above mentioned hydrocarbons do not differ greatly in terms of atomic composition and all their gaseous states have very similar specific heats.

Once the mass fractions of the different species composing the mixture are known, by using eqs. (1.5-1.6) and the simple rules for an ideal mixture of gases, the new coefficients are obtained for the calculation of c_p (and consequently also enthalpy and entropy), R and M related to the combustion products.

2.7 Off-Design Steady State Performance Calculations

In a turboshaft engine, various causes lead to a deviation from design conditions [3], such as:

1) variation of ambient conditions;
2) variation of fluid composition (humidity);
3) variation of flight Mach number;
4) variation of mechanical power requested from the external load (in our case the helicopter main rotor power);
5) variation of the rotational speed of the FPT.

It is important to note that the above mentioned deviations from normal operating conditions affect each single engine component in a different manner. The task of a good engine simulator is to fairly predict the efficiency change in each component, in order to accurately calculate overall engine performance. The action of virtually assembling the various engine components to predict engine behavior, respecting the physical laws of continuity, energy and momentum, is referred to as “matching”.

In TSHAFT, a single simulation can be performed including all the five variation effects listed above. To account for these variations, an off-design steady state solver is implemented which will be briefly exposed here below.

Compressor and turbine off-design performance is calculated employing different generalized characteristic maps, which are based on the principles of similitude. These principles state that single component performance can be uniquely determined by knowing at least two non-dimensional (or quasi-non-

dimensional parameters)[§]; the remaining variables are not independent and are fixed by the map values. For this reason, compressor and turbine maps are component-specific and can only be derived from experimental data; alternatively, they can be assumed using scaling techniques modifying existing data related to similar turbomachinery. Inside component maps, relations among a set of four quasi-non-dimensional variables are plotted. Following is a formal definition of the variables employed in component map building.

Pressure ratio:

$$r = \frac{p_2^{\,0}}{p_1^{\,0}} \text{ (compressor)} \qquad r = \frac{p_1^{\,0}}{p_2^{\,0}} \text{ (turbine)} \tag{1.66}$$

Corrected mass flow:

$$\dot{m}_{corr} = \frac{\dot{m}_1 \sqrt{T_1^0 / T_{ref}}}{p_1^{\,0} / p_{ref}} \tag{1.67}$$

where the reference values of pressure and temperature are the usual $p_{ref} = 101325$ *Pa* and $T_{ref} = 288.15$ *K*.

Corrected Speed relative to Design Point (or simply Corrected Speed):

$$N_{corr} = \frac{\dfrac{N}{\sqrt{T_1^0 / T_{ref}}}}{\dfrac{N_{des}}{\sqrt{T_{des}^0 / T_{ref}}}} \tag{1.68}$$

Total-to-total Isentropic efficiency:

$$\eta = \frac{\Delta h_{is}^0}{\Delta h^0} \text{ (compressor)} \qquad \eta = \frac{\Delta h^0}{\Delta h_{is}^0} \text{ (turbine)} \tag{1.69}$$

As anticipated above, when a particular component map is not known, a scaling procedure on existing and publicly available generalized maps is applied

[§] This is true for a specific value of the Reynolds number; however, some empirical relations are available in the literature, which can be used to apply modifications to component maps depending on the value of the Reynolds number.

with the aim to produce an approximate map suitable for the particular engine studied. An example of compressor and turbine characteristics can be found in the following sections. Moreover in appendix A, a more thorough description of the analytical method employed in building component maps from raw data and the scaling procedure applied is given; see [4] for an additional discussion on the subject. The remaining components, without rotating elements, are simulated without employing maps; instead, the possibility to change their efficiency parameters directly is given.

A matrix method is used to solve for the non-linear equations resulting from formalization of the matching problem (see also Walsh and Fletcher [5]). In the matching problem, the values of corrected mass flow and power predicted by the thermodynamic relationships are compared with those obtained through characteristic map interpolation; a Levenberg-Marquardt optimization algorithm [6] performs iterations until the difference between these values is less than the requested tolerance (as shown in Figure 2.3). This is the way in which the laws of continuity and energy conservation are implemented for steady state operation. In fact, the following constraints have to be contemporarily satisfied [7]:

$$m_{corr} = m_{corrcar} \text{ (for every component modeled with a characteristic)} \quad (1.70)$$

$$P_{GGT} = P_{comp} \quad (1.71)$$

$$P_{FPT} = P_{load} \quad (1.72)$$

Once all the relationships between state variables and performance parameters are defined, a system of the type $\boldsymbol{f(x) = 0}$ is solved, where $\boldsymbol{f}$ is a vector-valued error function (matching constraints) and $\boldsymbol{x}$ is the vector of the variables (matching guesses). The solution is obtained with a Levenberg-Marquardt optimization algorithm which minimizes the constraint errors. The number of equations to be solved in the system depends on the number of components to be matched. For example, Figure 2.3 represents a typical double spool turboshaft engine with the first shaft linking the compressor to the gas generator turbine, and the second shaft delivering power from the free power turbine to the external load (which can be represented by a helicopter rotor, a propeller, etc.). In this case, once the ambient conditions are fixed, if we want to know the performance and the power output at a particular fuel flow rate, we need to solve a system of four equations in four unknowns. The first three are based on the continuity principle eq. (1.70): the mass flow rate calculated with thermodynamic relations must be

the same as the one derived from the component map for either the GGT and the FPT. In addition, continuity must be preserved also in the nozzle, in which the entering mass flow must be compatible with the defined nozzle exit area and thermodynamic conditions (pressure at the exit is assumed to be ambient pressure, when the flow is subsonic). The fourth equation (1.71) is defined by the energy conservation at the gas generator spool. To solve the system iteratively we need to use initial values for the following four unknowns: beta (a map construction parameter, see Appendix), corrected speed, and the pressure ratios of both turbines (GGT and FPT). In this way, given a particular fuel flow rate, engine off-design performance is uniquely determined. Instead, if we want to know engine performance starting from a known value of the FPT power load (a typical problem in helicopter simulation), an additional equation is needed, eq. (1.72), along with another unknown, which in this case can be fuel flow or, alternatively, the combustor exit temperature.

The introduction of additional components and features in the simulation require additional equations and additional unknowns. A typical increase in model complexity can be due to, for example: higher number of compressors and turbines on different spools; introduction of compressor bleeds; compressor inlet flow distortion simulation. TSHAFT is implemented in a way that it automatically recognizes the number of components and features in order to be able to solve problems of increasing complexity (for example, any arbitrary number of spools can be set). This comes obviously with additional computational cost; however, grace to the matrix method implemented, the number of function evaluations are minimized along with the computational time needed to solve the system.

If the matching problem is correctly set, the off-design steady state solver finds a unique solution. As said in section 2.5, the only way to fix the geometry of a particular turboshaft engine is by performing a Design Point simulation, which is later used by the off-design solver to scale component maps. Following this, the user has to choose the ambient conditions (flight Mach number, ambient temperature and pressure) and the external power load requested by the engine. This input data, along with other component efficiencies which can be tuned for the off-design mode, determines a unique possible air mass flow rate passing through the engine and therefore identifies a single operating point on every component map.

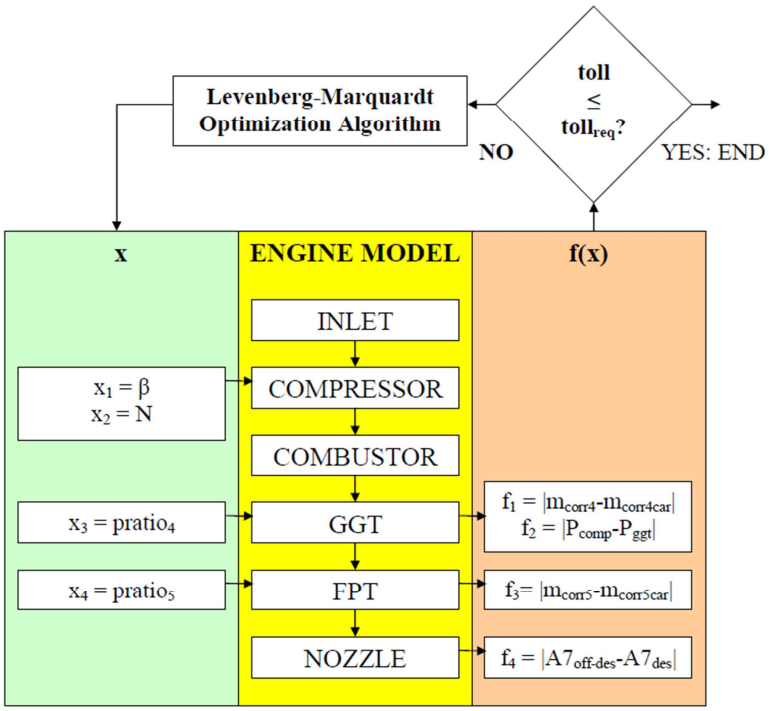

Figure 2.3. Matching problem solution: matrix method used by the Off Design solver for the turboshaft engine represented in Figure 2.1.

2.8 References

[1] A. M. Y. Razak, *Industrial Gas Turbines*, Woodhead Publishing LTD 2007.

[2] http://webbook.nist.gov/chemistry (last consultation Jan. 2014).

[3] H. I. H. Saravanamuttoo, G.F.C. Rogers and H. Cohen, *Gas Turbine Theory*, Pearson Prentice Hall, 2001.

[4] G. A. Misté and E. Benini, *Improvements in Off Design Aeroengine Performance Prediction Using Analytic Compressor Map Interpolation*, *International Journal of Turbo & Jet-Engines*, Vol. 29, No. 2, ISSN (Online) 2191-0332, ISSN (Print) 0334-0082, DOI: 10.1515/tjj-2012-0012, May 2012.

[5] P. P. Walsh and P. Fletcher, *Gas Turbine Performance*, Blackwell Publishing, 2004.

[6] D. Marquardt, *An Algorithm for Least Squares Estimation of Nonlinear Parameters*, Journal of the Society for Industrial and Applied Mathematics Vol. 11, No. 2, 1963, pp. 431-441.

[7] H. I. H. Saravanamuttoo, *Overview on basis and use of performance prediction methods*, in "Steady and Transient Performance Prediction of Gas Turbine Engines", AGARD Lecture Series 183, 1992

Chapter 3

TSHAFT Code Validation

3.1 Validation Typologies

In order to evaluate TSHAFT code predicting capabilities, three different types of validation were carried out, with increasing levels of reliability.

In the first phase, described in section 3.2, three blind test cases were analyzed for comparison with the NLR gas turbine simulation software, GSP [1]. For each case the same input data and the same engine configuration were employed for both TSHAFT and GSP, and a final comparison was made between the numerical results obtained using the two different codes.

A second validation of the code (section 3.3) was carried out in the framework of the EU funded Project *Clean Sky Green Rotorcraft 2*, in collaboration with Agusta-Westland. TSHAFT was employed to assess the installation performance of the ERICA conceptual tilt-rotor (*Enhanced Rotorcraft Innovative Concept Achievement*). One of the project subtasks consisted in building and calibrating a reliable turboshaft engine model. The greatest effort to this aim was concentrated on compressor and turbine maps derivation and construction. Since no experimental data related to the ERICA turboshaft engine were available in literature, comparison of estimated performance results were made between TSHAFT and the manufacturer's Engine Deck.

In addition to these efforts, the code was validated directly against engine experimental measures made by Ballin at NASA Ames [2]. The specified engine, a slightly modified version of the GE T700, was the engine chosen to assess the worthiness of the VSR concept exposed in Chapter 5; in fact, the GE T700 is the engine mounted on the standard version of the UH-60 Black Hawk. For this reason, the validation will not be presented in this chapter, but will be exposed later along with the description of the UH-60 helicopter performance model.

3.2 Validation vs. GSP

In this phase, three models of aeronautical engines are analyzed: a two spool turboshaft engine, a more complex three-spool turboshaft and a simple turbojet engine. Such models are blindly taken from the GSP engine library, which is given along with the GSP code. For each engine model, various simulations are run for different power load off-design steady state conditions. The starting point of the set of simulations is the design point of the engine, and then a sweep in the FPT power parameter, P_{FPT} (equal to P_{load} in steady state conditions), is made to construct the engine operating line and assess the engine performance variation.

Note that the simulations for all the three cases are carried out supposing ground testing conditions, i.e. *Ma=0* and *h=0 m*.

Performance outputs by TSHAFT and GSP are compared in charts that are presented throughout the text.

3.2.1 Model n° 1

Engine configuration. The model consists of a turboshaft engine similar to the one illustrated in Figure 2.1 and Figure 2.3. It is composed of a single compressor and two turbines, a GGT driving the compressor and a FPT, which produces the power required by the external load. The design mass flow rate is *m=4.5 kg/s* and the design output power is P_{load}*=1250 kW*. A schematic representation of the engine model as it is built in TSHAFT is visible in Figure 3.1, while its homologous made in GSP can be observed in Figure 3.2.

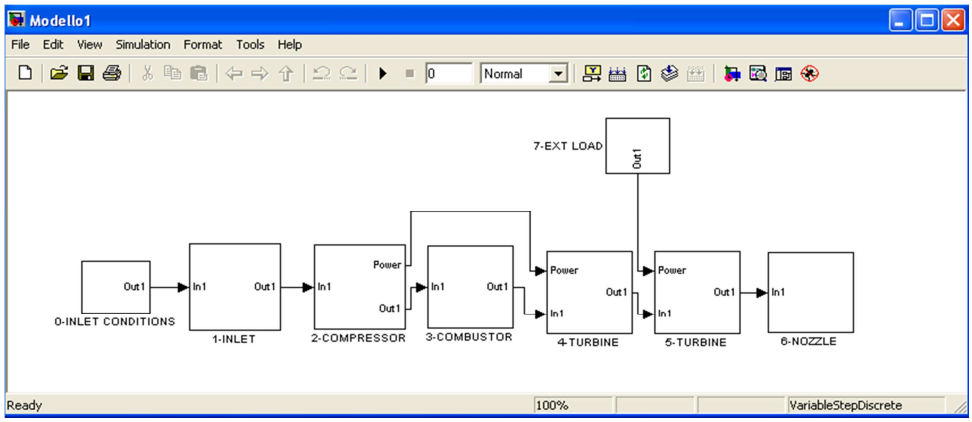

Figure 3.1. Model n°1: turboshaft engine built with TSHAFT.

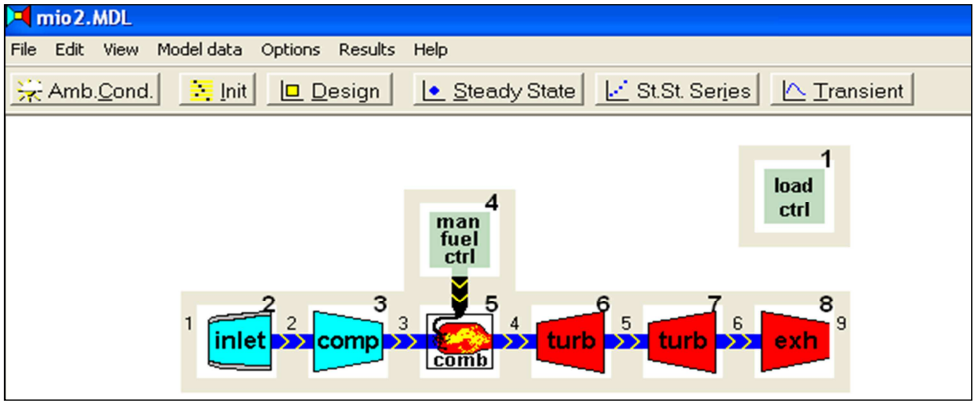

Figure 3.2. Model n°1: turboshaft engine built with GSP.

Using the same input data in both the programs, for the calculation of the design and off-design conditions, a first simulation is performed to obtain the operating line of the engine.

The required tolerance on the relative errors for the error function ***f(x)*** for both models is set at a value of 10^{-4} (the same holds also for the next two models).

It is worth noting that GSP is not able to calculate engine performance if the external power required P_{load} is used as a variation parameter (the one which allows us to move along the operating line): there is no convergence despite a high number of iterations. Within TSHAFT, instead, there are no convergence problems. For this reason we change the variation parameter both in GSP and TSHAFT and we use as input vector the maximum cycle temperature T_{max} instead of P_{load}. With this new off-design variation parameter the simulation rapidly converges also using GSP.

Results and comparison between operating lines. The comparison between the operating lines calculated using TSHAFT and GSP, for each map characteristic, is visible in Figure 3.3-8; since the comparison between component maps is very similar for all the three simulated models, it is presented only for model n°1. For the remaining models we will focus almost exclusively on the relative error charts which highlight the deviations between output given by TSHAFT and GSP.

Figure 3.3-4 show considerable similarities: in fact, there are no appreciable differences in the charts produced by TSHAFT and GSP.

Figure 3.5-6 instead show the existence of a non-negligible discrepancy, so that the GGT map characteristic produced by TSHAFT seems to be rescaled in a different way with respect to its homologous in GSP. The main reason lies in the different method of calculating the corrected mass flow m_{corr}. TSHAFT, similarly

to other methods proposed in the open literature [2],[3],[4], employs the definition of m_{corr} used in eq. (1.67), using as reference pressure and temperature the standard values $p_{rif}=101325\ Pa$ and $T_{rif}=288.15\ K$. GSP, initially, from its design point results related to the first stations of the model, seems to use the same definition of m_{corr}, with the same standard values. However, this is no longer true in the following stations, and especially at the entry station of the GGT. In fact, the value of m_{corr} output by GSP is different from the value obtained combining the same GSP output values of p^0, T^0, m following definition (1.67). The discrepancy is not so high, but it cannot be explained by a simple problem of numerical cancellation (the relative error between TSHAFT and GSP values is around 4%). It is also clear that this difference cannot be caused by the use of static instead of total values. For this reason the author is convinced that GSP defines m_{corr} in a different way from what is suggested in the literature, or maybe there is a slight error in GSP's computation of m_{corr}.

Anyway, a different definition of m_{corr} does not affect overall engine performance, as is well evidenced in the compressor map, where TSHAFT design point (the first operating point on the right) is almost coincident to the same on GSP. Therefore, this little deviation between the two codes is only responsible for a different scaling of GGT and also FPT maps (visible in Figure 3.7-3.8).

Relative Errors. Relative errors are always calculated for every model as the relative difference between the generic values calculated with GSP (G_{GSP}) and those calculated with TSHAFT (G_{TSHAFT}):

$$err = \frac{G_{GSP} - G_{Tshaft}}{G_{GSP}} \tag{3.1}$$

Thus, they may be positive or negative, and in charts they are presented in percentage values for convenience. The errors that are shown below for each of the three models are those related to the power P_{load} and the specific fuel consumption SFC, expressed as a function of gas generator corrected speed N_{corr} calculated by GSP. These errors, as well as being those of greatest interest to the user, turn out to be also the highest errors among all the variables considered.

Now, if we apply these concepts to model n°1, we obtain the charts given in Figure 3.9-11. The power load calculated by TSHAFT is slightly lower with respect to GSP when the operating point is located next to the design point (error well below 5%). In contrast, for points below $N_{corr}=0.95$, P_{load} is predicted to be much higher than that calculated by GSP.

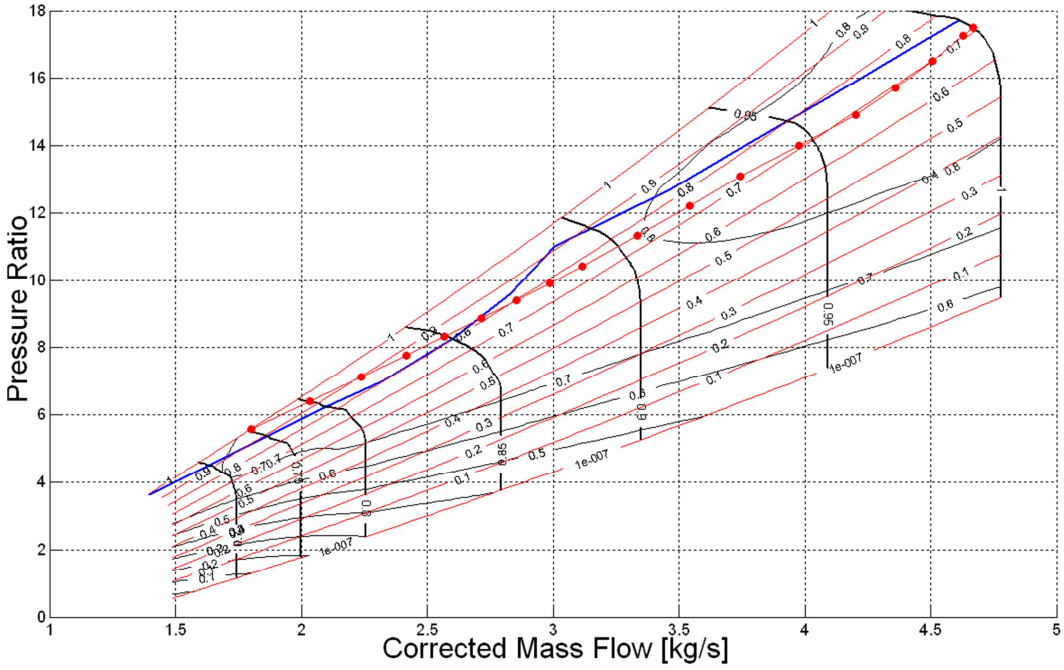

Figure 3.3. Model n°1: Engine operating line on compressor map (TSHAFT).

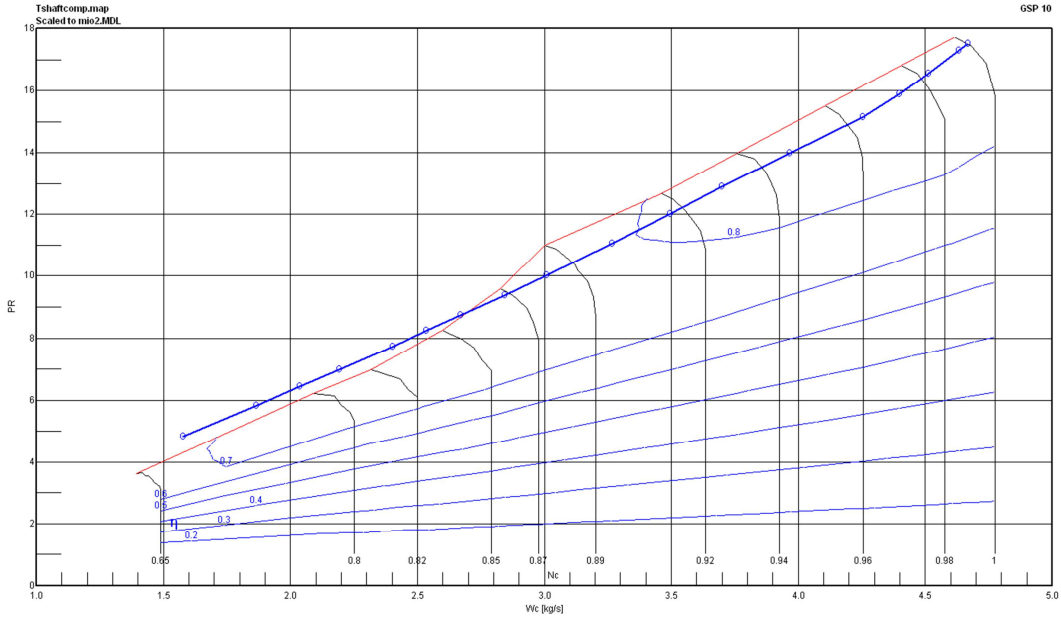

Figure 3.4. Model n°1: Engine operating line on compressor map (GSP).

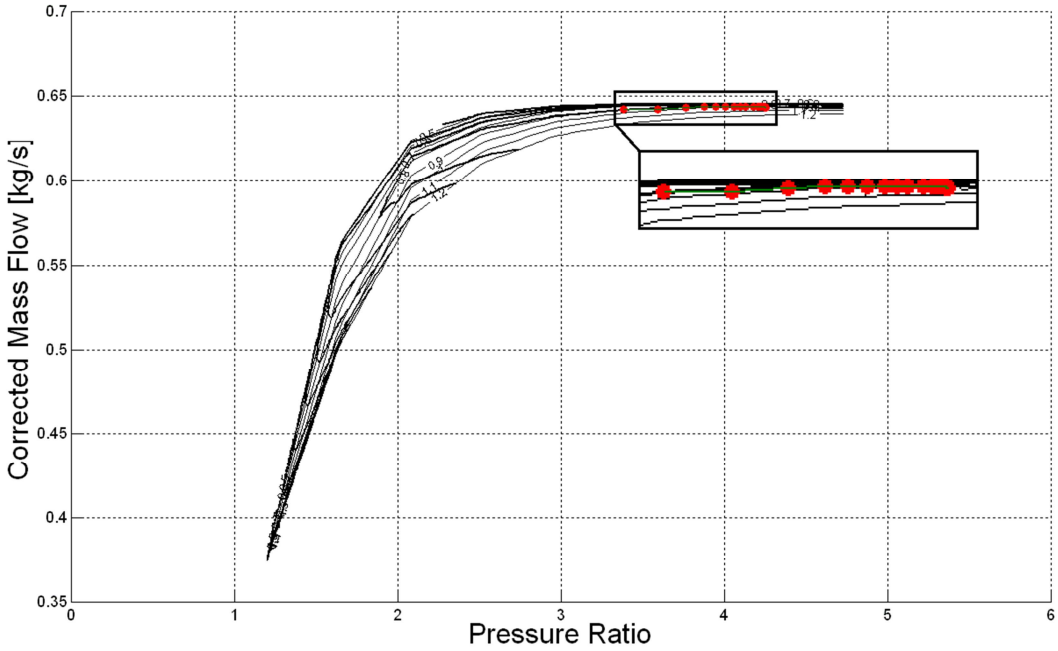

Figure 3.5. Model n°1: Engine operating line on GGT map (TSHAFT).

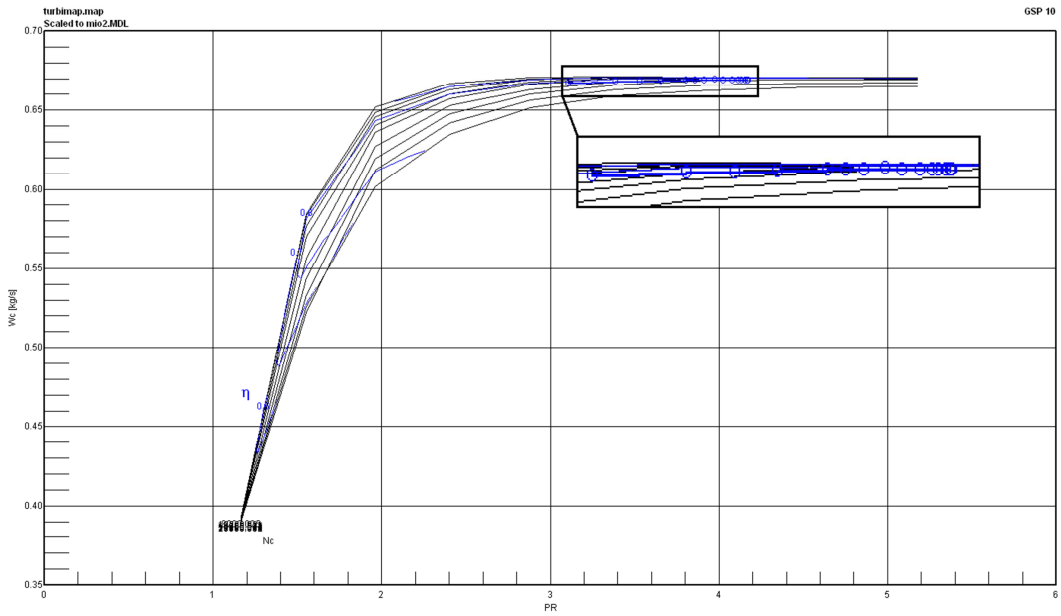

Figure 3.6. Model n°1: Engine operating line on GGT map (GSP).

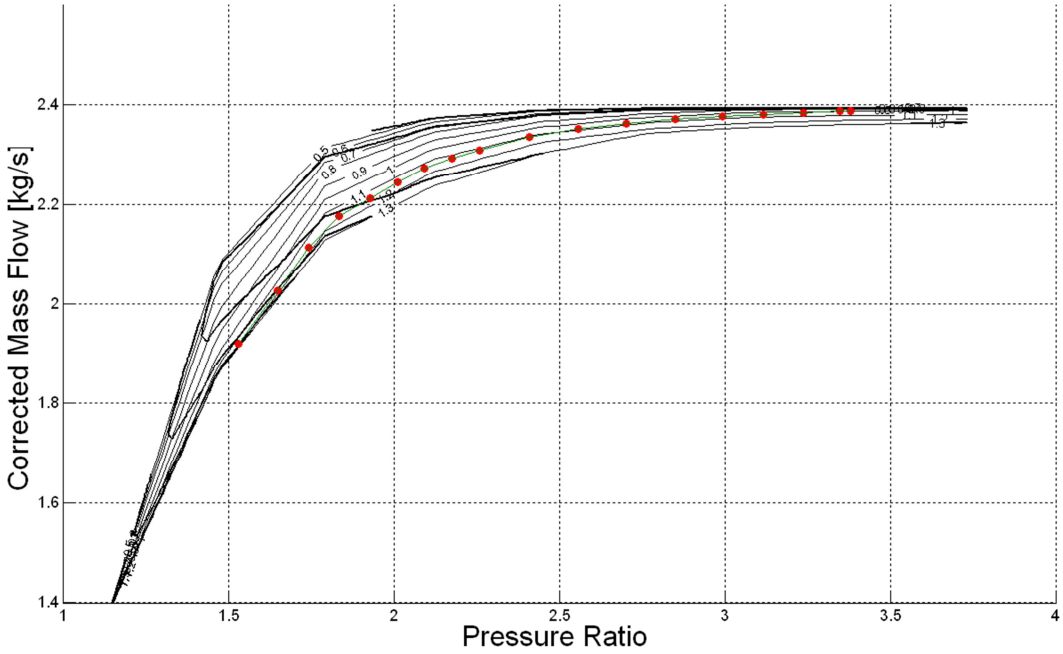

Figure 3.7. Model n°1: Engine operating line on FPT map (TSHAFT).

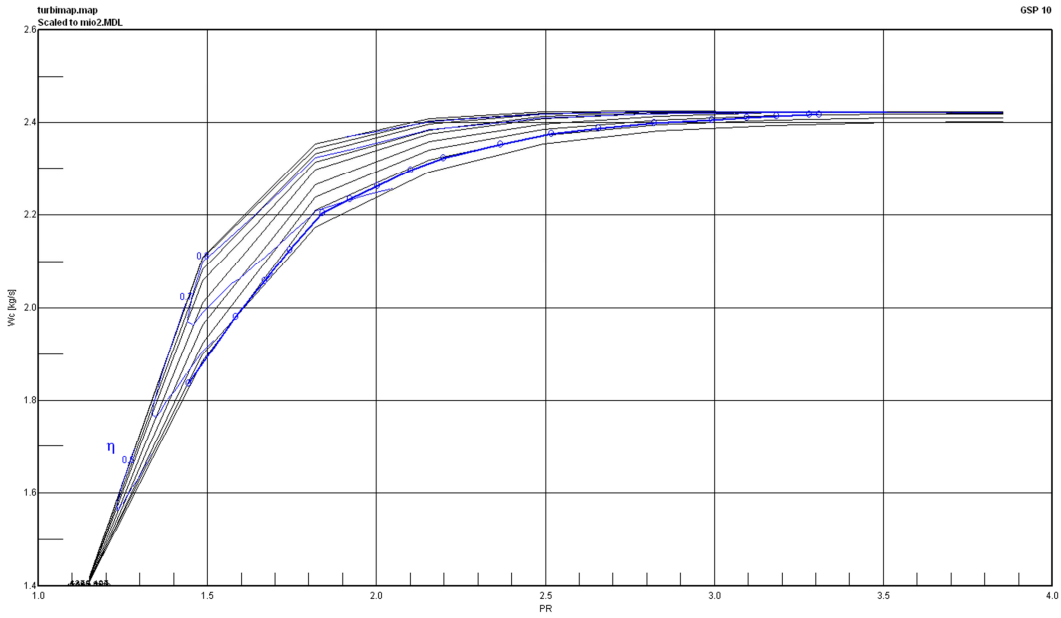

Figure 3.8. Model n°1: Engine operating line on FPT map (GSP).

As long as the operating points are far from the surge line (see Figure 3.3-4), the relative errors are kept below 15%; instead, the points that lie above the surge line present an error up to 35%. The reasons for this error increase are mainly three:

- Decrease in the value of P_{load}: for low values of N_{corr} the FPT power decreases and, even assuming an almost constant absolute error, it is clear that the relative error increases only as a consequence of its definition.
- Point distance from the design point: it is intuitive to expect that the differences between the two off-design simulation codes are more relevant when simulating an operating point far from the design conditions. In fact, the theory implemented for design point simulations in both TSHAFT and GSP is almost the same (and the high compatibility of the results confirms this). On the contrary, the differences encountered in off-design simulations are due to a number of factors not present in design point simulations (such as numerical solving methods, map interpolation procedures, etc.).
- Operating points above the surge line: for points on the compressor map lying above the surge line (in either one of the two maps output by TSHAFT and GSP) TSHAFT employs linear extrapolation. We do not know what kind of method is used in GSP to extrapolate compressor map values, but it surely produces different values. However, performance calculation for points beyond the surge line cannot be considered fairly accurate for both the engine simulation codes.

The *SFC* relative error presents a specular behavior with respect to the P_{load} error. From Figure 3.11 it is observed that for the majority of the operating points the fuel flow rate computed by TSHAFT is greater than that calculated by GSP; in fact, as expected, the relative error trend on m_f is very similar to that on P_{load}. When $N_{corr} < 0.9$, TSHAFT outputs a SFC value lower than GSP, which means that the greater fuel flow injected corresponds to a higher FPT power output with respect to GSP, thus leading also to better overall engine performance. For $Ncorr > 0.9$, instead, the overall performance calculated by GSP is revealed to be better than the one computed by TSHAFT. Actually TSHAFT, compared to GSP, predicts a milder decrease in engine performance at low N_{corr}, but outputs a lower performance in proximity of the design point.

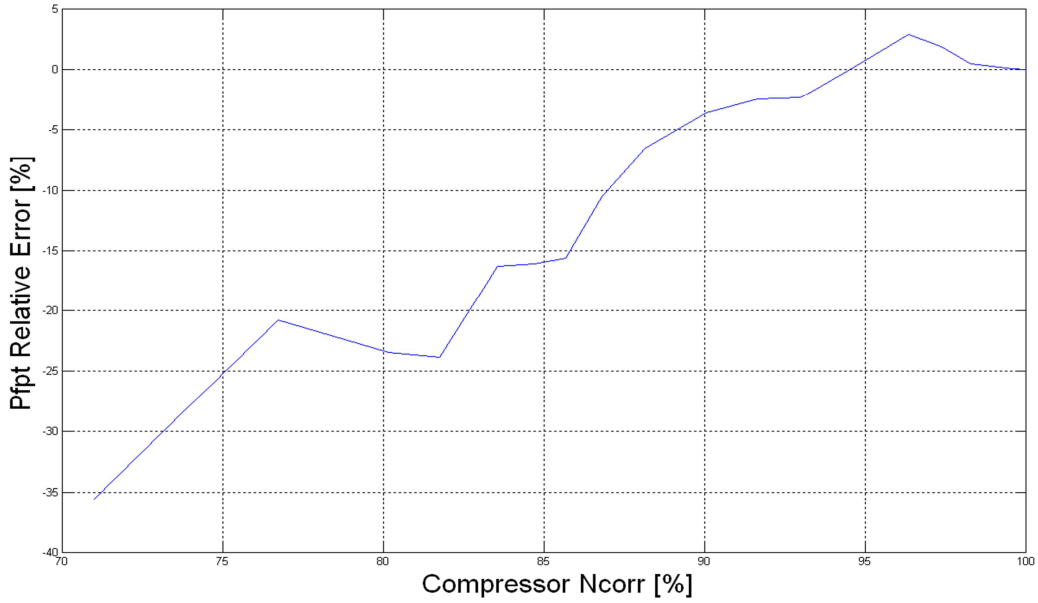

Figure 3.9. Model n°1: FPT power relative error between TSHAFT and GSP models.

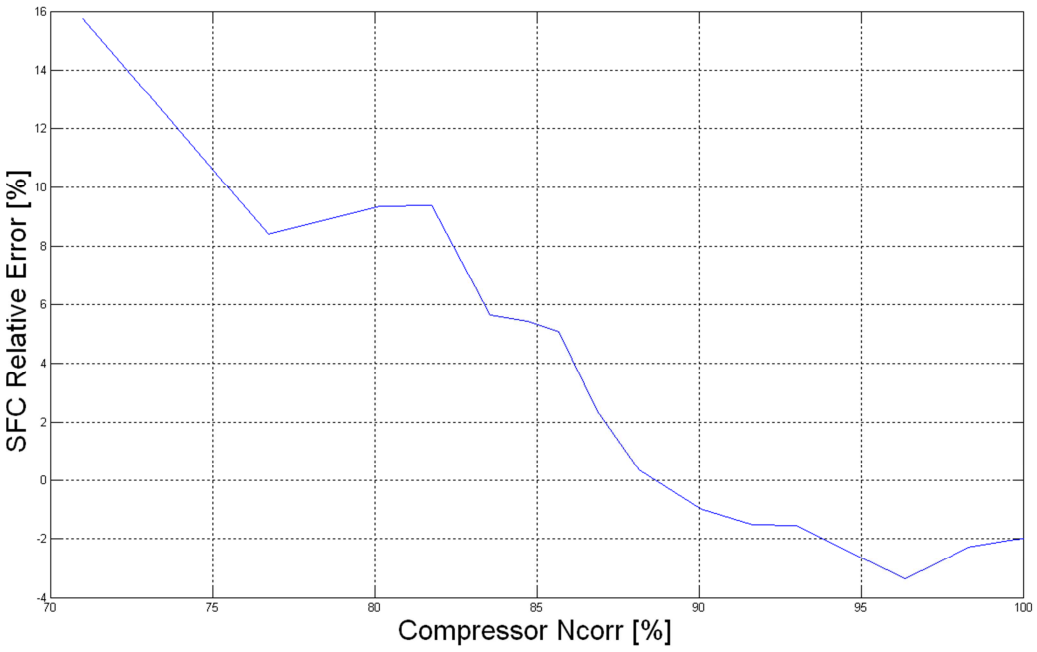

Figure 3.10. Model n°1: specific fuel consumption relative error between TSHAFT and GSP models.

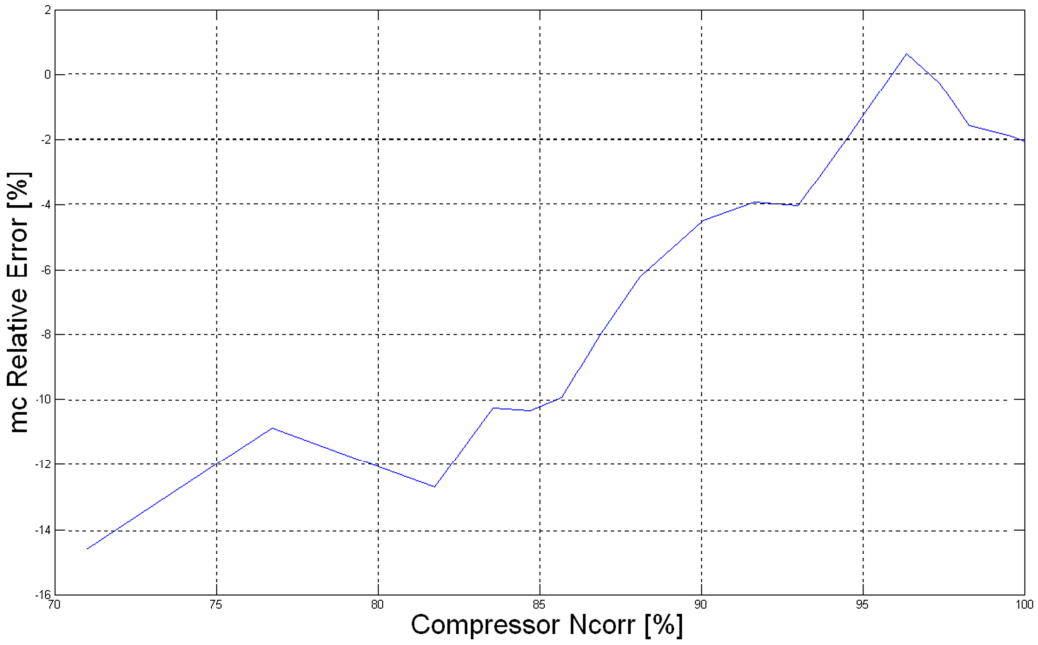

Figure 3.11. Model n°1: fuel mass flow relative error between TSHAFT and GSP models.

3.2.2 Model n° 2

Engine configuration. The model represents a three-spool turboshaft engine. On the first shaft the low-pressure compressor is linked together with a low-pressure GGT. On the second shaft the high-pressure compressor is coupled to the high-pressure GGT. This gas generator group is followed by a FPT, which is linked to the external load by another independent shaft.

The design mass flow rate is $m=4.5\ kg/s$ and the design output power $P_{load}=1250\ kW$. These values are the same as those chosen for model n°1; however, the different configuration of the engine must produce different results with respect to model n°1. In fact, the use of two independent spools for the gas generator is expected to improve engine performance; verification of this occurrence would be an additional validation for both the two simulation codes.

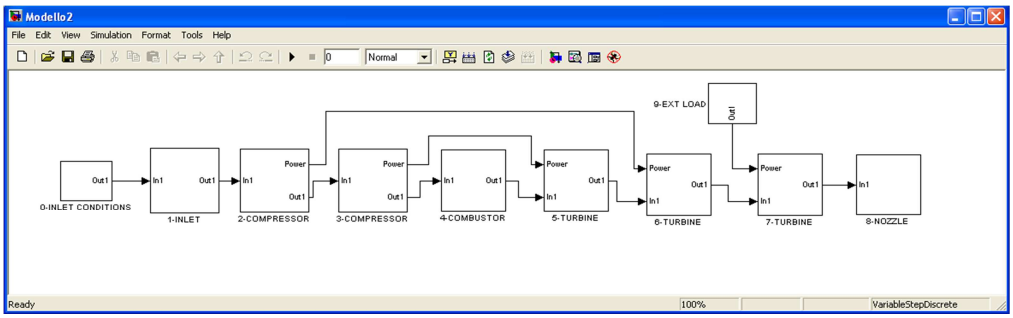

Figure 3.12. Model n°2: turboshaft engine built with TSHAFT.

A schematic representation of the engine model as it is built in TSHAFT is visible in Figure 3.12.

Results. As can be seen from a quick observation of Figure 3.13-15, engine overall performance calculated for model n°2 is always higher than that computed for model n°1. This holds true for either TSHAFT and GSP outputs, especially for low values of N_{corr}, where the independence between the two spools, in far from design point off-design conditions, brings major benefits to engine performance.

Relative Errors. The error trends are different from those reported in model n°1. It can be said, however, that the curves relating to different performance parameters again maintain the same shape relationships with each other: the P_{load} error curve is similar to a scaled m_f error curve, while the SFC error is almost their specular image.

Compared to model n°1, the map zone where P_{load} calculated by GSP is greater than that calculated by TSHAFT is greatly enlarged. If in model n°1 this occurred when $N_{corr} > 0.95$, in this case it occurs throughout the region in which $N_{corr} > 0.85$.

Anyway, we observe that in model n°2 the relative errors in the worst case reach a deviation of 7% (for values related to operating points far from the design point), which can be taken as a sign of good compatibility.

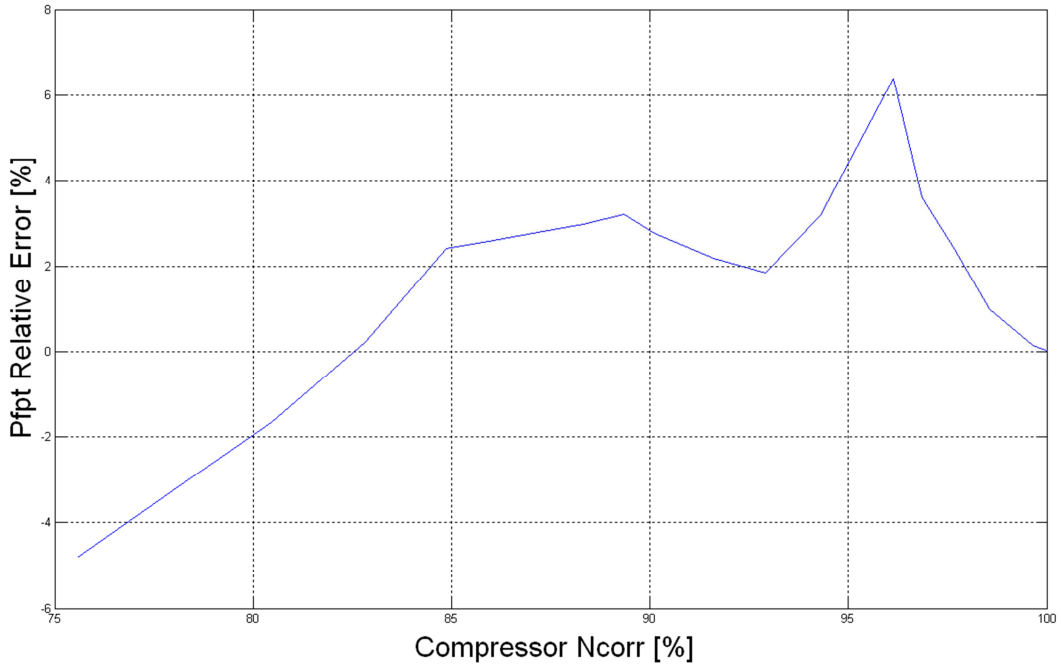

Figure 3.13. Model n°2: FPT power relative error between TSHAFT and GSP models.

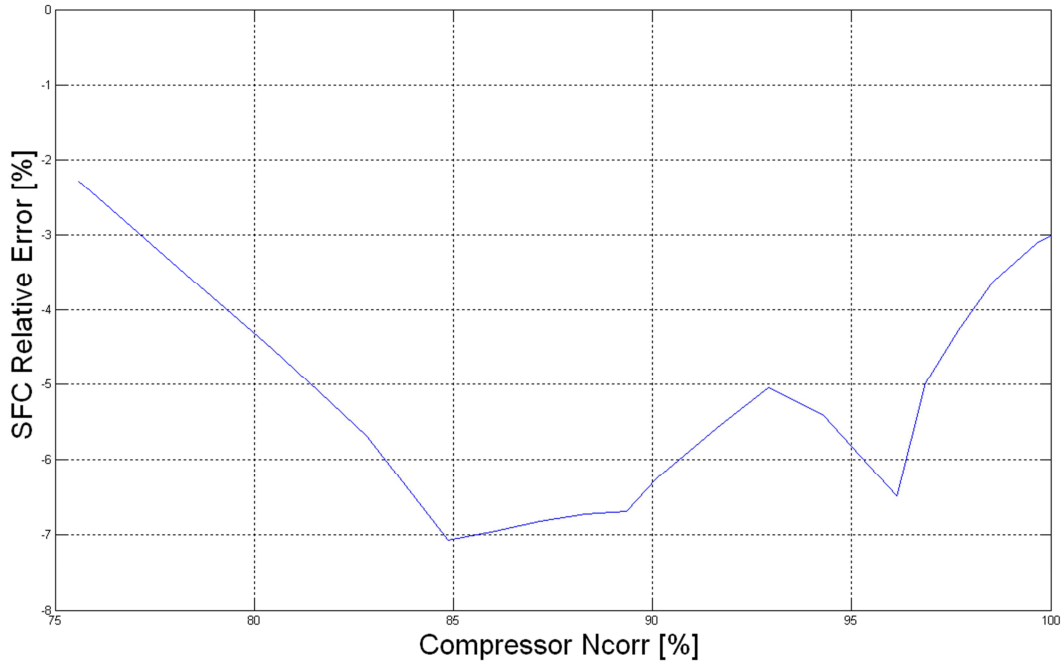

Figure 3.14. Model n°2: specific fuel consumption relative error between TSHAFT and GSP models.

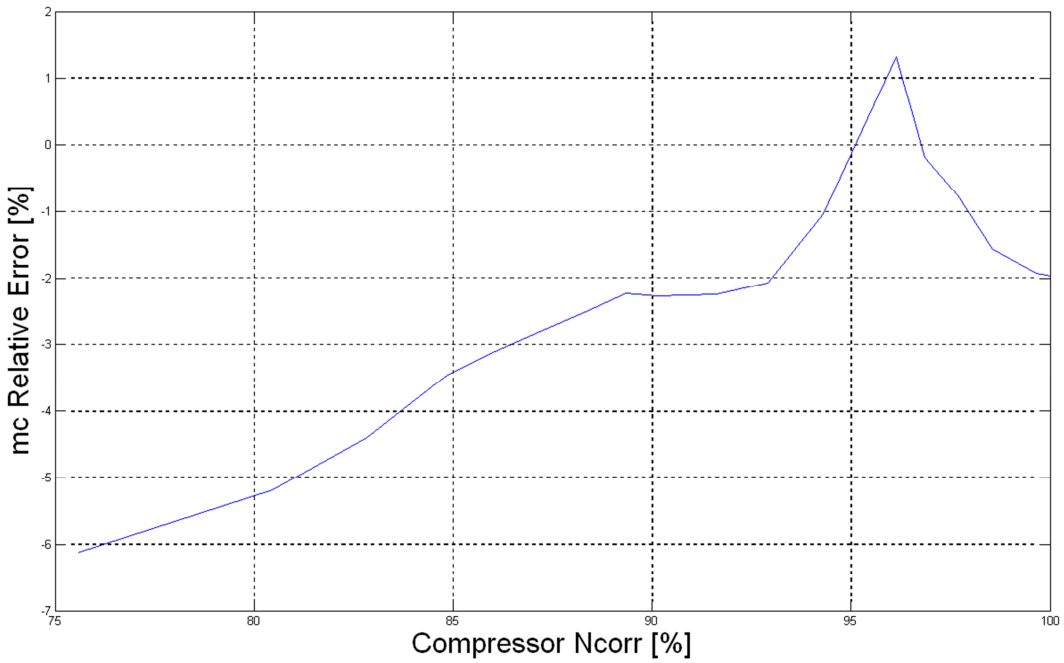

Figure 3.15. Model n°2: fuel mass flow relative error between TSHAFT and GSP models.

3.2.3 Model n° 3

Engine configuration. The model represents a single spool turbojet engine, with a single compressor and a single GGT, as shown in Figure 3.16.

In this case, there is no power delivered to an external load, since the total enthalpy at the exit of the GGT is converted into kinetic energy in the nozzle. New performance parameters are used in relative error charts, like thrust F and compressor power P_{comp}; in addition, specific fuel consumption is now calculated as the ratio between m_f and F.

The design mass flow rate is $m=19.9\ kg/s$ and the design thrust is $F=9400\ N$.

Results. The performance outputs given by the two codes are physically plausible but are not presented for brevity.

Relative Errors. The charts show the usual tendency of the relative errors to increase with the distance from the design point. As happened before, the performance parameters, when near to the design point, present a positive relative error, which then becomes negative as moving away from the design point.

The SFC is found to have low errors (5% maximum in absolute value), especially for medium values of N_{corr}, because in this zone the error on fuel flow and thrust, for the particular definition of SFC, compensate each other.

The highest deviations are found in compressor power for low N_{corr}, reaching 16%.

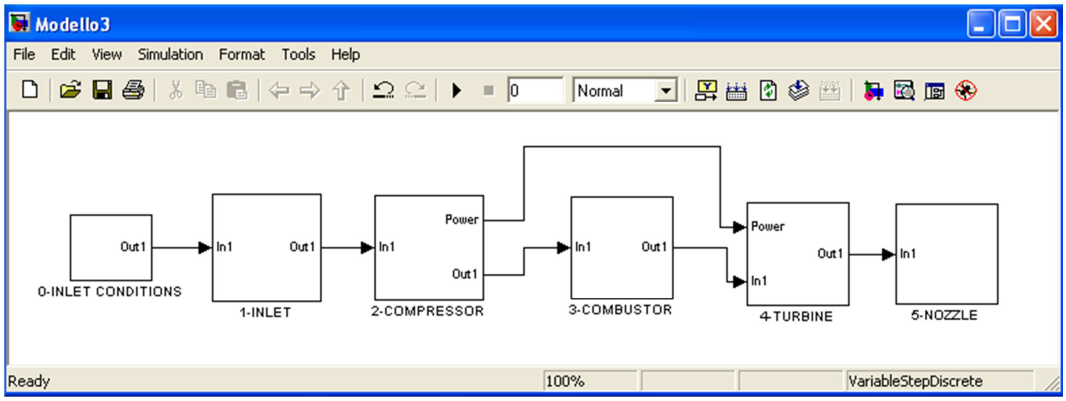

Figure 3.16. Model n°3: turbojet engine built with GSP.

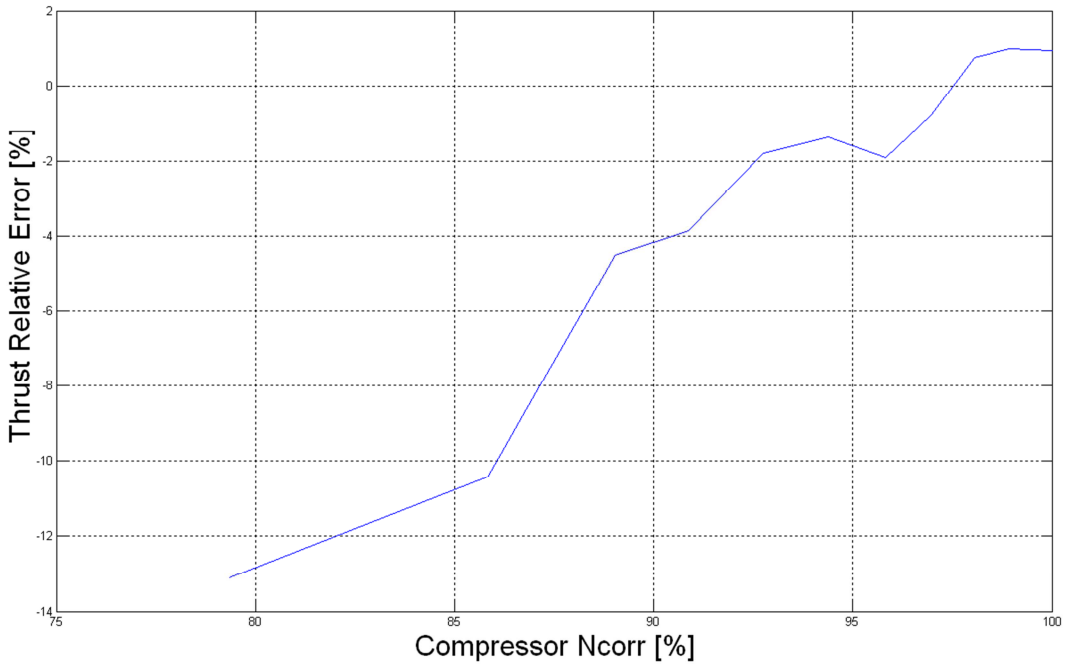

Figure 3.17. Model n°3: thrust relative error between TSHAFT and GSP models.

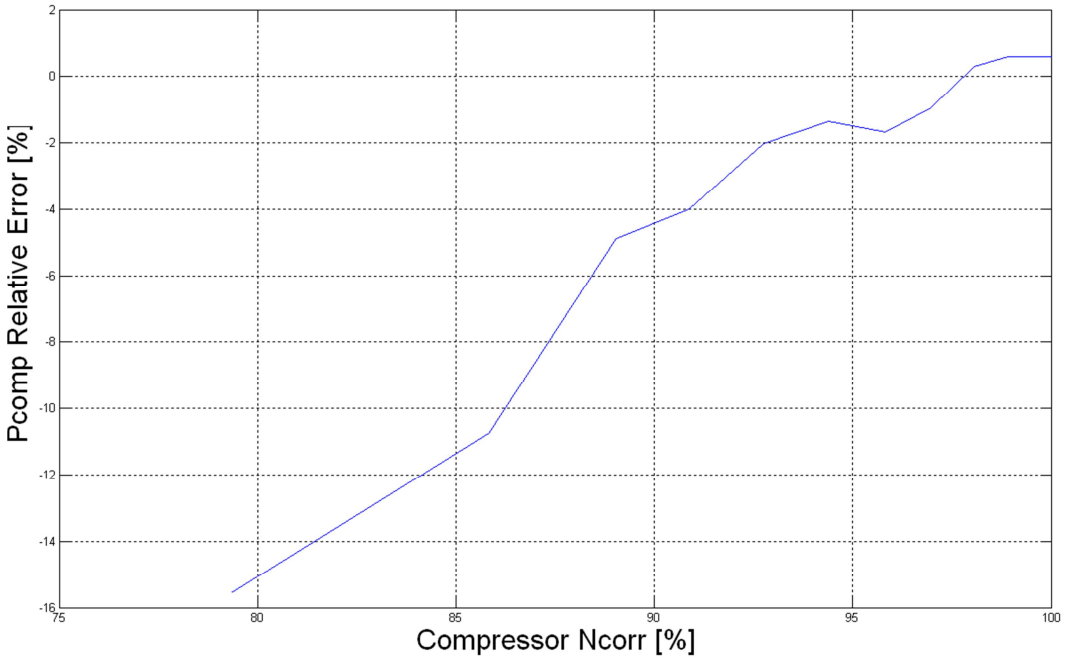

Figure 3.18. Model n°3: compressor power relative error between TSHAFT and GSP models.

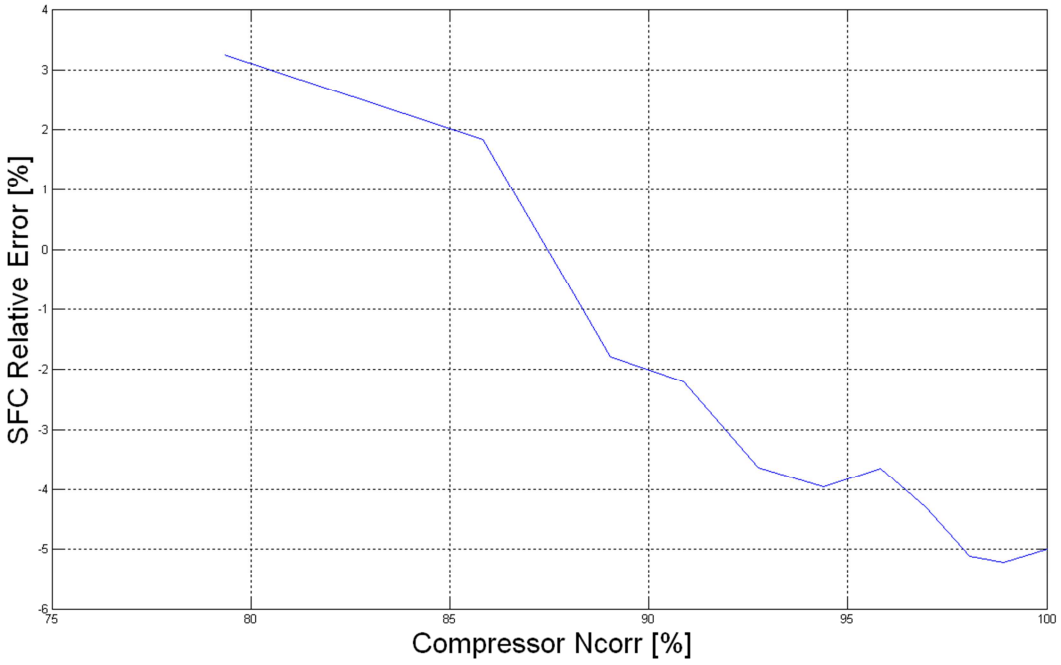

Figure 3.19. Model n°3: specific fuel consumption relative error between TSHAFT and GSP models.

3.2.4 Relative error comparison between the three models

In addition to the relative errors listed above, we can also define a single parameter able to detect the general degree of adhesion between TSHAFT and GSP models. It is therefore defined a mean relative error, in order to provide a statistical information about what is the average percentage difference between the results produced by the two simulation codes. To this purpose, a number n of variables of practical interest was taken, and the mean of the absolute value of their relative errors was computed:

$$err_{mean} = \frac{\sum_{i=1}^{n} |err_i|}{n} \tag{3.2}$$

Such value can only be positive, and it represents a possible index of the general deviation between the results obtained using the two codes. We have seen in the previous sections how the errors for almost all models tend to increase with distance from the design point and we understood the main reasons for this. There is still an oscillating component of the error that it is difficult to attribute to some specific cause. However, the numerical methods employed by GSP to solve the matching problem, map interpolations, variable c_p calculation and the combustion

process, are unknown. The differences between the two codes exist in each of these subjects, but we are unable to determine which of these affect the errors between the codes the most. Anyway, using the mean relative error definition, we are able to compare the three models, as can be observed in Figure 3.20.

In model n°1, the mean relative error tends to increase with the decrease of N_{corr}, thus confirming the usual trend seen before. It remains well below the 10%, even for points lying above the surge line.

In model n°2 the mean relative error has a much more constant behavior than in model n°1, and has also a lower value. This is largely due to the extension of the number of state variables used to calculate the error. In fact, with much more stations than the previous model, and noting that usually state variables (pressure, temperature, etc.) show lower deviations than performance parameters, the mean error is brought down by the higher number of state variables.

In model n°3 the mean relative error, even with few state variables used for its computation, remains low and does not exceed 5%.

In addition to the mean error analysis, we observe that the engine operating lines on map characteristics are very similar between the two codes, and both bring physically reliable results. Therefore, only a proper comparison with experimental data can determine which of the two codes, TSHAFT and GSP, better simulates engine performance. Anyway, from the results obtained by the analysis of these three models it is possible to state that a fairly acceptable compatibility between TSHAFT and GSP outputs is verified.

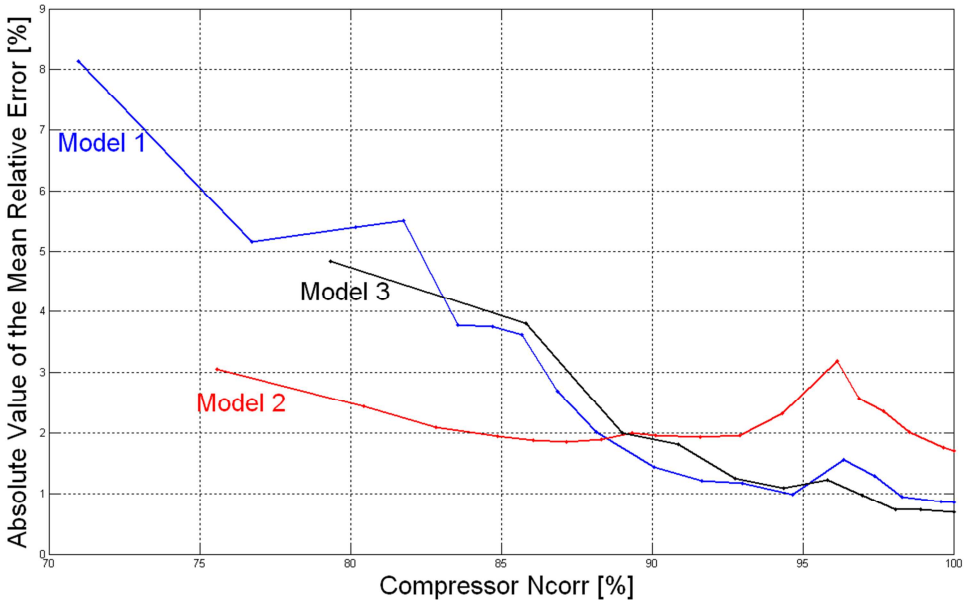

Figure 3.20. Comparison between the mean relative errors related to the three models.

3.3 Validation vs. ERICA Engine Deck

The second step of the code validation procedure is given by the analysis and setup of a reliable model for the candidate turboshaft engine for the ERICA tilt-rotor. As can be seen in Figure 3.21, it is a three-spool turboshaft engine: on the first shaft (in orange) a low-pressure (LP) centrifugal compressor is linked together with a low-pressure axial GGT; on the second shaft (in red) a high-pressure (HP) centrifugal compressor is coupled to the high-pressure axial GGT; on the third shaft (in green) an axial FPT produces the power output for an external load (the convertible main rotor in the ERICA case).

The schematization of the model built in TSHAFT is visible in Figure 3.22. Note that a new component, the bleed duct, is added to the model in order to account for compressor air bleed effects.

To build a suitable model of the engine, data related to more than 1200 different simulations performed using the manufacturer's Engine Deck (ED) are used. Various off-design operating conditions are considered. The principal issues in building the model are listed below.

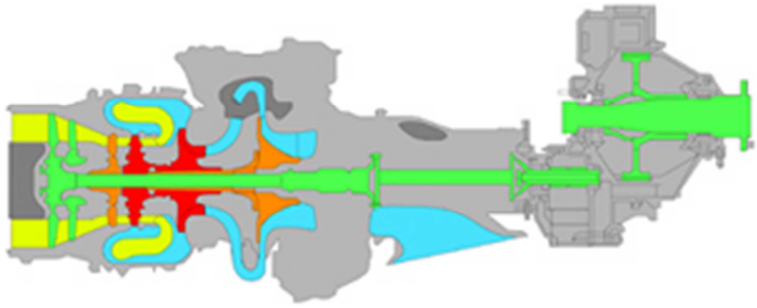

Figure 3.21. The turboshaft engine chosen for ERICA.

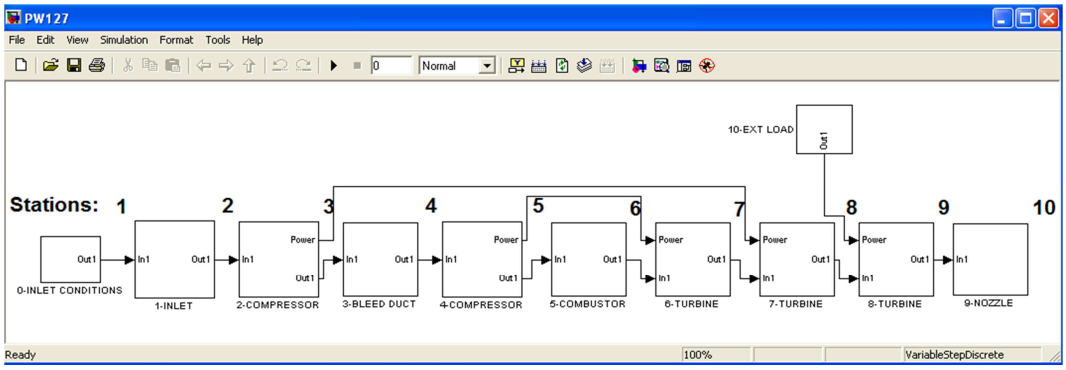

Figure 3.22. ERICA turboshaft engine model built using TSHAFT.

3.3.1 Design point selection

The design point, fundamental to fix the virtual geometry of the engine and its exhaust area, is arbitrarily selected as the corresponding ERICA cruise condition. This is the operating point used to scale component maps, when needed. Since the ED model does not account for installation losses, intake and nozzle efficiencies are set to unitary values to calibrate TSHAFT model correctly. This hypothesis will be held also for the subsequent off-design simulations.

3.3.2 Compressor maps

From the ED output, it is possible to estimate compressor off-design characteristics. In fact, the values of total pressure and temperature related to the entry and the exit conditions are computed by the ED for both the compressors. The same is applicable for the mass flow entering the engine and compressor rotational speed, which can also be found as ED outputs. As a consequence, corrected mass flow, corrected speed and pressure ratio for a specific off-design condition can be determined using eqs. (1.66-1.68). By manipulating data referred to multiple simulations, the corrected speed lines can be determined as explained in appendix A.

Tracing the efficiency lines is a bit more complicated, since the values of compressor efficiency are not given by the ED. However, by knowing both total temperature and pressure at the entry (p_1^0 T_1^0 and exit (p_2^0, T_2^0) stations, the efficiency values can be computed from comparison with the isentropic values of exit temperature. In fact, it is possible to numerically solve eq. (1.13), from which we derive the value T^0_{2is}: this is the value of compressor exit temperature for an isentropic transformation. By using the definition of enthalpy (1.5) we calculate the values of Δh^0 and Δh^0_{is}, and from eq. (1.69) it is possible to derive compressor efficiency η_{comp}.

The results of map interpolation procedure are visible in Figure 3.26-27 for both LP and HP compressors. It is worth noting that HP compressor map extension is considerably reduced with respect to LP compressor. The reason for this is given by the fact that the second compressor is much more constrained in operation than the first by other engine components, so that in steady state conditions the region in which all the operating points fall is extremely narrow. Moreover, the first compressor presents an extended map principally due to the presence of air bleeds, which are used to shift the engine operating line, and thus allow to explore a wider region of compressor operating conditions.

3.3.3 Compressor bleeds

From analysis of the ED results, the value of the net air mass flow at the compressor exit is not found equal to the flow entering the engine. This leads to the conclusion that somewhere inside the engine a certain quantity of air is withdrawn for various purposes.

Inside the ED output, a scheduled handling bleed variable is found which represents the fraction of air mass flow thrown away to maintain an acceptable stall margin for the LP compressor during off-design and transient operations. In fact, the most critical component which can be usually affected by stall is the LP compressor. The bleed valve responsible for ejecting air outside of the engine, as well explained in [5], is often located between LP and HP compressors, and is simulated in the TSHAFT model using the bleed duct component in Figure 3.22. For different operating points a different scheduled bleed is present; thus, for a correct simulation, an interpolation procedure is employed to determine the correct value of the bleed flows for every steady-state off-design condition. Bleed flows, as a fraction of the inlet mass flow, are closely related with pressure ratio, which in turn is linked to the surge margin. The relationship between these two variables for two different rotational regimes of the FPT, 100% (corresponding to design point N_{FPT} design speed) and 77%, is visible in Figure 3.23.

Note that the bleed valves start opening in proximity of a pressure ratio value of 2, reach a peak around a value of 3 (10% maximum of the engine air flow) and then start closing till a value of 4 is reached. Once a pressure ratio value of 4 is passed, the bleed valves are closed.

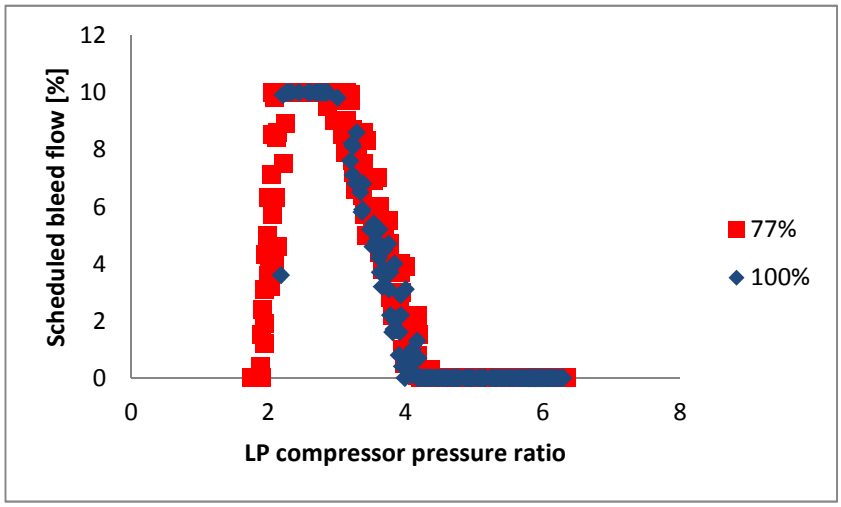

Figure 3.23. Scheduled handling bleed flow downstream of LP compressor.

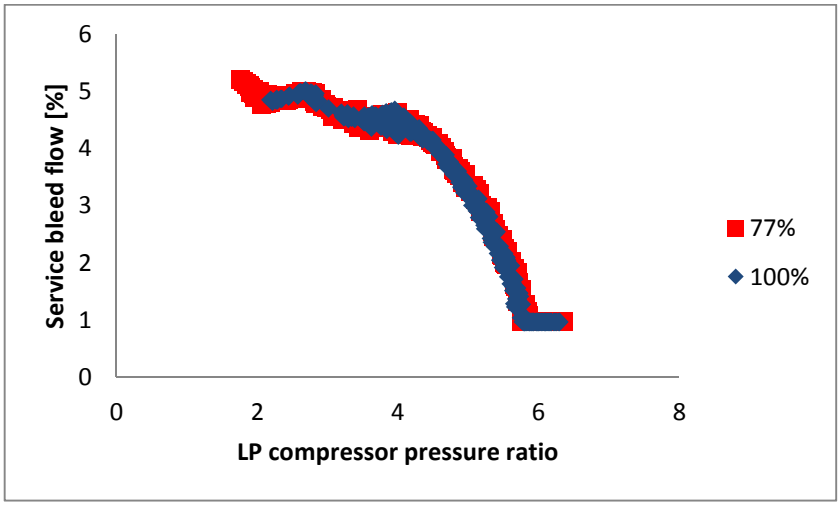

Figure 3.24. Service bleed flow downstream of LP compressor.

This behavior is consistent with aeronautical compressors, for which the stall risk is usually maximum at an intermediate power level between idle and design conditions. Even taking into account air mass flow losses due to scheduled bleeds, there is still a discrepancy of some percentage points in the ED data related to inlet and exhaust flows. The reason for this is not explained in the ED manual, therefore the presence of other bleed valves which deliver hot pressurized air for other services (such as cabin and seals pressurization, oil pumping, actuators, engine bay ventilation, etc.) must be postulated. Such bleed is here referred to as "service bleed flow" (Figure 3.24): when the engine is in idle conditions a consistent percentage of air is extracted (over 5% of the total air mass flow), but when running at full power a fixed quantity of 1% is extracted: with higher engine mass flows, only a smaller part is needed to perform service purposes. For the sake of simplification, in the numerical model of the engine service bleed flow is taken out from the same bleed duct component between the two compressors. Following this assumption, the only component in which a loss of mass flow is modeled, in the engine simulation, is the bleed duct component, where the sum of scheduled handling bleed and service bleed is extracted from the engine.

3.3.4 Turbine maps

From the ED output, the three different turbine maps were not identifiable. For this reason, three generalized maps found in the GSP library were used and scaled to the design point. However, the most difficult effort has been focused on choosing the correct design point efficiencies for the three turbines.

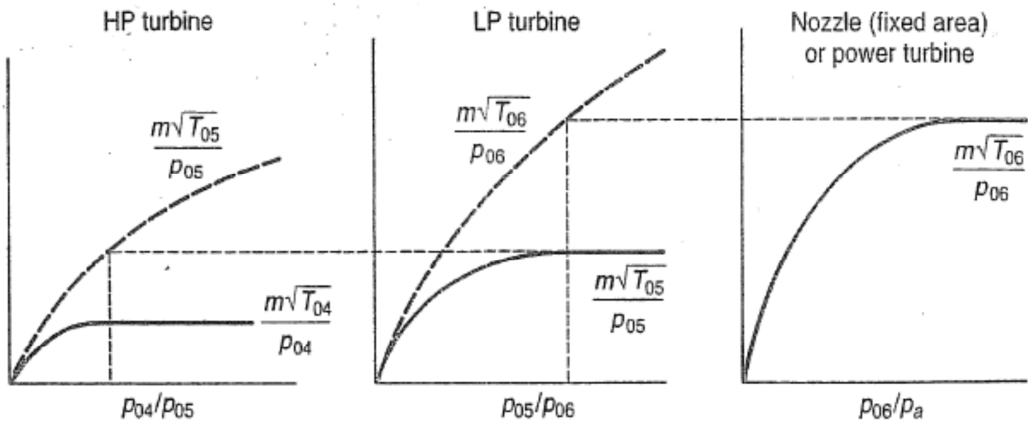

Figure 3.25. Operation of three turbines in series [2].

The calibration of the model was made taking advantage of the fact that, for the majority of the operating conditions, all the three turbines remain choked; hence, as long as the FPT operating point position changes maintaining choking conditions, the other two turbines are constrained to preserve approximately the same operating point. This represents the normal working behavior of turbines in series, an example of which is visible in Figure 3.25. As well explained in [2], the assumption of single line turbine characteristics, in which corrected mass flow is independent of turbine corrected speed, is a close approximation to reality, especially in choking conditions. Within this hypothesis, *"as long as the power turbine is choked, the gas generator turbines will operate at a fixed non-dimensional point"* [2]: in fact continuity requires that the corrected mass flow exiting the preceding turbine must equal that entering the following turbine, as can be observed in Figure 3.25. Based on this principle, the three turbine efficiencies can be determined using a trial and error procedure. This procedure is referred to as "turbine map calibration", which is performed in such a way that TSHAFT results and ED output are compared for different conditions until a combination of the turbine efficiencies showing a minimum acceptable discrepancy is obtained.

3.3.5 Performance Results and comparison with Engine Deck data

Once the engine model is built, predicted performance is checked against the output provided by the ED. The model validation is carried out analyzing five steady state conditions of interest for the ERICA tilt-rotor, which are reported in Table 3.1. These input data employed in both TSHAFT and ED models uniquely determine a single operating point of the engine for each of the five conditions.

	Altitude [m]	Mach Number	FPT Power normalized to DP [%]	Total Bleed Flow [%]
Conversion Mode 1	0	0.144	63.7	5.2157
Conversion Mode 2	0	0.181	64.3	5.2920
Conversion Mode 3	0	0.242	68.6	5.2944
Hover	0	0	98.8	3.6897
Cruise (design point)	7500	0.4975	100	0.9669

Table 3.1. Five testing conditions for the ERICA engine model: input data.

In Figure 3.26-3.27, the five engine operating points are visible on LP and HP compressor maps. The data are normalized with respect to Design Point conditions (DP). A very good compatibility between TSHAFT and ED predictions is observed. Again, as in the preceding models, the errors between the two codes are higher as the distance from the design point is increased. The reason is given by the fact that the point used to calibrate TSHAFT model is represented by the cruise condition; in fact, for this particular condition the error tends to zero, and the operating points predicted by the two codes are nearly coincident.

In Figure 3.28-3.32, a series of comparisons is made between some variables of interest, in particular specific fuel consumption. Related to these charts is Table 3.2, which explicitly reports the values of these variables calculated by TSHAFT and ED along with the error calculation. A high accordance between the two codes is evidenced as the largest part of the discrepancies is around or below 1%. The highest computed error affects the engine exit temperature in hover, a parameter of minor interest, and is equal to 2.2%.

3.4 References

[1] W. P. J. Visser and M. J. Broomhead. GSP, *A Generic Object-Oriented Gas Turbine Simulation Environment*, ASME paper 2000-GT-0002, 2000.

[2] M. G. Ballin, *A high fidelity real-time simulation of a small turboshaft engine*, NASA TM 100991, Ames Research Center, 1988.

[3] H.I.H. Saravanamuttoo, G.F.C. Rogers and H. Cohen, *Gas Turbine Theory*, Pearson Prentice Hall, 2001.

[4] P.P. Walsh and P. Fletcher, *Gas Turbine Performance*, Blackwell Publishing, 2004.

[5] H.I.H. Saravanamuttoo, *Overview on basis and use of performance prediction methods, in "Steady and Transient Performance Prediction of Gas Turbine Engines"*, AGARD Lecture Series 183, 1992.

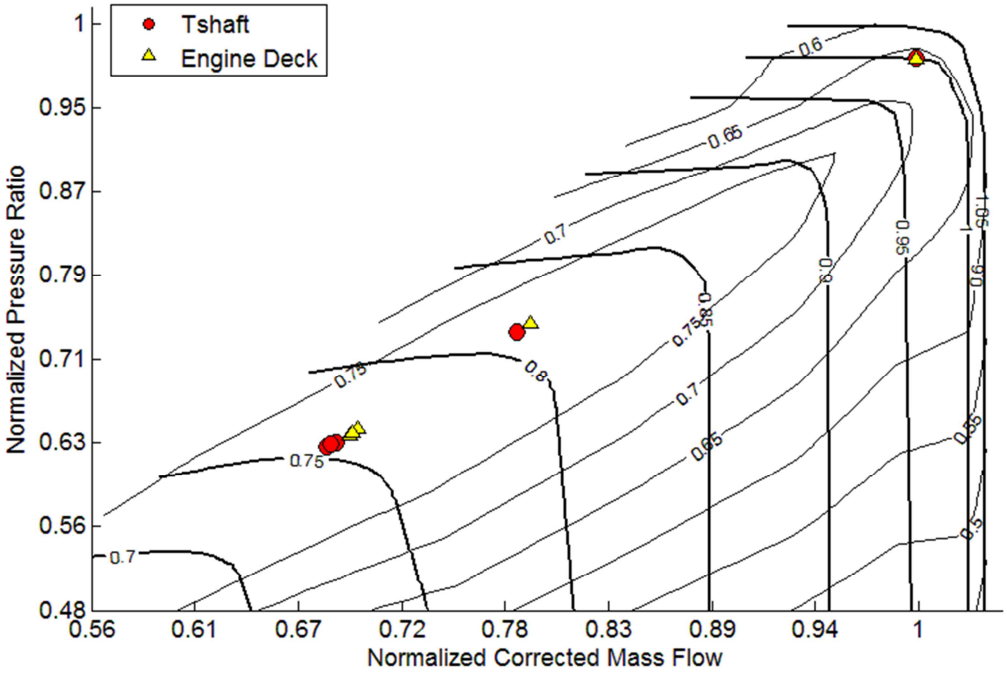

Figure 3.26. Operating points comparison between ED and TSHAFT on LP compressor map (normalized with respect to Design Point).

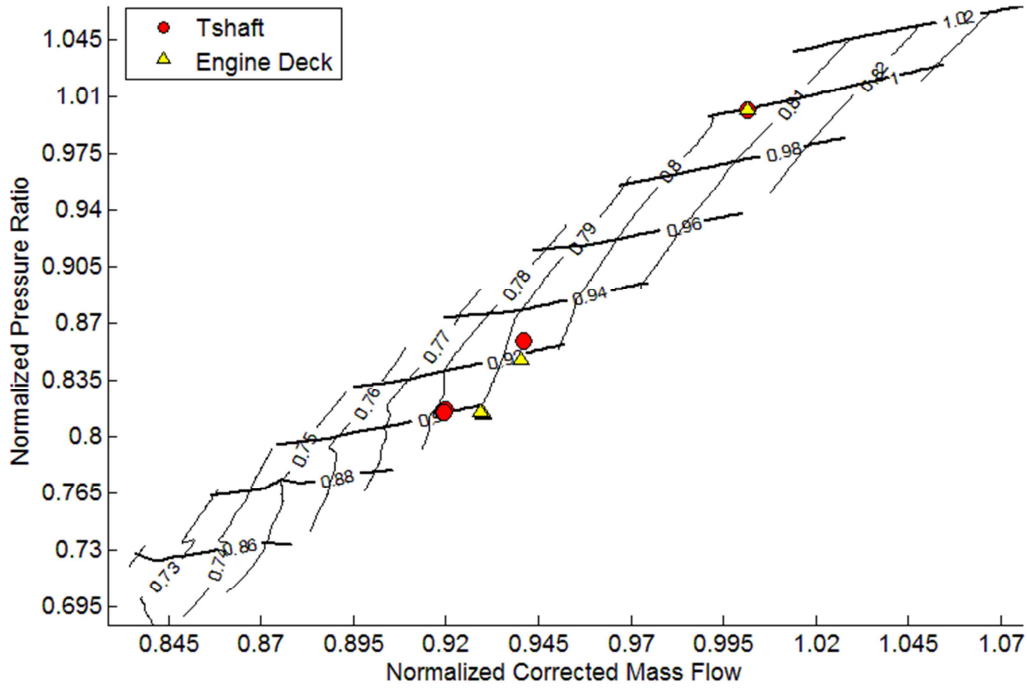

Figure 3.27. Operating points comparison between ED and TSHAFT on HP compressor map (normalized with respect to Design Point).

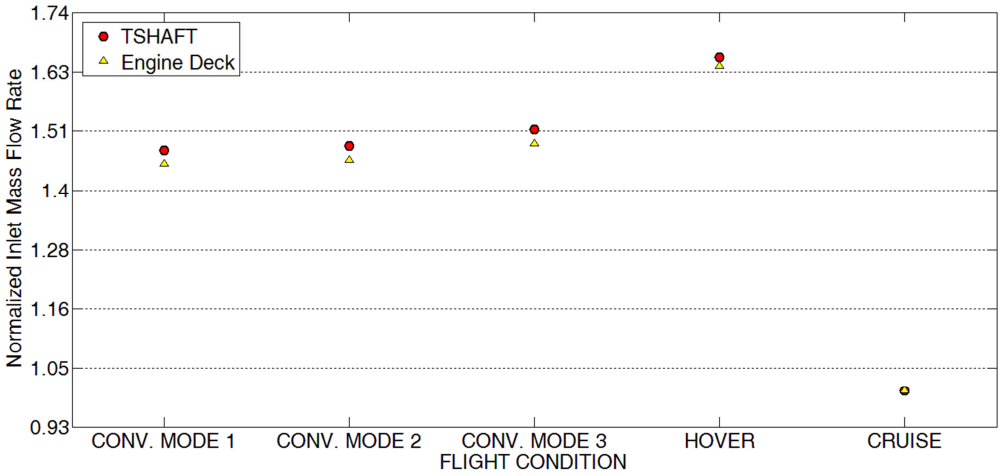

Figure 3.28. Normalized mass flow rate comparison between ED and TSHAFT.

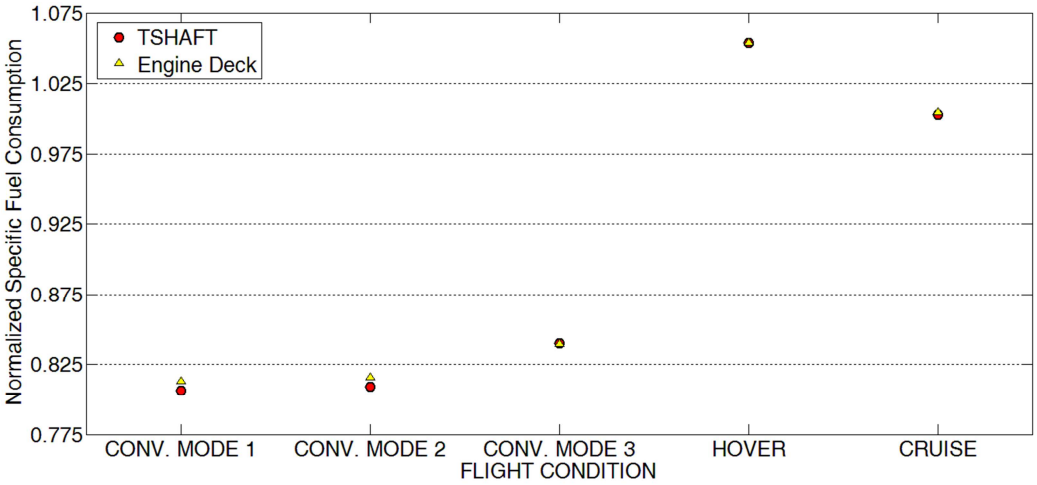

Figure 3.29. Normalized SFC comparison between ED and TSHAFT.

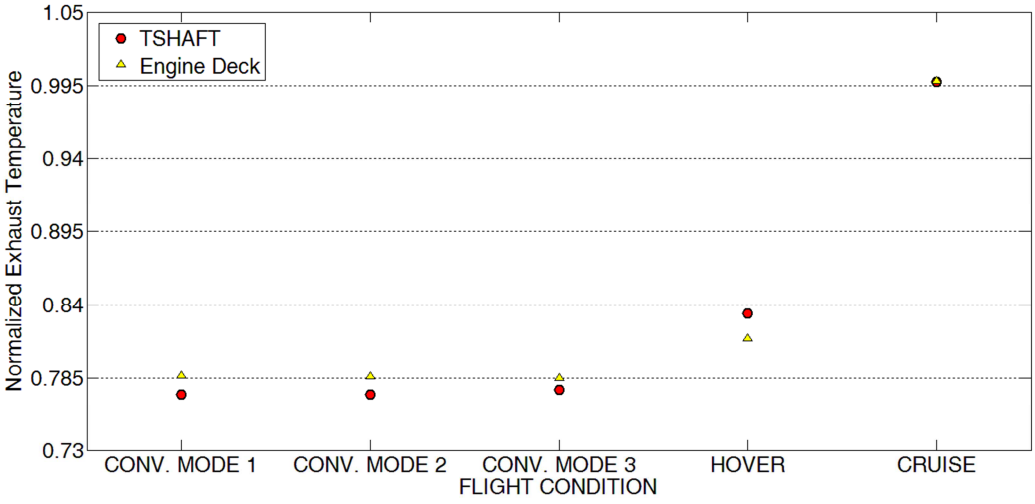

Figure 3.30. Normalized engine exit total temperature comparison between ED and TSHAFT.

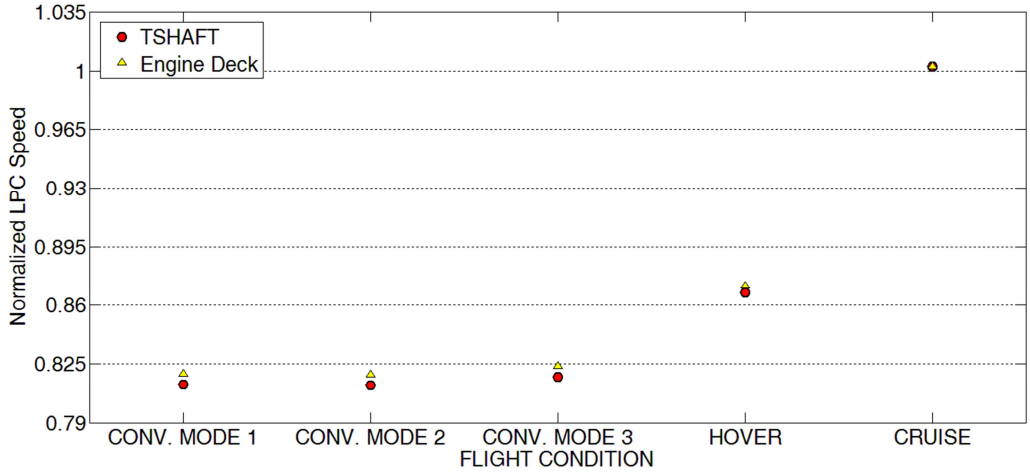

Figure 3.31. Normalized LP compressor speed comparison between ED and TSHAFT.

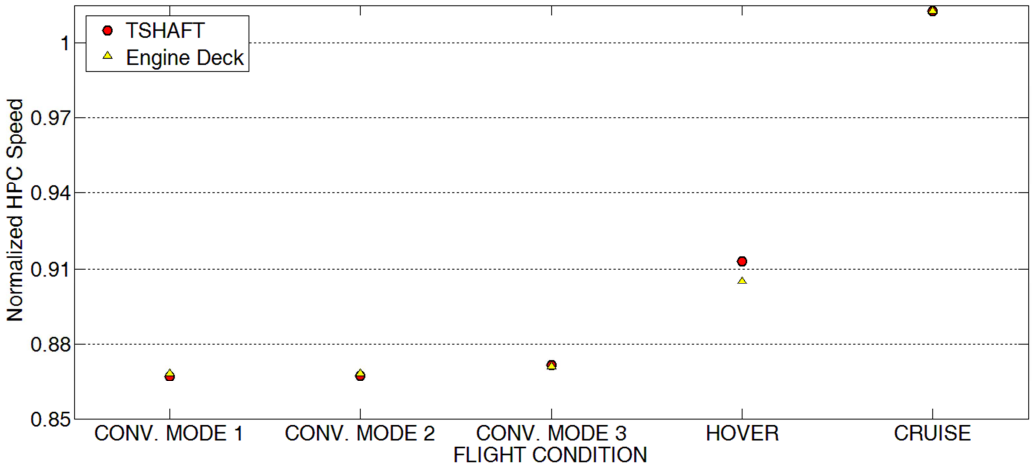

Figure 3.32. Normalized HP compressor speed comparison between ED and TSHAFT.

	Relative Errors [%]				
	m_f	m	T_{exit}	N_{LPC}	N_{HPC}
Conversion Mode 1	0.7759	1.7692	1.6865	0.7385	0.1233
Conversion Mode 2	0.7733	1.8649	1.6464	0.7453	0.1152
Conversion Mode 3	0.0289	1.8259	1.0287	0.7773	0.062
Hover	0.0232	1.0507	2.2245	0.4505	0.8611
Cruise	0.1118	0.0023	0.0273	0.0169	0.0052

Table 3.2. Error analysis for the ERICA engine model: fuel flow (m_f), air mass flow (m), exhaust temperature (T_{exit}), LP compressor speed and HP (N_{LPC}) compressor speed (N_{HPC}).

Chapter 4

TCOPTER: a Helicopter Trim Simulation Code

4.1 Helicopter Model Assumptions

Helicopter flight simulation is a very complicated and interdisciplinary problem, which involves different technical branches, such as aerodynamics, blade dynamics, acoustics, structural and vibrational analysis. Some interesting simulation tools are commercially available, which are able to perform a comprehensive analysis dealing with all these disciplines. Probably the most famous and successful example is given by CAMRAD, a code developed by Johnson [1]; its capabilities include inertia, elasticity and aerodynamics coupling, in order to give the possibility to perform a full aeroelastic analysis, not only taking into account the aerodynamics of the main rotor, but also considering the interaction effects between rotors and fuselage.

The degree of sophistication of a particular model must be chosen wisely, because it has to capture the most significant aspects of a particular physical phenomenon, at the same time minimizing the need for computational resources. The best compromise has to be chosen, which irrevocably leads to neglecting some aspects of the problem. Since the present study is mainly focused on performance prediction, the helicopter simulation code implemented, TCOPTER, was built with the purpose of determining with a good degree of reliability the power consumed by the helicopter rotors (main rotor and tail rotor). This objective can be achieved by concentrating only on the aerodynamic aspect of helicopter simulation, and by making some simplifying assumptions, which will dramatically reduce the model complexity without losing too much accuracy.

We must underline that variable speed operation in practice needs a thorough vibrational analysis to understand how the loads are transferred to the hub and which speeds are capable of exciting the natural frequencies of a big number of structural elements. However, as we stated in the introduction, the purpose of the present thesis is to understand if the performance gain is worth the application of

the VSR concept; after that, vibrational studies must follow and possible innovative solutions to the damping problem may be studied.

The previous discussion led to a definition of the physical assumptions that are supposed to preserve the reliability of the helicopter power estimation and are therefore introduced inside TCOPTER. The assumptions for the main rotor model are the following:

- Combined Momentum theory and Blade Element Theory (BEMT);
- Linear induced velocity model (Glauert);
- Rigid blade motion: no blade elastic deformation;
- Blade lead-lag motion is neglected;
- Real airfoil characteristics: C_l and C_d are calculated as functions of Mach number, Reynolds number and angle of attack;
- Each airfoil section is isolated and does not influence the flow in the other adjacent sections;
- No small angle assumption.

The helicopter trim calculations are instead based on the following hypotheses:

- Steady state level flight operation: zero climb/descent rate;
- Azimuthal averaged forces and moments are balanced;
- Fuselage drag is obtained using empirical relations;
- No small angle assumption for the Euler angles in attitude calculation.

We will see in section 5.3 that these assumptions lead to an acceptable accuracy in performance prediction, especially main rotor power. Unlike for the engine performance code, there will be no chapter uniquely dedicated to the validation of TCOPTER. In fact, the code was validated against experimental data only once, for the specific real case treated in Chapter 5. It has been used also for preliminary design studies, but it still has not been tested on a vast number of numerical and experimental cases.

4.2 Main Rotor Model

The main rotor model employed in TCOPTER combines momentum theory and blade element theory (BEMT) at an advanced level. This is a very known basic theory of helicopter flight which is capable of capturing the most important aspects of helicopter rotor behavior. It can be found in most of the textbooks dealing with helicopter flight, of which Refs. [2],[3],[4],[5] represent authoritative examples. In the implementation of the current model, the practical guidelines followed are those provided by Howlett [6] and Steiner [7].

Let us first analyze a single blade, which is visible from the upper side view of an helicopter in forward flight (Figure 4.1). The blade is divided into infinitesimal segments of mass *dm* and length *dr* in the radial direction. Note the convention adopted for the azimuthal angle:

$$\psi = \Omega t \tag{3.1}$$

With respect to the orientation of the rotorcraft, ψ is zero when it is aligned with the direction of the air speed *V* seen by an observer on the helicopter (positive *x* when radius is pointing outwards).

4.2.1 Dimensionless Coefficients

Quite often rotor analysis is carried out using dimensionless quantities; let us define the ones which will be employed in the following treatment. The forward speed is linked to the first dimensionless parameter μ, the rotor advance ratio:

$$\mu = \frac{V\cos\alpha_{MR}}{\Omega R} \tag{3.2}$$

which is defined as the component of the forward speed parallel to the rotor disk, normalized by the rotor tip speed. Another interesting parameter is the rotor inflow ratio, i.e. the ratio between the flow velocity component normal to the rotor disk and the tip speed:

$$\lambda_i = \frac{V_i + V\sin\alpha_{MR}}{\Omega R} \tag{3.3}$$

Clearly, the numerator is given by the sum of the flow velocity induced by the rotor in order to produce lift, and the component of the advancing speed normal to the rotor disk. Forces have also their related dimensionless coefficients; the most useful, which will be often used in the present analysis, is the thrust coefficient:

$$C_T = \frac{T}{\rho A(\Omega R)^2} \tag{3.4}$$

Any force calculated can be normalized with the denominator in eq. (3.3). We can also define in a similar way the power coefficient, which we will see as the most interesting parameter in the model validation in section 5.3:

$$C_P = \frac{P}{\rho A(\Omega R)^3} \tag{3.5}$$

Along with kinematic, dynamic and energy parameters, the typical lengths are also normalized with respect to the tip radius *R*. In fact, as you can see in Figure 4.1Figure 4.2, the hinge offset *e* (in meters) is normalized by *R*:

$$\xi = \frac{e}{R} \tag{3.6}$$

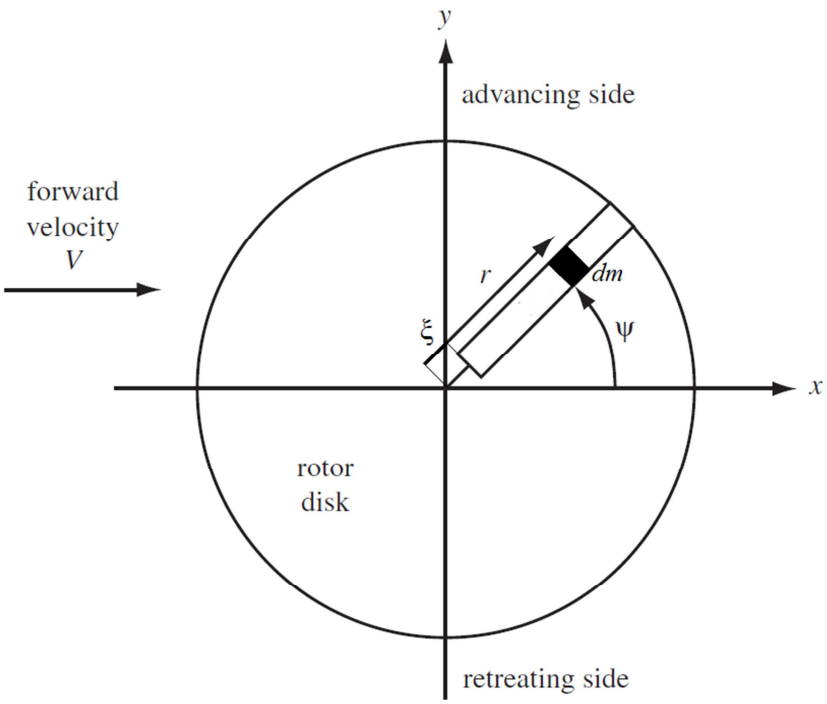

Figure 4.1. Hub reference axes and azimuth angle definition (adapted from Johnson [3]).

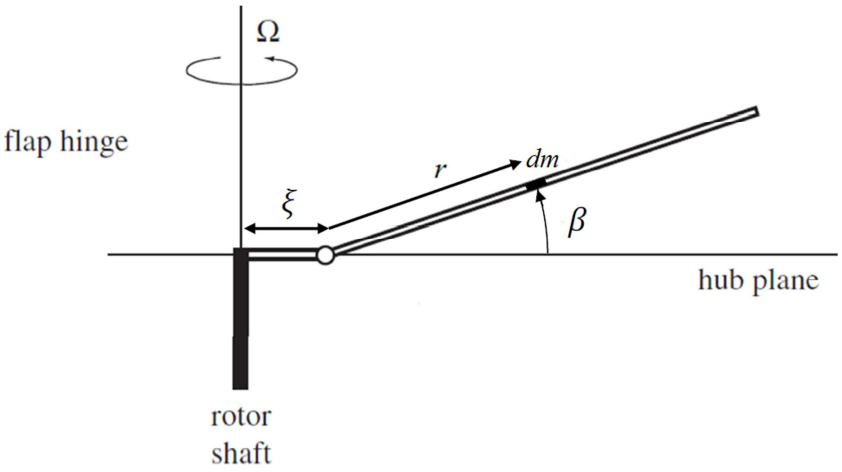

Figure 4.2. Blade flapping motion and hinge configuration (adapted from Johnson [3]).

In the same figures, the variable r is defined as the dimensionless radial position on the blade, starting from the blade hinge. Figure 4.2 represents a lateral view of the blade, showing the blade flapping motion around the articulated hinge and the definition of the flapping angle β.

4.2.2 Blade Section Velocities

Our analysis should start with the determination of the expressions for the velocities seen by a particular blade section. In fact, at each different radial position a different relative speed is seen by the blade, due to its rotational and flapping motion. Their knowledge allows to determine the aerodynamic forces related to each infinitesimal segment; the loads will be first integrated over the rotor blade and then integrated and averaged along the azimuthal angle ψ in order to calculate the forces and moments on the rotor.

Referring to Figure 4.3, the normalized velocities at a particular section of the blade are calculated with no small angle assumption; note that no blade lead-lag motion is simulated by using these equations:

$$\frac{V_T}{\Omega R} = \xi + r\cos\beta + \mu\sin\psi \tag{3.7}$$

$$\frac{V_P}{\Omega R} = \lambda\cos\beta + r\dot{\beta} + \mu\sin\beta\cos\psi \tag{3.8}$$

$$\frac{V_R}{\Omega R} = \mu\cos\beta\cos\psi - \lambda\sin\beta \tag{3.9}$$

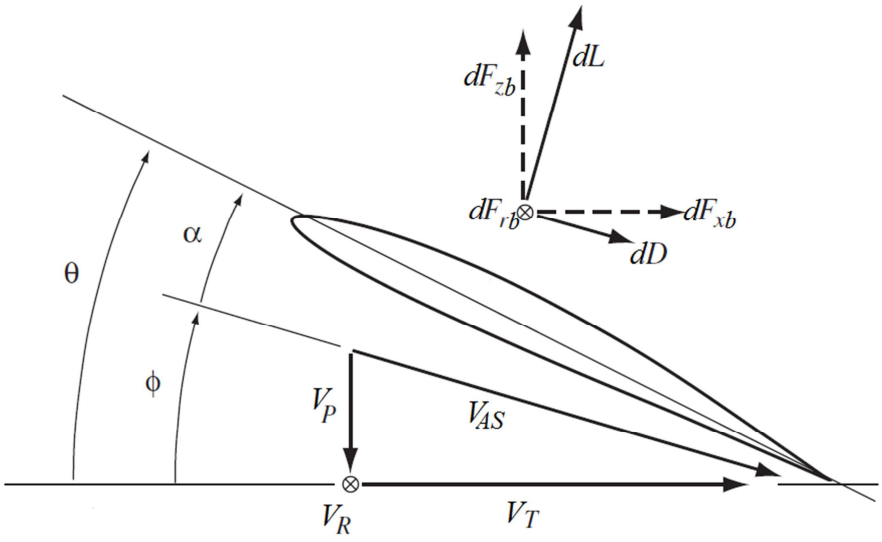

Figure 4.3. Blade section velocities and forces (adapted from Johnson [3]).

4.2.3 Induced Inflow Model

While for the hover condition an analytical solution to the induced velocity profile can be found using BEMT, this is no longer true for forward flight cases. In order to preserve the simplicity of the analysis, a prescribed induced inflow model is used. There are many in literature; a linear inflow model proposed by Glauert [2], derived by means of experimental observations, is chosen. The induced inflow varies along the rotor disk and is calculated as follows:

$$\lambda_i = \lambda_{i0}\left(1+\left(\xi + r\cos\beta\right)K_x\cos\psi\right) \tag{3.10}$$

where λ_{i0} is the average inflow coefficient calculated assuming uniform inflow:

$$\lambda_{i0} = \frac{C_T}{2\sqrt{\mu^2+\left(\lambda_{i0}+\mu\tan\alpha_{MR}\right)^2}} \tag{3.11}$$

and the local inflow coefficient, which accounts for both induced velocity and the forward speed component normal to the rotor, is the usual:

$$\lambda = \mu\tan\alpha_{MR} + \lambda_i \tag{3.12}$$

The constant K_x is determined using Glauert empirical relations:

$$K_x = \frac{15\pi}{23}\tan\left(\frac{\chi}{2}\right) \tag{3.13}$$

$$\chi = \arctan\left(\mu/\lambda_i\right) \tag{3.14}$$

The determination of the exact value of λ is clearly an iterative process, since the abovementioned equations are strictly coupled.

4.2.4 Blade Section Lift and Drag

For each blade section, lift and drag are calculated using two-dimensional thin airfoil theory, employing the introduction of nonlinear lift and drag coefficients. It is therefore assumed that only the tangential and perpendicular components of the velocity relative to the blade contribute to lift and drag determination, so that the velocity seen by the airfoil section becomes:

$$V_{AS} = \sqrt{V_T^2 + V_P^2} \tag{3.15}$$

The radial velocity V_R is, however, taken into account in the overall forces balance, as we will see later. The infinitesimal lift and drag forces acting on a segment of length *Rdr* can be computed as follows (note that these are not dimensionless quantities):

$$dL = \frac{1}{2}\rho c C_l V_{AS}^2 R dr \tag{3.16}$$

$$dD = \frac{1}{2}\rho c C_d V_{AS}^2 R dr \tag{3.17}$$

The problem remains on how to compute C_l and C_d. The importance of correctly simulating airfoil characteristics was already stated in the introduction; in order to obtain a good power estimate, it is necessary to predict airfoil behavior in two limit conditions: near stall, and at high Mach numbers. Both viscous effects and compressibility effects are strong contributors to the increase in main rotor power, especially at high helicopter advancing speeds. In fact, at high forward speeds *V*, the advancing blade sees very high Mach numbers, which can eventually overcome the drag divergence Mach number, with the flow becoming transonic. On the retreating blade, instead, the flow is so slow that it can eventually stall; note that in the inward part of the blade, at any value of *V* different from zero, a reversed flow region will always be present. As *V* is increased, this zone becomes bigger, and an increasing number of sections of the blade are affected by stall.

Compressibility and stall both result in an increase in rotor drag and therefore absorbed power. The use of incompressible linear theory for airfoils will not be sufficient to simulate these phenomena, since it does not capture the most important contributions to main rotor power. For this reason, experimental look-up tables are used in order to incorporate empirical data inside the model, examples of which are Figure 4.4Figure 4.5. The lift and drag coefficients are calculated as functions of angle of attack, Mach number and Reynolds number:

$$C_l = f(\alpha, Ma, Re) \tag{3.18}$$

$$C_d = f(\alpha, Ma, Re) \tag{3.19}$$

It is noteworthy that such airfoil characteristic tables are derived from measurements in steady state conditions; they are able to approximately predict the occurrence of a static stall. When operating with feathering motion (the periodic pitching movement of a blade imposed by pitch control) another type of

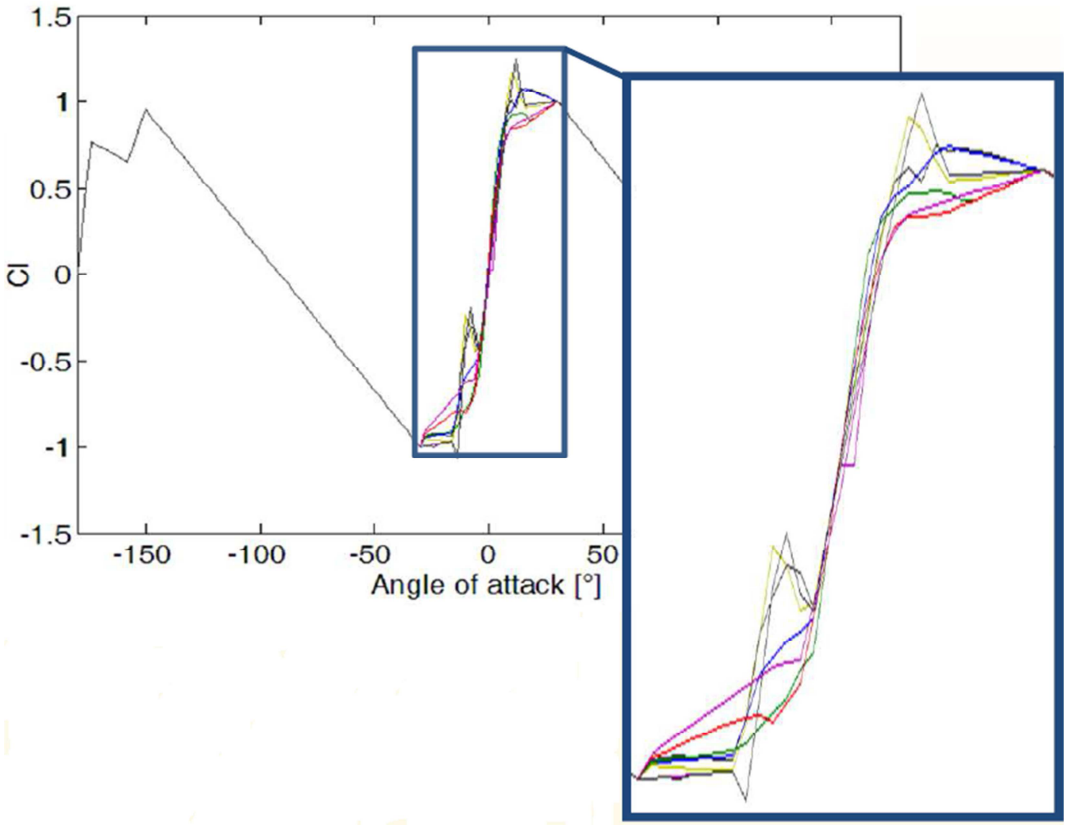

Figure 4.4. Lift coefficient as a function of angle of attack and Mach number (data from [7]).

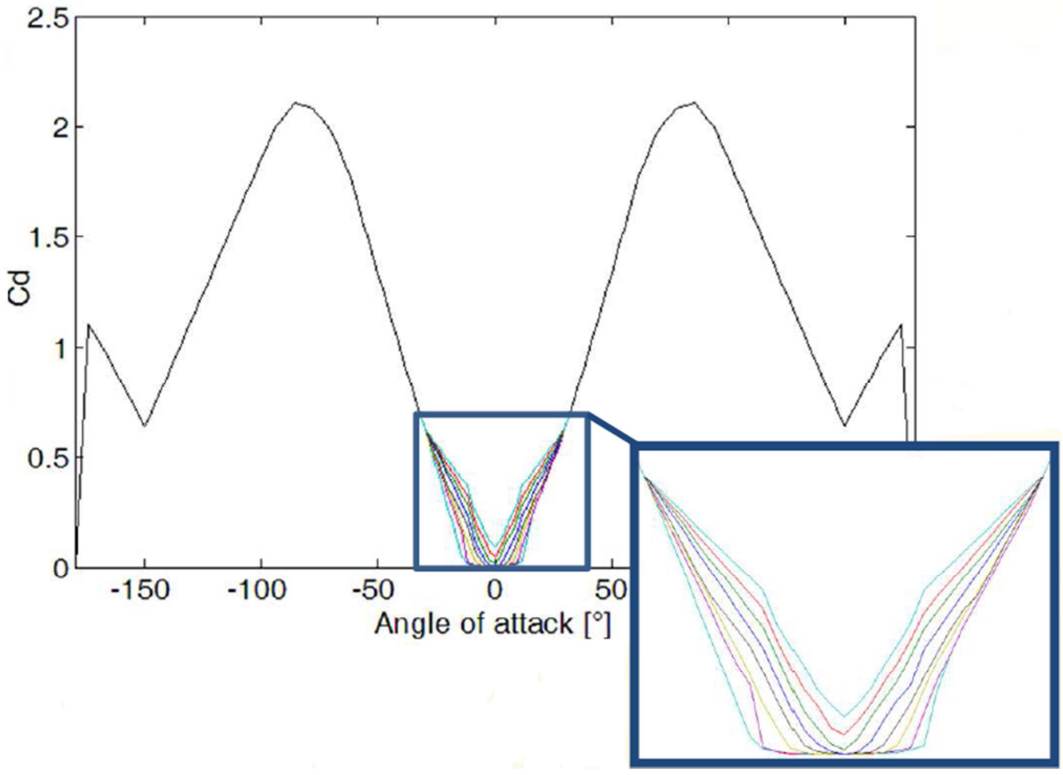

Figure 4.5. Drag coefficient as a function of angle of attack and Mach number (data from [7]).

stall, dynamic stall, is set. This stall typology is different from the previous one, especially because it is characterized by a higher maximum C_l value and a sort of hysteresis, so that the C_l curve during an α increase is no longer the same curve when α is decreased after stall. However, the utilization of static stall information, even if not extremely accurate, is a conservative stall estimate, since dynamic stall is usually encountered at higher angles of attack with respect to static stall. In practice, if the rotor model anticipates the onset of stall, limiting the operational possibilities of the helicopter, it can be viewed as a designer constraint chosen to maintain a safe stall margin. Just before the static stall occurs, the error in using static airfoil characteristics is still small and acceptable, so static airfoil data interpolation is a valid compromise between model complexity and reliability.

Another source of error related to airfoil data is given by the unavailability of complete experimental information along the entire [0°,360°] α interval. In fact, as can be seen in Figure 4.4Figure 4.5, Mach number sweeps are reported for only a limited range of α (typically [-20°,+20°]); the main reasons for this lack of data are related to a minimization of time and cost of unnecessary experimental measurements. Indeed, extreme values of α are only encountered in a very limited zone in the rotor disk, near and inside the reverse flow region; since this part is only a small fraction of the rotor disk, the error made has a limited effect on overall rotor performance. Therefore, in our model, for the α domain outside [-20°,+20°], the influence of *Re* and *Ma* is neglected.

To obtain the values of lift and drag coefficients from the airfoil data tables three parameters are necessary: *Ma*, *Re* and α. The first two are straightforward:

$$Ma = \frac{V_{AS}}{\sqrt{kRT_{amb}}} \tag{3.20}$$

$$Re = \frac{V_{AS}c}{\upsilon} \tag{3.21}$$

with υ representing the air kinematic viscosity. The determination of the angle of attack, instead, is quite long and complex and requires iteration. From Figure 4.3, it can be easily shown that:

$$\alpha = \vartheta - \varphi \tag{3.22}$$

where ϑ is the blade pitch angle and φ is the inflow angle. The first is given by the sum of the pitch given as a control input to the blade and the inherent blade twist:

$$\vartheta = \vartheta_{control} + \vartheta_{twist} \tag{3.23}$$

The blade control pitch angle can be approximated to the first harmonic terms of a Fourier series, dependent on the azimuth angle:

$$\vartheta_{control} = \vartheta_0 + \vartheta_{1c} cos\psi + \vartheta_{1s} sin\psi \tag{3.24}$$

The local inflow angle, instead, requires knowledge of the velocities at the airfoil section, computed as in eqs. (3.7-8); it is calculated with the four-quadrant inverse tangent function, to account for reverse flow:

$$\varphi = arctan\left(V_P / V_T\right) \tag{3.25}$$

Grace to the inverse tangent with two arguments, when projecting from wind axes to blade axes, the lift and drag forces are computed as negative values if reverse flow occurs.

4.2.5 Forces and Moments Acting on the Rotor Hub

In the previous section, we found a way to calculate the values of lift and drag of an infinitesimal segment of the blade. These infinitesimal forces have been computed in the wind reference axes, as illustrated in Figure 4.3. Now, the objective of this section is to calculate the total forces and moments to which the main rotor is subject. To do this, we have to change reference frame and integrate the contributions given by each single segment.

Let us first transform the forces computed in wind axes to the blade reference axes (Figure 4.3):

$$dF_{zb} = \left(\frac{dL}{dr} cos\varphi - \frac{dD}{dr} sin\varphi \right) dr \tag{3.26}$$

$$dF_{xb} = \left(\frac{dD}{dr} cos\varphi + \frac{dL}{dr} sin\varphi \right) dr \tag{3.27}$$

$$dF_{rb} = -\frac{dD}{dr} tan\Lambda \, dr \tag{3.28}$$

Note that in this reference the radial force F_{rb} can be calculated using the equivalence assumption for swept wings, as suggested by Johnson [4]; F_{rb} has the

negative sign because it is directed inward along the radial direction. The yawed flow angle Λ is then defined using blade section speeds as follows:

$$\Lambda = arctan\left(V_R / V_T\right) \tag{3.29}$$

From the reference system attached to the blade we should pass to the shaft reference axes, in which the x_s and y_s are in the rotor disk plane and the z_s axis is parallel to the rotational speed vector Ω:

$$dF_{zs} = dF_{zb}cos\beta + dF_{rb}sin\beta \tag{3.30}$$

$$dF_{xs} = dF_{xb} \tag{3.31}$$

$$dF_{rs} = dF_{rb}cos\beta - dF_{zb}sin\beta \tag{3.32}$$

The last transformation is made from the moving reference frame attached to the rotating shaft to a reference system again centered in the rotor center of rotation, but this time fixed with respect to the helicopter fuselage. Finally, if we integrate the different contributions of the rotor segments from the hinge to the tip, we are able to obtain the forces and moments acting on the main rotor, which are then transferred to the helicopter fuselage:

$$F_z = \int_{\xi}^{1} F_{zs}\,dr \tag{3.29}$$

$$F_x\left(\psi\right) = \int_{\xi}^{1} F_{xs}sin\psi + F_{rs}cos\psi\,dr \tag{3.30}$$

$$F_y\left(\psi\right) = \int_{\xi}^{1} -F_{xs}cos\psi + F_{rs}sin\psi\,dr \tag{3.31}$$

$$M_z = \int_{\xi}^{1} F_{xs}\left(\xi + rcos\beta\right)R\,dr \tag{3.32}$$

$$M_x\left(\psi\right) = \int_{\xi}^{1} \left[F_{zs}\left(\xi + rcos\beta\right) - F_{rs}rsin\beta\right]Rsin\psi\,dr \tag{3.33}$$

$$M_y\left(\psi\right) = \int_{\xi}^{1} -\left[F_{zs}\left(\xi + rcos\beta\right) - F_{rs}rsin\beta\right]Rcos\psi\,dr \tag{3.34}$$

It is shown that the vertical force F_z and moment M_z are independent from the blade azimuthal position ψ, whereas the remaining forces and moments are strictly dependent on ψ. The forces and moments are therefore not steady, but periodic; in order to calculate helicopter trim -which is a quasi-steady state equilibrium condition of the helicopter where all the forces acting on the rotorcraft are balanced (no accelerations)- we need to calculate an average value of all the six forces and moments in one revolution, multiplied by the number of blades:

$$T_{MR} = \frac{N_b}{2\pi} \int_0^{2\pi} F_z d\psi \tag{3.35}$$

$$H_{MR} = \frac{N_b}{2\pi} \int_0^{2\pi} F_x(\psi) d\psi \tag{3.36}$$

$$Y_{MR} = \frac{N_b}{2\pi} \int_0^{2\pi} F_y(\psi) d\psi \tag{3.37}$$

$$M_{zMR} = \frac{N_b}{2\pi} \int_0^{2\pi} M_z d\psi \tag{3.38}$$

$$M_{xMR} = \frac{N_b}{2\pi} \int_0^{2\pi} M_x(\psi) d\psi \tag{3.39}$$

$$M_{yMR} = \frac{N_b}{2\pi} \int_0^{2\pi} M_y(\psi) d\psi \tag{3.40}$$

The moments are taken with the same sign convention visible in the Figure 4.6Figure 4.7, representing helicopter equilibrium. Once the forces expressed in blade axes are projected in the hub-shaft axes, it becomes possible to sum the contribution of every single sector to the forces H_{MR},Y_{MR},T_{MR}, and the moments M_{xMR},M_{yMR},M_{zMR} acting on the rotor hub.

4.2.6 Flapping Motion

There is still something missing from the current main rotor analysis. We introduced the flapping angle, but we have not seen yet how it can be calculated. If we analyze the flapping motion dynamics, introducing the aerodynamic, inertial and centrifugal forces, we obtain the following differential equation:

$$\ddot{\beta} + \nu_\beta^2 \beta = \frac{M_\beta}{\Omega I_\beta} \tag{3.41}$$

Note that the blade weight force has been neglected in this formulation, a quite common assumption in rotor analysis. The flapping moment is the result of the integration of the vertical force in the blade axes:

$$M_\beta = \int_\xi^1 \frac{dF_{zb}}{dr} Rdr \tag{3.42}$$

The term ν_β in eq. (3.41) is the dimensionless flap frequency, which appears due to the presence of a hinge offset from main rotor center of rotation. It can be computed as follows [5]:

$$\nu_\beta^2 = 1 + \frac{3\xi}{2(1-\xi)} \tag{3.43}$$

An analytical solution to eq. (3.41) exists only when employing the small angle assumption and analytical expressions for C_l (linear) and C_d (quadratic). Unfortunately, without these assumptions, the differential equation (3.41) is highly nonlinear due to the M_β term; a solution can be found only by using numerical methods. Instead of employing time-variant approaches such as Runge-Kutta methods, a greatly simplified solution to eq. (3.41) can be found by approximating the flapping angle β as the first harmonic terms of a Fourier series:

$$\beta = \beta_0 + \beta_{1c} cos\psi + \beta_{1s} sin\psi \tag{3.44}$$

The usual operators employed in the calculation of the coefficients of a Fourier series can be applied to the left hand side of eq. (3.41) to obtain:

$$\frac{1}{2\pi} \int_0^{2\pi} \left(\ddot{\beta} + \nu_\beta^2 \beta \right) d\psi = \nu_\beta^2 \beta_0 \tag{3.45}$$

$$\frac{1}{\pi} \int_0^{2\pi} \left(\ddot{\beta} + \nu_\beta^2 \beta \right) cos\psi d\psi = \left(\nu_\beta^2 - 1 \right) \beta_{1c} \tag{3.46}$$

$$\frac{1}{\pi} \int_0^{2\pi} \left(\ddot{\beta} + \nu_\beta^2 \beta \right) sin\psi d\psi = \left(\nu_\beta^2 - 1 \right) \beta_{1s} \tag{3.47}$$

By applying the same operators to the right hand side of eq. (3.41) and rearranging, we are able to transform a single differential equation in a system of three algebraic equations, where the unknowns are the Fourier coefficients β_0, β_{1c}, β_{1s}:

$$\nu_\beta^2 \beta_0 - \frac{1}{2\pi}\int_0^{2\pi} \frac{M_\beta}{\Omega I_\beta} d\psi = 0 \tag{3.48}$$

$$(\nu_\beta^2 - 1)\beta_{1c} - \frac{1}{\pi}\int_0^{2\pi} \frac{M_\beta}{\Omega I_\beta} cos\psi d\psi = 0 \tag{3.49}$$

$$(\nu_\beta^2 - 1)\beta_{1s} - \frac{1}{\pi}\int_0^{2\pi} \frac{M_\beta}{\Omega I_\beta} sin\psi d\psi = 0 \tag{3.50}$$

This nonlinear set of equations will be part of a greater nonlinear system that has to be generated to calculate helicopter trim conditions.

4.3 Forces and Moments Acting on the Helicopter

Aside from the forces and moments acting on the main rotor, there are some other which are needed to calculate the attitude in the three-dimensional space of the helicopter. These include the helicopter weight, tail rotor thrust, fuselage aerodynamic drag and perturbations. Here below are reported the six equations used to calculate the helicopter equilibrium, slightly modified from those presented in [5] to account for tail rotor cant angle and structural shaft pitch. The moments are calculated referred to the rotor hub.

Longitudinal equilibrium:

$$\begin{aligned} &D_{fus} cos\theta_{FP} + H_{MR} cos(\Theta + \theta_S) - \\ &(T_{MR} + T_{TR} sin\delta) sin(\Theta + \theta_S) cos\Phi = 0 \end{aligned} \tag{3.51}$$

Lateral equilibrium:

$$Y_{MR} + T_{TR} cos\delta cos\Phi + (T_{MR} + T_{TR} sin\delta) cos(\Theta + \theta_S) sin\Phi = 0 \tag{3.52}$$

Vertical equilibrium:

$$\begin{aligned} &W - (T_{MR} + T_{TR} sin\delta) cos(\Theta + \theta_S) cos\Phi - D_{fus} sin\theta_{FP} - \\ &H_{MR} sin(\Theta + \theta_S) + (Y_{MR} + T_{TR} cos\delta) sin\Phi = 0 \end{aligned} \tag{3.53}$$

Rolling moment equilibrium:

$$M_{xMR} + M_{x_{fus}} + T_{TR}cos\delta h_{TR} + W\left(z_{CG}sin\Phi - y_{CG}cos\Phi\right) = 0 \qquad (3.54)$$

Pitching moment equilibrium:

$$\begin{aligned} &M_{yMR} + M_{y_{fus}} + T_{TR}sin\delta l_{TR} - W\left[x_{CG}cos\left(\Theta+\theta_S\right) - z_{CG}sin\left(\Theta+\theta_S\right)\right] - \\ &D_{fus}cos\left(\Theta+\theta_S\right)\left[z_{CG}cos\left(\Theta+\theta_S\right) - x_{CG}sin\left(\Theta+\theta_S\right)\right] = 0 \end{aligned} \qquad (3.55)$$

Torque equilibrium:

$$M_{zMR} - T_{TR}cos\delta l_{TR} = 0 \qquad (3.56)$$

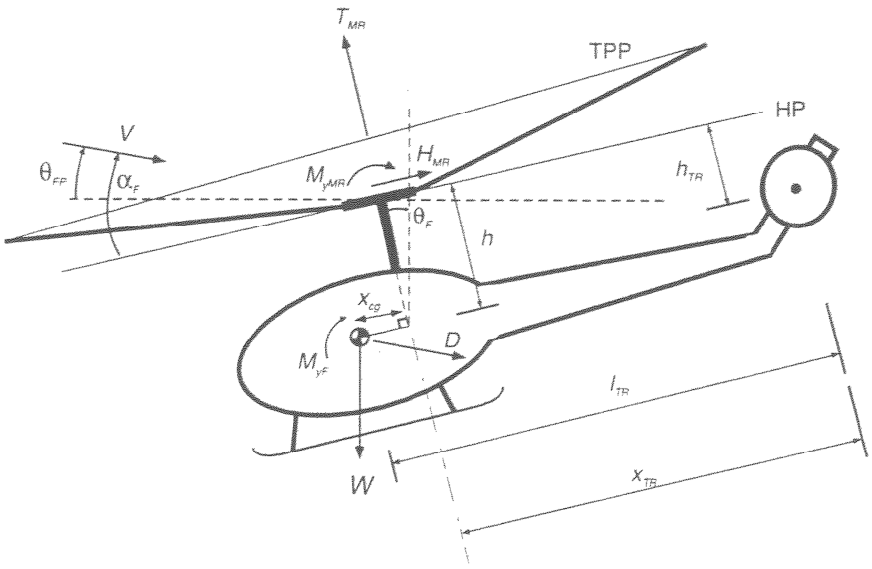

Figure 4.6 Longitudinal forces and moments acting on a helicopter (from Leishman [5]).

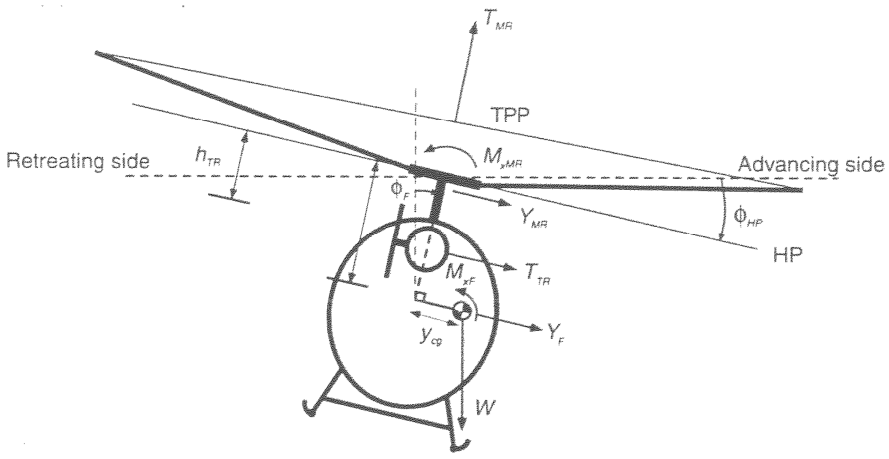

Figure 4.7 Lateral forces and moments acting on a helicopter (from Leishman [5]).

Figure 4.6-Figure 4.7 allow for a better understanding of the equilibrium relations (3.50-3.55). Most of the variables in the equations are illustrated in the figures, but let us stop for a while on the most important angles. Since we are dealing only with steady state level flight, the flight path angle ϑ_{FP} is zero. The orientation of the helicopter in space is determined by the three Euler angles: roll Φ, pitch Θ and yaw (or sideslip); the last is not visible in figures. In fact, in the present trim analysis, the sideslip angle is neglected and is considered null, so that the helicopter advancing motion is considered unyawed.

A final consideration on tail rotor thrust and power is needed: these are calculated in a similar way to the main rotor ones, introducing additional simplifying assumptions: the flapping motion is neglected, the inflow is considered uniform and analytical airfoil characteristics are used.

4.4 Trim Solution

To trim the helicopter at a particular forward speed V and main rotor speed Ω, the collective, cyclic and lateral pitch controls must be adjusted to find the equilibrium. The relationships written in the previous section are highly non-linear and interdependent, and also include the evaluation of numeric integrals; in fact, when using look-up tables an analytical evaluation of the integrals is no more possible. The blade must be divided in a discrete number of segments, and the azimuthal averaged values must be calculated on a finite number of equal spaced positions.

It is not possible to uncouple the main rotor equations from the helicopter equilibrium equations, because the orientation of the helicopter with respect to the incoming flow influences the aerodynamic forces acting on the rotor; the same happens also inside the main rotor equations, where the inflow, flapping motion, lift and drag equations are highly interconnected to each other. For this reason, they are all implemented as a non-linear system of the type $\boldsymbol{f(x) = 0}$, where $\boldsymbol{f}$ is a vector-valued error function (matching constraints) and $\boldsymbol{x}$ is the vector of the variables (matching guesses). The way this system is written and solved is very similar to the one exposed in Chapter 2 for turboshaft engine matching calculations. In the present helicopter model the number of equations to be solved are twelve. The vector of the variables in this case becomes:

$$x = \left[\vartheta_0, \vartheta_{1c}, \vartheta_{1s}, \beta_0, \beta_{1c}, \beta_{1s}, \Theta, \Phi, \lambda_0, \lambda_{TR}, C_T, C_{TTR}\right] \qquad (3.57)$$

The equations that compose the system ***f(x)*** are: eqs. (3.50-3.55) for helicopter equilibrium, eqs. (3.48-3.50) for flapping motion, the inflow eq. (3.11) for both main rotor and tail rotor, and finally the equivalence between the guessed coefficient of thrust and the thrust force T calculated by numerical integration:

$$C_T - \frac{T}{\rho A(\Omega R)^2} = 0 \tag{3.58}$$

The system is solved numerically with a Levenberg-Marquardt algorithm. Care must be taken in choosing the initial values for the x vector in eq. (3.57), because a choice too far from the solution may lead to converge problems.

4.5 References

[1] W. Johnson, *A Comprehensive Analytical Model of Rotorcraft Aerodynamics and Dynamics, Part 1: Analysis Development*, NASA TM 81182, 1980.

[2] A. Gessow, G. C. Myers, *Aerodynamics of the helicopter*, Frederick Ungar Publishing Co., New York, 1985 (8th Edition).

[3] W. Johnson, *Helicopter Theory*, Dover Publications Inc., New York, 1980.

[4] W. Johnson, *Rotorcraft Aeromechanics*, Cambridge University Press, New York, 2013.

[5] J. G. Leishman, *Principles of Helicopter Aerodynamics*, Cambridge University Press, New York, 2006.

[6] J. J. Howlett, *UH-60A Black Hawk Engineering Simulation Program: Volume I-II*, NASA Contractor Report 166309-166310, December 1988.

[7] J. H. Steiner, *An Investigation of Performance Benefits and Trim Requirements of a Variable Speed Helicopter Rotor*, M.Sc. Thesis, The Pennsylvania State University, 2008 (also available online at http://www.engr.psu.edu/rcoe/theses/Steiner_Jason.pdf, last consultation Jan. 2015).

Chapter 5

VSR Speed Optimization: a Case Study

5.1 Overview of the UH-60 Black Hawk Helicopter

The importance of a real case study relies in the possibility to estimate the performance benefits related to employing a VSR. The helicopter chosen for the present analysis is a UH-60 Black Hawk helicopter (Figure 5.1): it is a four-bladed, medium lift utility helicopter, having a maximum allowable gross weight of 22,000 lbs (9,979 kg). Manufactured by Sikorsky Aircraft Company, the Black Hawk is equipped with two General Electric T700 turboshaft engines. It is a very versatile helicopter, whose missions include: air assault, general support, aeromedical evacuation, command and control and special support operations. It has been chosen as a test case mainly for the presence of a lot of experimental tests and information available to the public, which permit the construction and validation of a sound helicopter model.

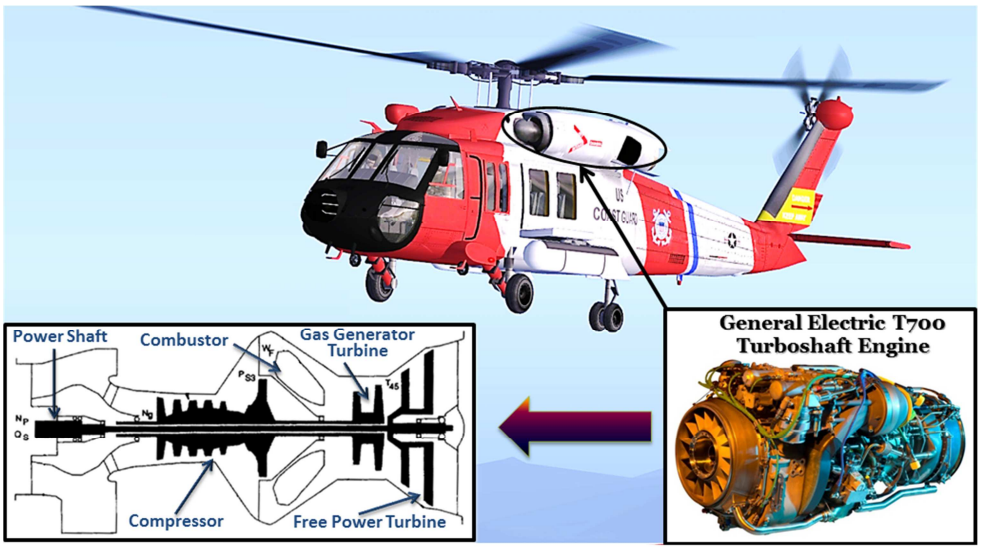

Figure 5.1. The UH-60 Black Hawk helicopter mounting two GE T700 turboshaft engines.

In the next sections, we will first have a look at the data used to build the models of the GE T700 and the UH-60. A validation against experimental data will be given for the engine model in section 5.2 and for the main rotor and helicopter model in section 5.3. Subsequently, it will be described how to find the optimal rotational speed minimizing fuel consumption; in this Chapter, we will deal only with a traditional helicopter configuration, employing a fixed-ratio transmission. Finally, the results output from the optimization in different flight conditions will be shown and discussed. The work exposed in this Chapter was presented at the 69th American Helicopter Society (AHS) Forum, Phoenix, 2013; it was given the Best Paper Award in the Propulsion Session, and has been published in the Journal of the AHS [1].

5.2 Validation vs. Experimental Data for the GE T700 Model

The power plant used in the UH-60 is the GE T700, an engine for which several data, available in the open literature, can be found to build a reasonable model [2],[2],[4],[5]. It is a two-spool turboshaft engine, composed of a five stage axial - one stage centrifugal compressor and two axial turbines: a gas generator turbine (GGT) driving the compressor and a FPT delivering torque and power to the external load. A schematic representation of the engine model is visible in Figure 5.2, while the related TSHAFT model is depicted in Figure 5.3.

The Design Point (DP) data needed to build the engine model are listed in Table 5.1; the design values for free power turbine RPM (N_{FPT}) and power load (P_{load}) are obtained from the manufacturer's engine data.

Air mass flow [kg/s]	**4.612**
Inlet recovery factor	**0.988**
Compressor pressure ratio	**17.50**
Compressor isentropic efficiency	**0.821**
Compressor design speed [RPM]	**44700**
Combustor relative pressure loss	**0.04**
Combustion efficiency	**0.985**
Fuel upper heat of combustion [MJ/kg]	**43.10**
GGT isentropic efficiency	**0.85**
GGT mechanical transmission efficiency	**0.99**
FPT design speed [RPM]	**20900**
FPT isentropic efficiency	**0.85**
FPT mechanical transmission efficiency	**0.99**
FPT Design Power Load [kW]	**1343.8**
Nozzle isentropic efficiency	**0.9**

Table 5.1. Design data used to build the GE T700 turboshaft engine model.

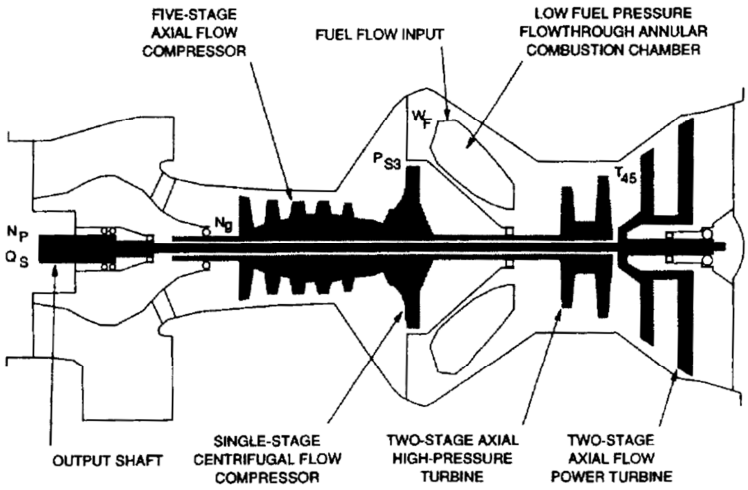

Figure 5.2. The GE T700 turboshaft engine [5].

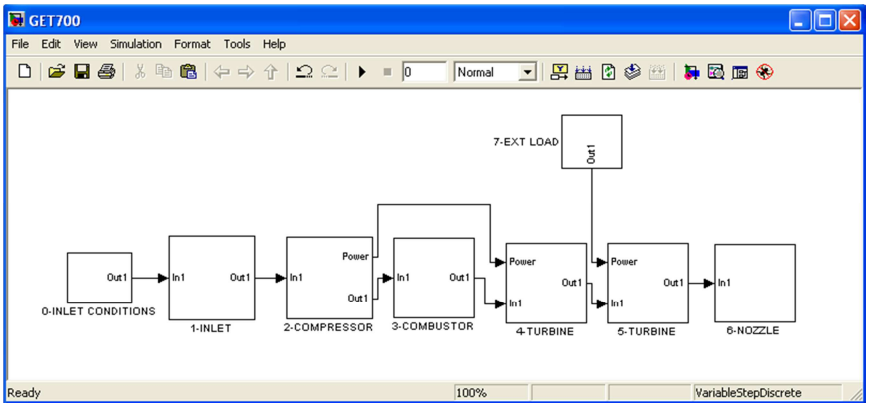

Figure 5.3. GET700 turboshaft engine model built using TSHAFT.

	Station 1	Station 3	Station 4	Station 5	Station 6	Station 7
Total Temperature [K]	288.2	715.1	1503.9	1152.7	910.8	910.8
Total pressure [bar]	1.013	17.519	16.818	4.072	1.227	1.203
Total enthalpy [kJ/kg]	0	441.4	1370.5	934.5	646.7	646.7
Specific entropy [J/(kgK)]	0	120.2	1000.8	1069.4	1126.6	1132.1
Specific heat [J/(kgK)]	1004.3	1078.5	1264.8	1213.7	1162.9	1155.3
Power Load [kW]	1343.8					
Engine efficiency	0.2989					
SFC [kg/kWh]	0.2794					
Fuel mass flow [kg/s]	0.1043					

Table 5.2. Results of the Design Point Simulation.

Firstly, a DP simulation was performed and the obtained results are summarized in Table 5.2. The ambient conditions for the engine DP simulation are chosen to be ISA standard at sea level (*T=288.15 K, p=101325 Pa*). The DP data are necessary to fix the virtual geometry of the engine and therefore rescale

turbine and compressor maps. In fact, these input data alone are not sufficient to build an engine model able to predict performance at all conditions, because off-design simulations require component maps. Since map characteristics of the turboshaft engine studied are not publicly available, some generalized maps in table form, found inside the GSP library, were used. The scaling procedure employed was based on a simple proportional criterion: every single map parameter is divided by its design point value[§]. This approximation perhaps represents the major source of deviation from experimental measures.

Compressor characteristic interpolation was performed employing auxiliary coordinates (usually named β lines, see Appendix), which are particularly useful in helping the off-design optimization algorithm to converge and visually define the interpolation domain. The off-design steady state solver is also able to calculate engine conditions at operating points out of this domain; however, since the values derived from the map will be extrapolated, the accuracy of the results will decrease as the distance of the operating point from the interpolation domain increases. Turbine characteristic interpolation, instead, is performed directly without the use of any additional parameter.

The performance results obtained using TSHAFT are compared against experimental data collected at the NASA Lewis Research Center by Ballin [2]. The validation process is carried out on six operating conditions featuring different inlet conditions and external loads, reported in Table 5.3.

Test Case	W_f lb_m/hr	$P2$ $PSIA$	$T2$ $°R$	$P49$ $PSIA$	Load Torque $ft - lb_f$
1	140.1	14.37	516.7	14.37	30.1
2	297.2	14.17	515.6	14.43	90.1
3	372.0	14.16	508.3	14.46	148.3
4	458.4	14.09	508.0	14.60	206.5
5	560.6	14.02	507.2	14.63	274.3
6	694.4	13.92	507.2	14.72	360.8

Table 5.3. Test conditions for NASA-Lewis experimental test engine[†] (from Ref [2]). W_f is the fuel flow, *P2* and *T2* are the measured total pressure and temperature at the AIP, *P49* is the FPT exit pressure.

[§] See appendix A for the description of an adequate scaling procedure.

[†] The NASA test data are related to a slightly modified version of the GE T700, but the differences with the original are very small. The power plant performance differs from a standard T700 of only few percentage points, which will not affect the validity of the present analysis.

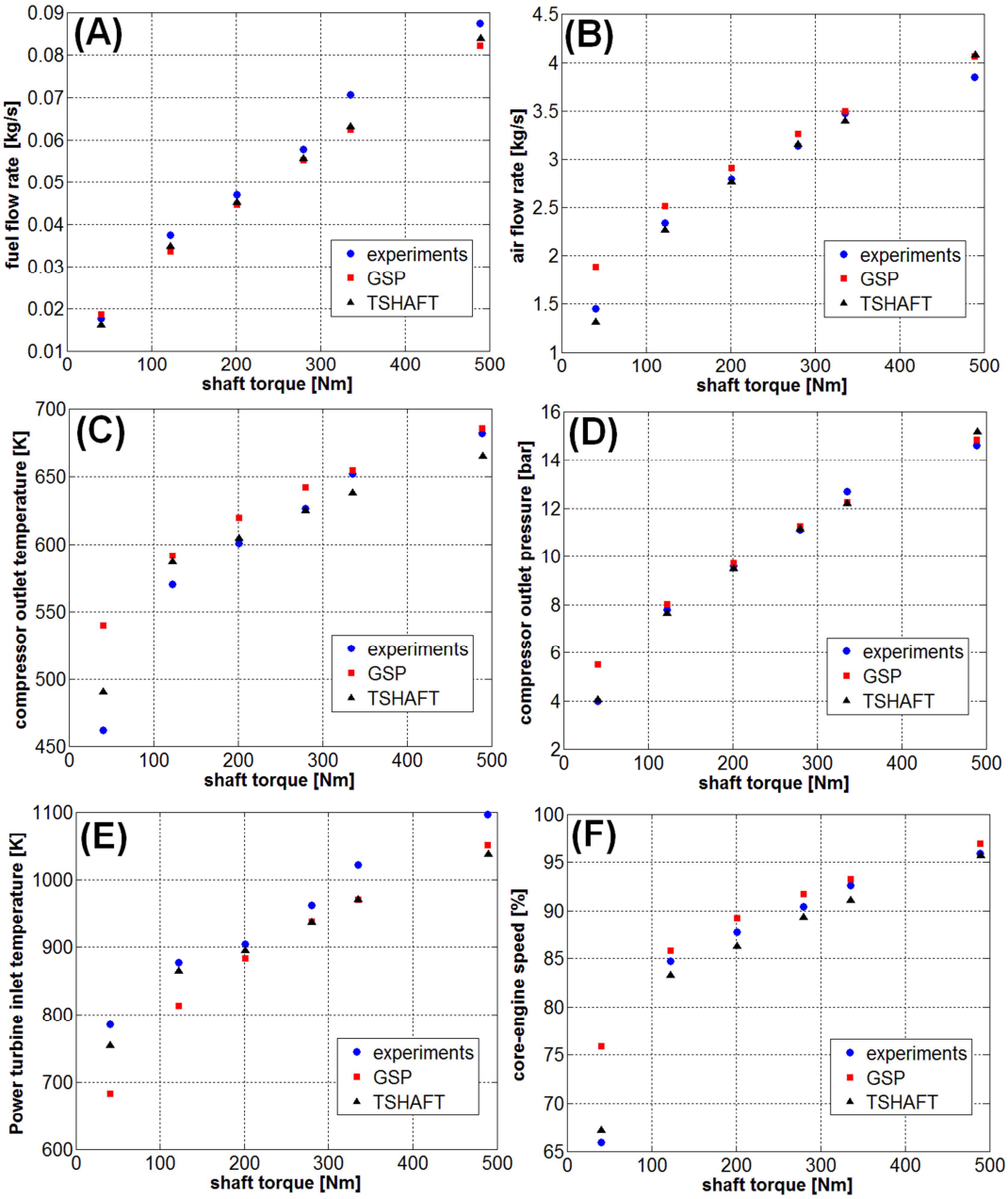

Figure 5.4. GE T700 turboshaft engine: comparison of TSHAFT model results with experimental data and GSP software: (A) Fuel flow; (B) Mass flow rate; (C) Compressor outlet temperature; (D) Compressor outlet pressure; (E) FPT inlet temperature; (F) Gas generator shaft speed.

Another engine model with the same input data is built using GSP software, in order to compare the two codes predicting capability with respect to the experimental test results.

The validation assessment is represented in Figure 5.4. Fuel consumption is the most interesting parameter to be observed. In fact, it represents the objective function of the minimization in the VSR analysis: failing to match it correctly

with the experiments would affect the entire reliability of the present study. The operational points generated by TSHAFT are in good agreement with the experimental data, with a maximum relative error on the various performance quantities in line with and in most cases even better than GSP calculations. As already stated, the principal cause of discrepancies between experimental and simulation results is probably found in the lack of knowledge of single engine component performance (especially component map data). Moreover, the real engine may involve the use of bleed valves to control stall margin, a phenomenon which is not introduced for lack of information. Bleed flows actually affect engine performance parameters, creating a deviation from predicted operation of some percentage points. Nevertheless, these comparisons show that the TSHAFT code is a valuable tool to predict the performance parameters of a generic turboshaft engine; in fact, they represent also the first validation of the software against real performance measures.

5.3 Validation vs. Experimental Data for the UH-60 Model

A model of the UH-60 Black Hawk helicopter is built using TCOPTER and collecting a set of real data which is reported in Table 5.4 and Figure 5.5. These data are available in the open literature, and most of those used for the simulation are found in NASA technical reports by Howlett [6] and other papers [7],[8].

Main rotor radius [m]	**8.178**
Main rotor blade chord [m]	**0.527**
Number of blades (main rotor)	**4**
Main rotor nominal speed [rad/s]	**27**
Transmission efficiency	**0.95**
Hinge offset [m]	**0.381**
Spar length [m]	**1.167**
Tail rotor radius [m]	**1.676**
Tail rotor blade chord [m]	**0.247**
Number of blades (tail rotor)	**4**
Tail rotor nominal speed [rad/s]	**124.4**
Tail rotor cant angle [deg]	**20**
Main rotor - tail rotor distance [m]	**9.93**

Table 5.4. UH60A construction data and other assumptions (Ref. 3).

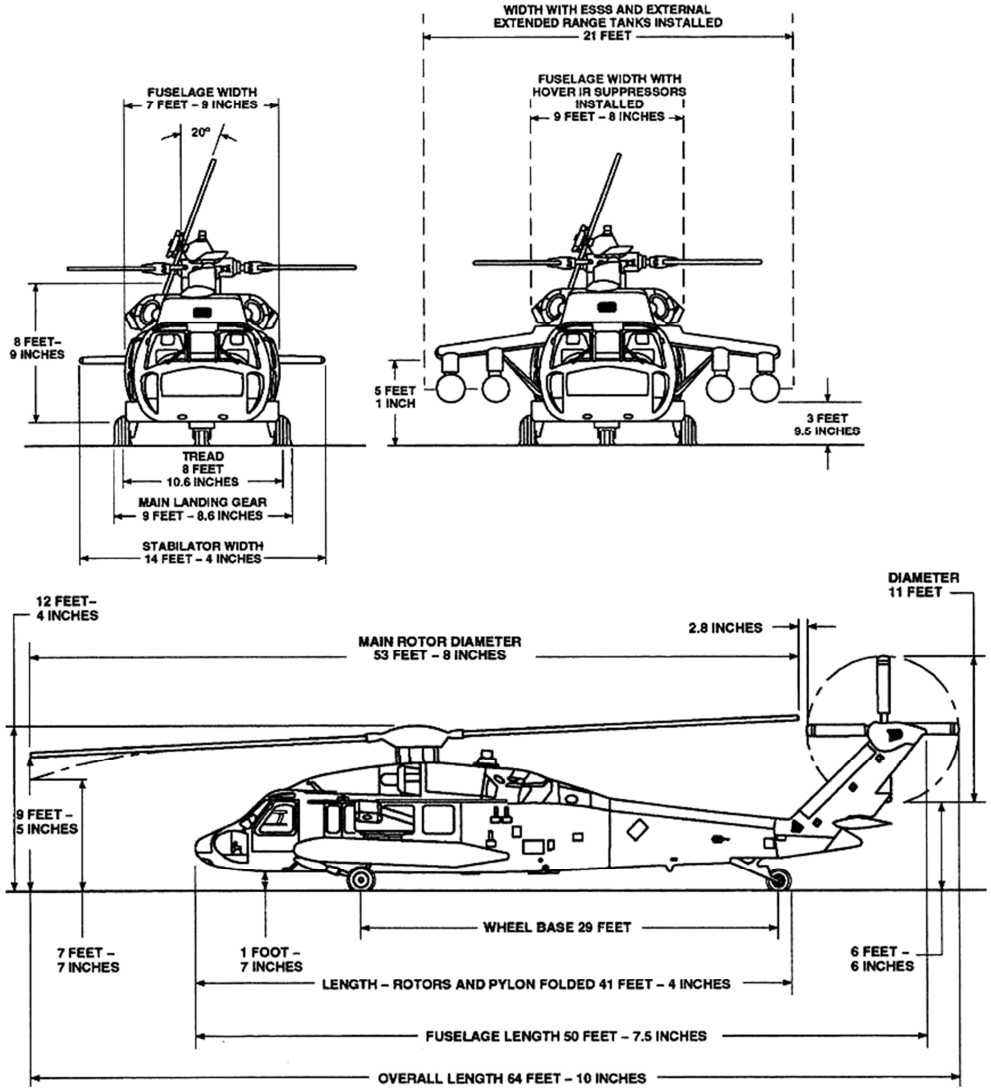

Figure 5.5. UH-60 Black Hawk helicopter: configuration and dimensions [9].

There are some additional assumptions used specifically inside the UH-60 simulations that are to be reported. Firstly, the blade tip loss is modeled with the well-known Prandtl tip-loss function. Secondly, the aerodynamic moments acting on the fuselage are neglected for the lack of data. The same holds also for the rear stabilator, which is not simulated. On the contrary, the fuselage lift and drag are taken into account using empirical expressions found in Yeo et al. [10]:

$$L_{fus} = \frac{1}{2}\rho V^2 (1.0239\alpha_{WL}{}^5 + 12.841\alpha_{WL}{}^4 - 39.558\alpha_{WL}{}^3 - 30.214\alpha_{WL}{}^2 + \\ + 106.09\alpha_{WL} - 0.709) \tag{5.1}$$

$$D_{fus} = \frac{1}{2}\rho V^2 (35.14 + 0.0440896\alpha_{WL}) \tag{5.2}$$

From the same paper, the additional accessory power of 51 kW, typical of the average UH-60 operation, is derived and used in the model. Lift and drag coefficients are derived by interpolating the SC1095 airfoil characteristics found in Bousman [11]; the interpolation accounts for Mach number variation. A similar interpolation is used to account for the slightly nonlinear twist distribution.

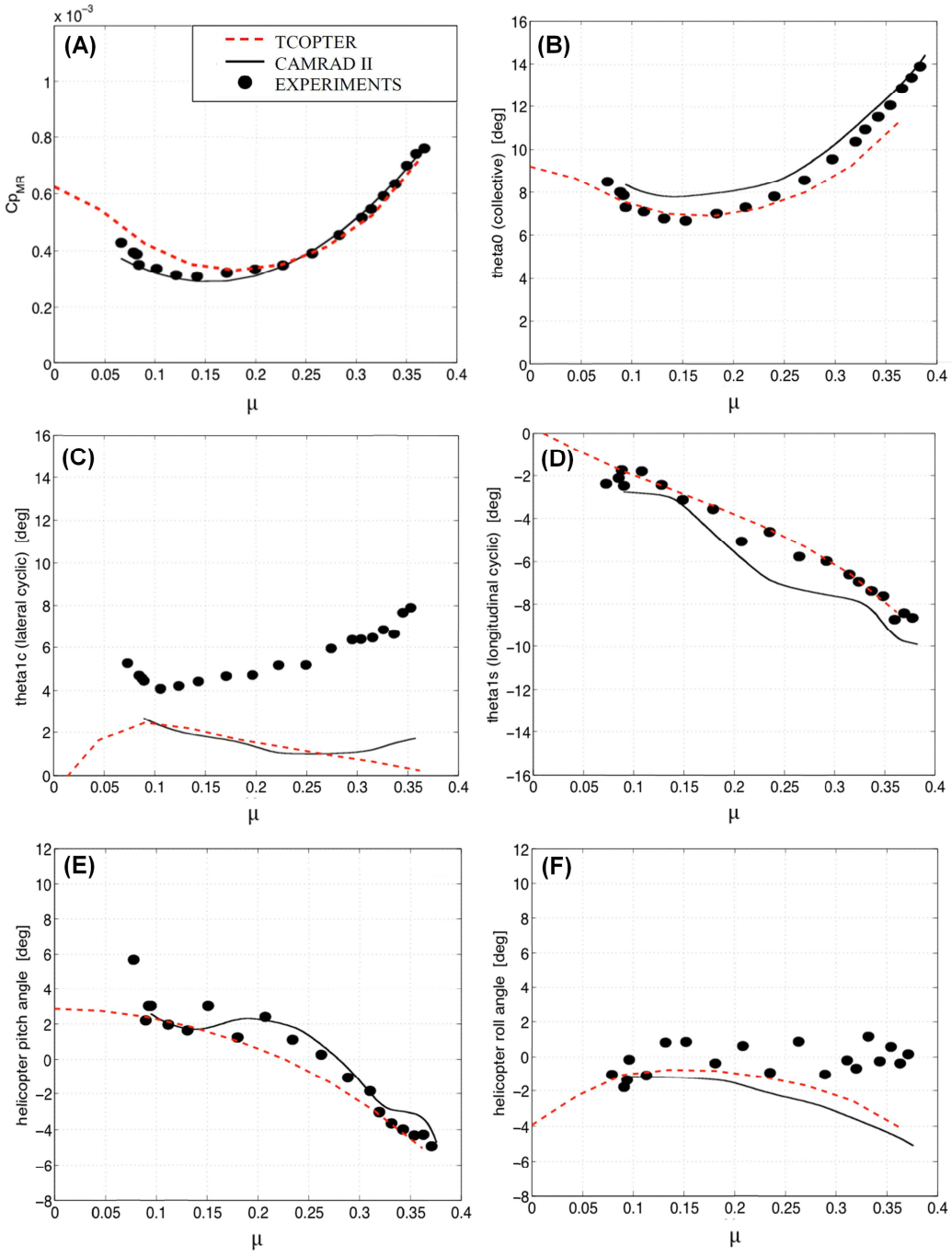

Figure 5.6 UH60 helicopter: comparison of TCOPTER model results with experimental data and CAMRAD II output from Yeo [10]: (A) Power coefficient; (B) Collective angle; (C) Lateral cyclic angle; (D) Longitudinal cyclic angle; (E) Pitch attitude; (F) Roll attitude.

Figure 5.6 shows the comparison between the current TCOPTER model, an aeromechanical analysis performed with CAMRAD II [12] and experimental measurements collected by Yeo et al. [10]. The results predicted by the TCOPTER model for the analyzed variables show a good compatibility with the experimental values. Particularly important for the current analysis is the good prediction of both the power coefficient and collective angle. As well, the longitudinal cyclic angle estimation is quite accurate according to that encountered experimentally. Since the main goal of the current analysis is given by a correct modeling of the engine power demand, there is less interest in accurate blade dynamics simulation, and some error related to the attitude angles and the control angles can be fairly accepted. However, all helicopter trim parameters find quite a good adherence with experimental measurements by using the abovementioned assumptions.

Summarizing, the UH-60 model can be considered validated in first approximation, since the most important parameter estimated, the power coefficient, is very close to the C_p measured. The highest error is found in the hovering region (the most difficult region for BEMT model prediction), where C_p is slightly overestimated.

5.4 FRT Optimal Ω Calculation Scheme

The primary objective of the present study consists in merging together the turboshaft engine and helicopter trim models to create an overall helicopter performance model. In this way it is possible to build an optimization algorithm which runs the helicopter model seeking for the best main rotor speed Ω, in different flight conditions. The objective of the algorithm is to adjust Ω in order to minimize the engine fuel mass flow, taking into account the different requirements of the main rotor and the turboshaft engine. Despite the large number of nonlinear equations employed in the two different models, the optimization algorithm has to solve a univariate minimization problem, thus a wide variety of algorithms can be used. For the case study at hand, a derivative-free algorithm, the golden section search method with parabolic interpolation is chosen.

In Figure 5.7, the optimization process is graphically schematized; remind that we are analyzing a standard fixed-ratio transmission helicopter. The input values of ambient conditions and forward speed are needed for both the main rotor and engine models. Once a tentative value for Ω is chosen, from the

helicopter trim simulation the power absorbed by the rotor P_{MR} can be derived, whereas from the fixed transmission ratio the FPT speed can be evaluated:

$$\Omega_{FPT} = k_{trans}\Omega \tag{5.3}$$

The power requested to the engine is actually given by the sum of main rotor power, tail rotor power and additional accessory power. If a helicopter mounts two different turboshaft engines, as in the case of the UH-60, the power is supposed to be equally divided between the two. Therefore, accounting for transmission losses, the single engine power load becomes:

$$P_{load} = \frac{(P_{MR} + P_{TR} + P_A)}{2\eta_{trans}} \tag{5.1}$$

These data are then inserted as input values in the engine model, which in turn computes engine fuel consumption m_f. Next, the optimization algorithm computes a new value for Ω and restarts the process until the minimum in fuel consumption is reached. Note that this optimization process must be accomplished for each different flight condition taken into consideration.

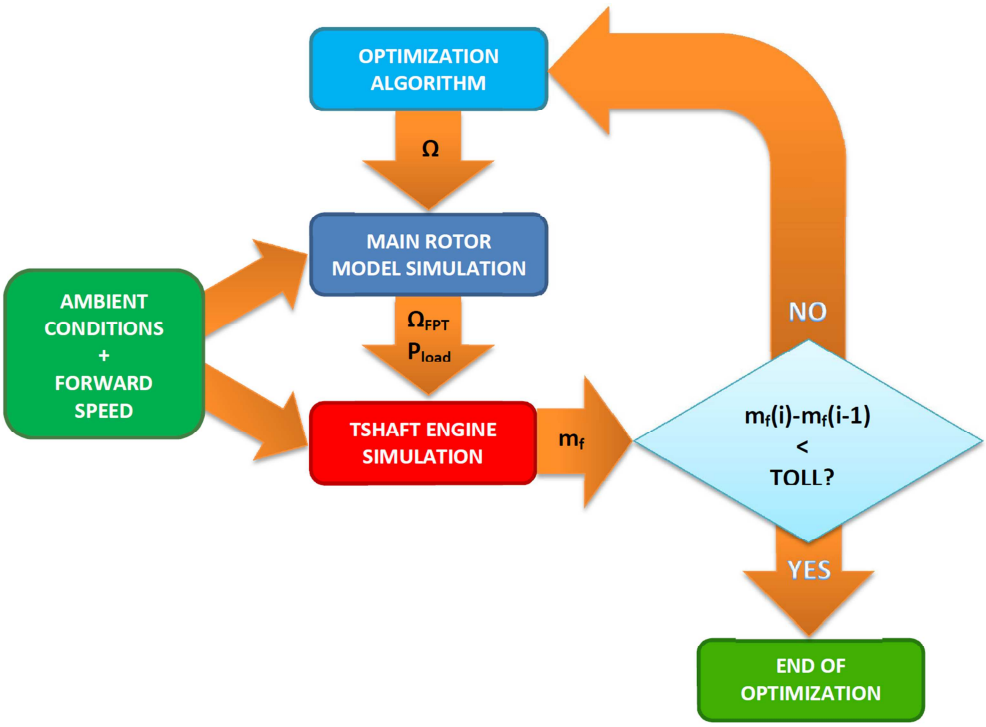

Figure 5.7. Optimal speed determination process for a fixed-ratio transmission helicopter.

5.5 Simulation Results

In order to obtain a good overview of how an optimal main rotor speed could reduce fuel consumption, five steady state cases at level flight are simulated with different weights and altitudes. For each case, 19 simulations are carried out to cover the advancing speed interval from 0 to 90 m/s. It is clear that there will be different optimal speeds depending on different weights and altitudes, since the power required to maintain level flight is clearly dependent upon these parameters.

Three simulations are performed with a constant weight of 7257 kg (16000 lbs) at the following altitudes and ambient temperatures:

- Sea level (0 m), T=302 K
- 2100 m, T=288 K
- 4200 m, T=274 K

The reference temperatures used for the three different altitudes are chosen as typical of a hot summer day (ISA+14°C).

Further simulations are carried out maintaining the constant altitude of 2100 m, T=288 K, and varying the helicopter gross weight:

- 5443 kg (12000 lbs)
- 7257 kg (16000 lbs)
- 9071 kg (20000 lbs).

One may think that, instead of performing the simulations with a sweep in altitude and weight, simulating different values of C_T would have been sufficient to understand the effects of both variables. In fact, this is true for the helicopter model alone, where the power required by the main rotor is directly dependent on air density: in first approximation, a change in altitude is equivalent to a change in density, and nothing else. Unfortunately, engine performance significantly depends not only on air density, but also on temperature (or, alternatively, pressure). Therefore, if we compare two helicopter configurations with the same C_T, but different weights and altitudes, the engine performance will be different, because it is also dependent on temperature, which varies with altitude. This justifies the need to simulate both the effects, altitude and weight, to obtain a correct overall performance estimation.

5.5.1 Complete results for the 2100m, 7257 kg case

The simulation at 2100 m for a gross weight of 7257 kg is chosen to show the amount of information that can be derived from the optimization methodology

discussed in the previous sections. The remaining ones will be only used to understand the various trends in the most interesting parameters. The optimal main rotor speed is expressed as a function of advancing speed V in Figure 5.8. The first thing to notice is that the optimal Ω is lower than the constant speed for the entire V interval. Moreover, the variation in Ω is still inside the 15% boundary in which a usual helicopter engine operates. In Figure 5.9, the objective function of the optimization, fuel consumption, is shown along with the engine shaft torque.

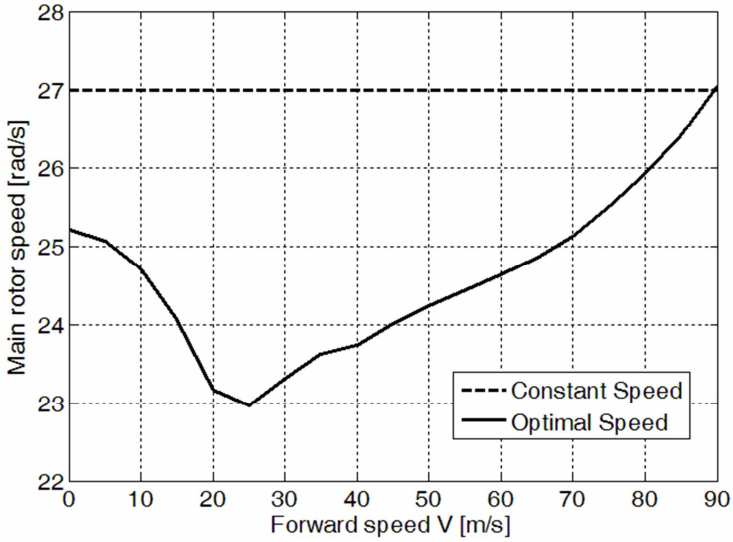

Figure 5.8. Optimal main rotor speed compared to constant design speed (27 rad/s).

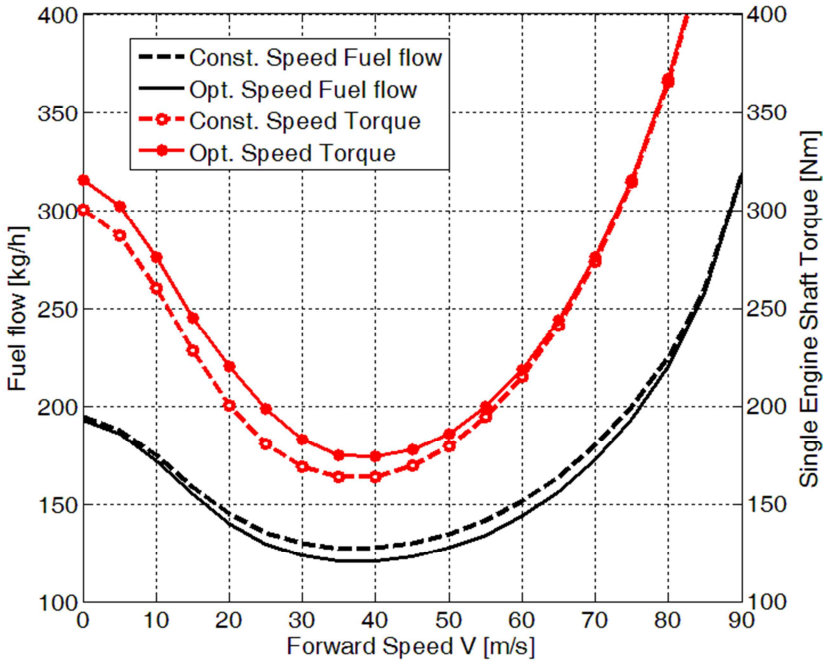

Figure 5.9. Fuel flow and shaft torque (single engine) for constant and optimal speed.

It is clear that optimal speed has achieved a good result, since fuel consumption is lower in the entire flight speed interval, and the best results are found for intermediate forward speeds, in accordance with previous studies [2]. Fuel consumption reduction is also accompanied by a reduction in total helicopter power, as will be clear in the next section (Figure 5.15-Figure 5.16). Despite the power reduction, optimal Ω operation leads to a higher engine shaft torque (Figure 5.9): in fact, the decrease in Ω with respect to the constant speed case more than compensates the power reduction, with the net effect of increasing engine torque. However, this is a minor drawback; the torque increase is small and vanishes at higher speeds: in fact, the maximum transmission torque load observed inside the V interval is the same for both cases. Now, it is interesting to analyze the operating points on the two most important components of the turboshaft engine, i.e. the FPT and the compressor. From Figure 5.10 it is evident that there is no shift in the compressor operating line between the two cases compared, as expected. In fact, for a turboshaft engine operating in steady state conditions, the working line is fixed as long as the gas generator turbine is choked, namely the vast majority of its operating envelope. However, the points related to the optimal Ω line are moved towards lower corrected speed lines, a clear indication that the power requested from the rotor is lowered.

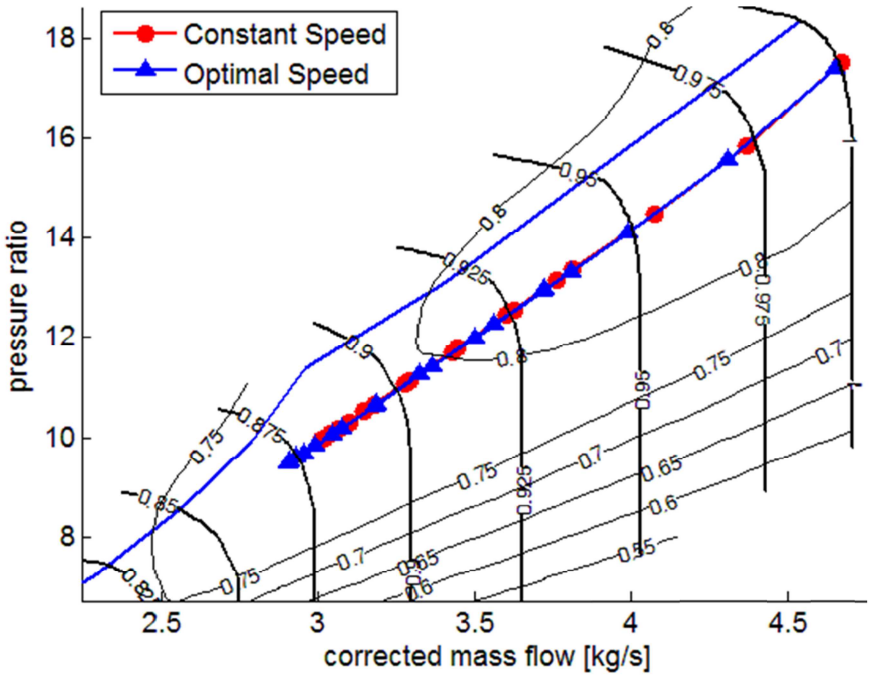

Figure 5.10. Operating line on compressor map characteristic for both constant and optimal speed.

In Figure 5.11 both the turbine operating lines of constant and optimal Ω are traced. The optimization leads to an evident displacement of the engine running line; however, it is unclear if it is directed towards higher levels of isentropic efficiency, as it would have been when optimizing turboshaft engine efficiency [12]. Figure 5.12 clarifies the trend: only for a short range of intermediate values of V the optimal speed achieves an improvement in FPT efficiency; instead, for low and high values of V the constant Ω is characterized by a higher FPT efficiency: in this case rotor power minimization is a slightly opposing goal. This behavior is not encountered for every altitude and weight, as will be seen later.

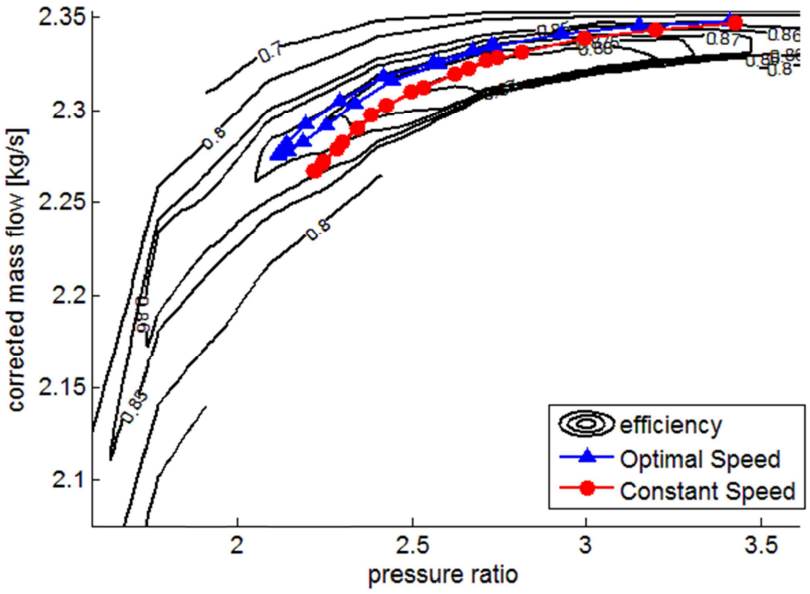

Figure 5.11. Operating line on FPT map characteristic for both constant and optimal speed.

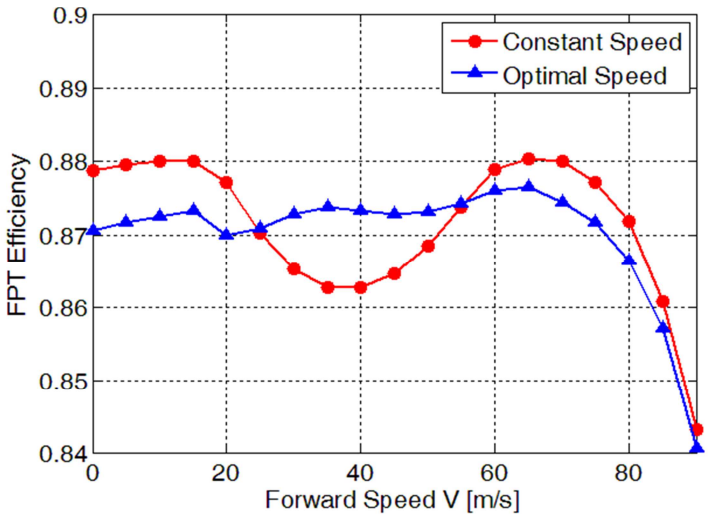

Figure 5.12. FPT efficiency for both constant and optimal speed.

The last interesting observation to be made is related to finding a physical explanation to the reduced Ω found by the optimization algorithm. Let us analyze the condition at which minimum fuel consumption is reached, namely the one at 35 m/s. In Figure 5.13-Figure 5.14 the angle of attack α seen by the rotor blades is plotted along the rotor disk for constant and optimal Ω, respectively. A significant increase of α is encountered when operating at optimal speed: this means that the algorithm is reducing profile power by lowering the rotational speed. Hence, in order to compensate for the loss of thrust due to Ω reduction, the angle of attack has to be increased.

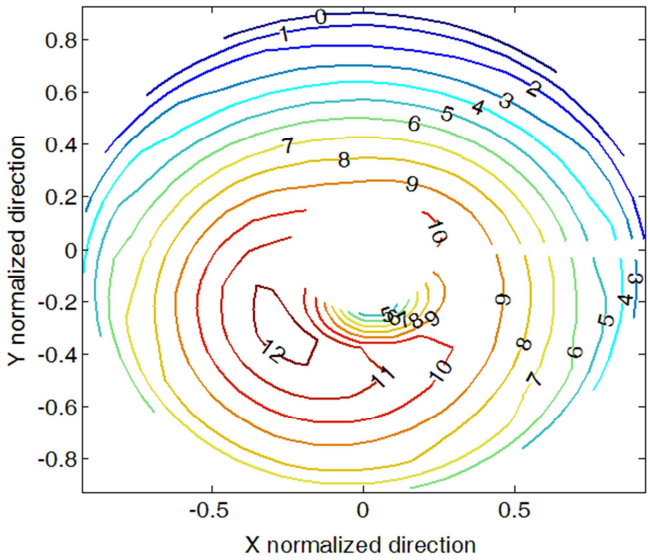

Figure 5.13. Angle of attack distribution for the constant speed case, V=35 m/s.

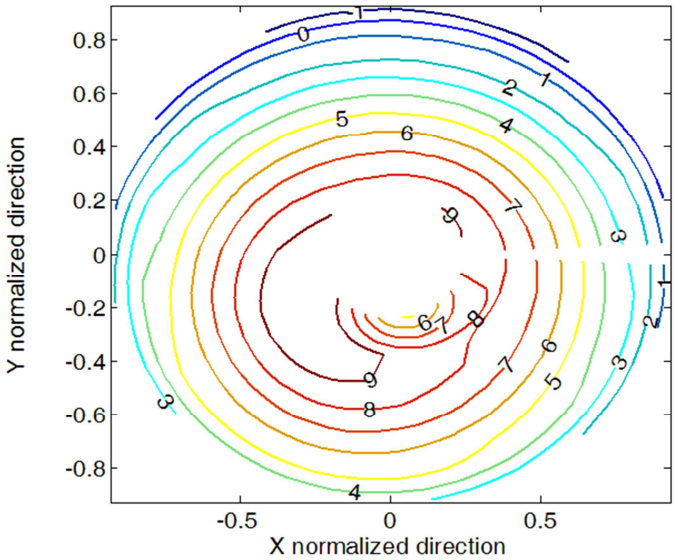

Figure 5.14. Angle of attack distribution for the optimal speed case, V=35 m/s.

5.5.2 Main Rotor Power Comparison

Main rotor power variation is the primary indicator of rotor efficiency changes, and therefore it is a parameter to be carefully studied. First, observe the discrepancies in power absorption between the optimized and constant case at different weights and altitudes (Figure 5.15-Figure 5.16). It is clear that optimal rotor speed operation is particularly advantageous at sea level, where for the entire V range a substantial power reduction is noticed. This reduction vanishes at 4200 m, proving that the constant speed of 27 rad/s is already near to the optimal speed for this altitude (in Figure 5.15 Ω related to the 4200 m case is the nearest to the constant 27 rad/s case). The significant difference between main rotor optimal speed and constant speed in hover, corresponding to almost the same power, may be due to a slightly better trade-off between turbine efficiency and rotor efficiency. At 65 m/s there is a sudden peak in power for the constant speed line. Since no point on the blade is reaching Ma=1, retreating blade stall is the most reasonable explanation.

The same occurrence is found for the high weight case (9071 kg), this time at a forward speed 10 m/s higher (Figure 5.16). This case is also characterized by a strong proximity between the values of optimal and constant Ω. The last two cases have something in common: at high speeds a higher altitude or a higher weight, when Ω is constrained to the same value, inevitably leads to a higher collective angle. This is translated into higher angles of attack at the blade, which imply retreating blade stall and a consequent intense increase in profile drag. The optimization algorithm, instead, seems to solve the problem by increasing Ω to move away from blade stall (but still ensuring no sonic conditions at the blade tip) and maintain the rotor inside an acceptable operating envelope.

The phenomena encountered here at high forward speeds are in quite good accord with the trends individuated by Steiner in his work [13]; he noticed that some peaks occurred before finding a limit condition where helicopter trim was no longer possible. On the contrary, the optimal Ω seems to extend the operating envelope of the helicopter, permitting a weaker increase in rotor power at high forward speeds by avoiding retreating blade stall.

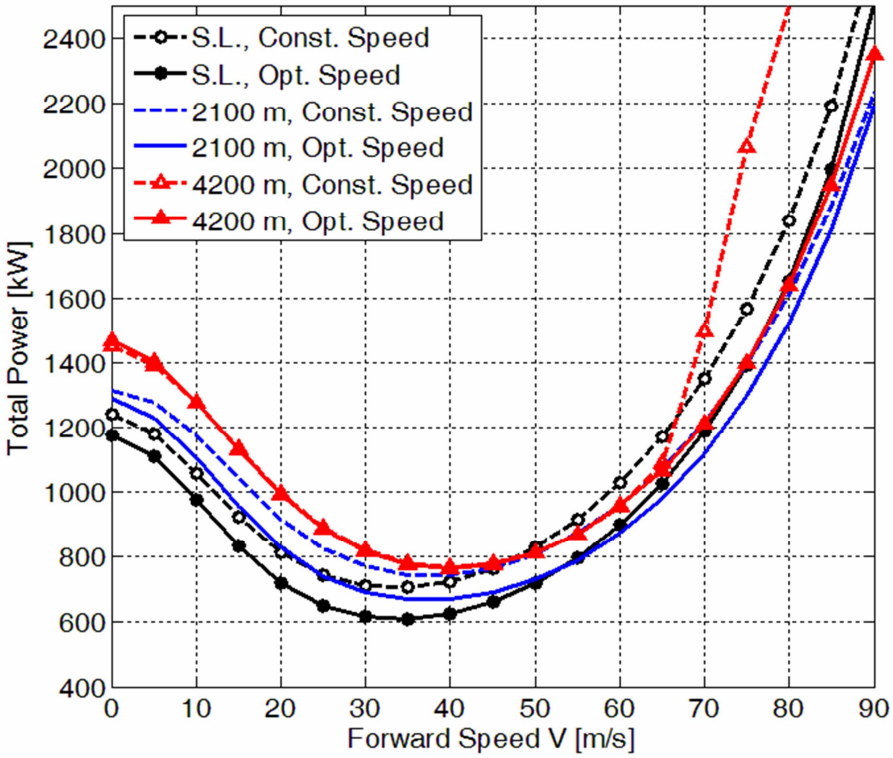

Figure 5.15. Total helicopter power at different altitudes (W=7257 kg).

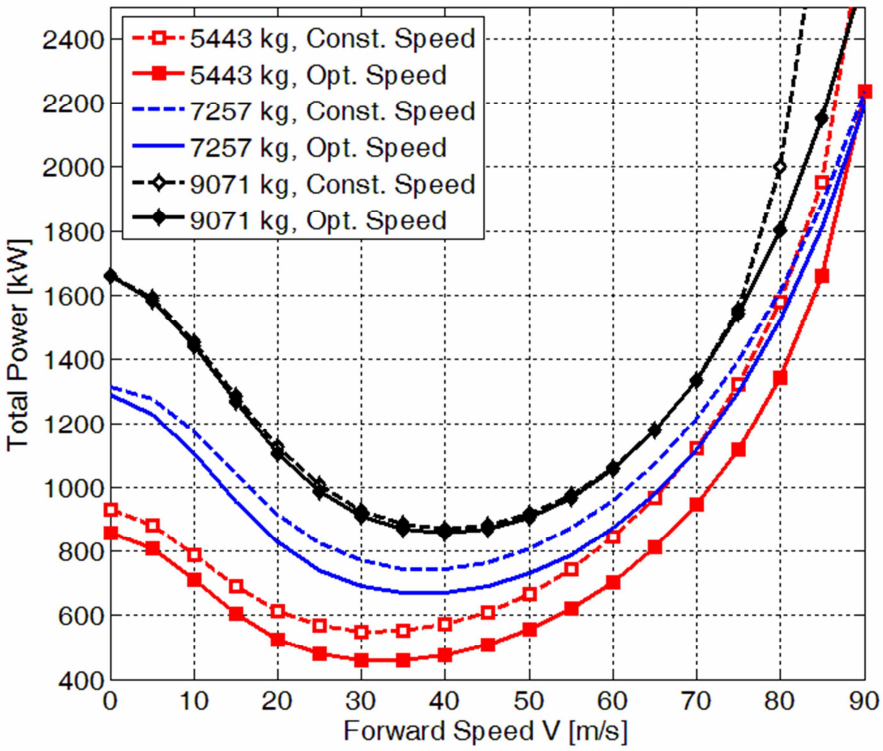

Figure 5.16. Total helicopter power for different helicopter gross weights (*h*=2100 m).

5.5.3 Fuel Flow Reduction

The main goal driving this Chapter analysis is represented by the possibility to obtain a significant fuel reduction by using a VSR on a standard helicopter (UH-60). The percentage reduction achieved by the optimization process is presented in Figure 5.17 for different altitudes and in Figure 5.18 for different weights; in Figure 5.19 and Figure 5.20, instead, the optimal Ω responsible for fuel reduction is plotted for the entire advancing speed range of the helicopter. In the lower and intermediate V interval, a maximum fuel reduction of 13% is observed for the 5443 kg at 2100 m case.

As a rule of thumb, it is possible to conclude that the optimal main rotor speed achieves the best results, in terms of fuel consumption, at lower weights and lower altitudes. In practice, it seems that the farther from the design conditions, the more useful the approach presented. This is true for advancing speeds still far from the blade stall condition.

For high V values, the optimal Ω seems to produce another beneficial effect, retarding blade stall. In this region high gains of fuel consumption are output by the helicopter and turboshaft models. However, these results have to be carefully analyzed, because constant speed operation at 27 rad/s cannot be realized in practice for the engine. In fact, some of the constant Ω conditions analyzed could not occur in practice because of the too high maximum cycle temperature reached inside the turboshaft engine. Moreover, at these high powers, the corresponding operating points are falling out of the compressor and FPT map, strongly decreasing the reliability of the results output by the turboshaft model. This simply means that standard constant speed operation is no more possible, so it does not make any sense to calculate an estimation of fuel reduction. On the contrary, optimum Ω operation permits to reduce the combustor temperature to an acceptable level, proving that the flight envelope of the helicopter has been widened.

As a further note to the reader, it has to be noted that numerical convergence has been verified inside both the helicopter trim and the turboshaft models, for the entire set of simulations performed. The relative tolerances were found always lower than 10^{-6}. It has to be remarked that the optimization routine, when far from the constant design condition of 27 rad/s, demonstrates that significant benefits can be obtained at both high and low speeds by employing an optimal Ω.

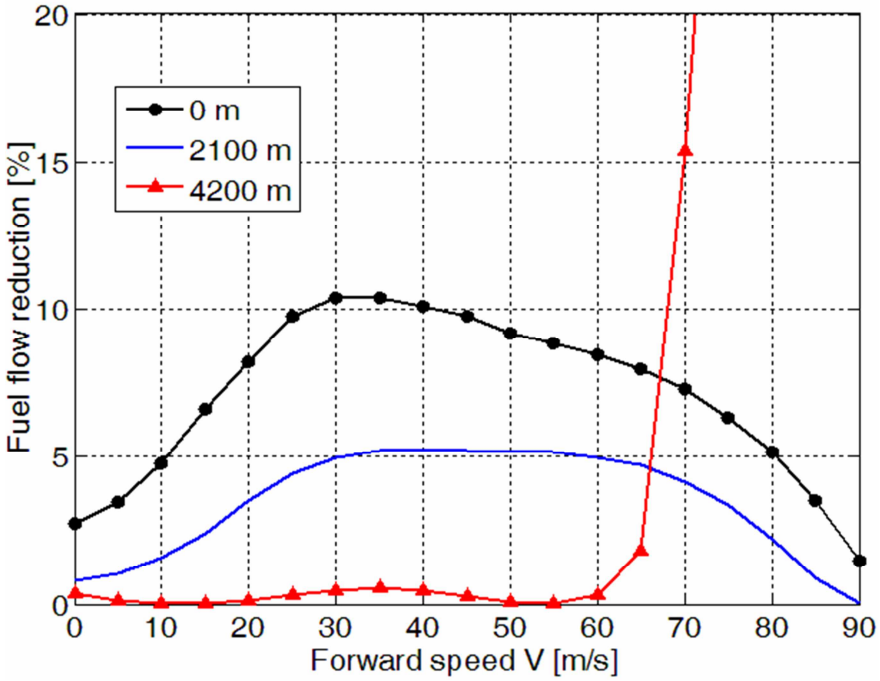

Figure 5.17. Fuel flow reduction at different altitudes (W=7257 kg).

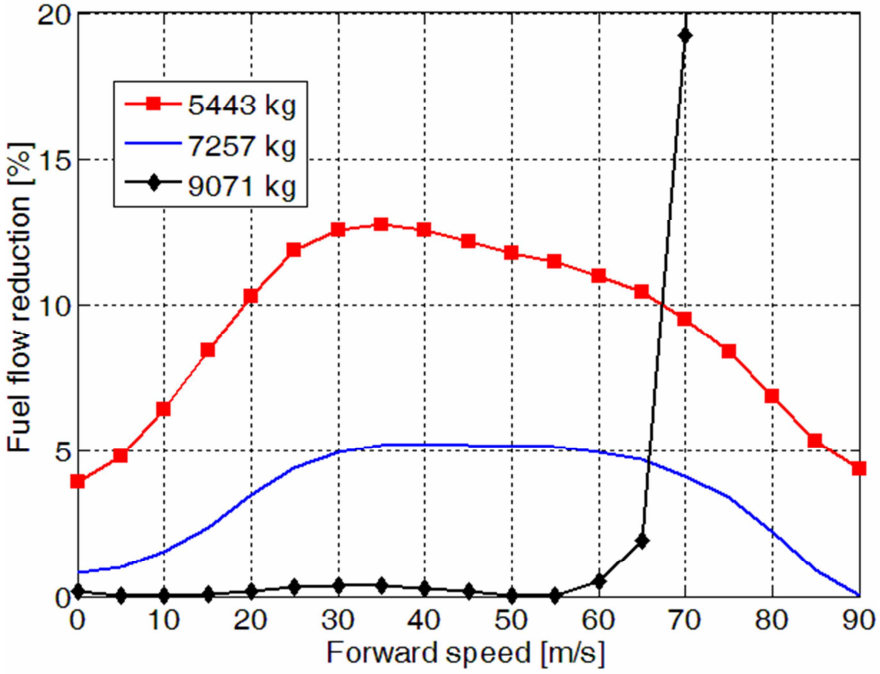

Figure 5.18. Fuel flow reduction for different helicopter gross weights (h=2100 m).

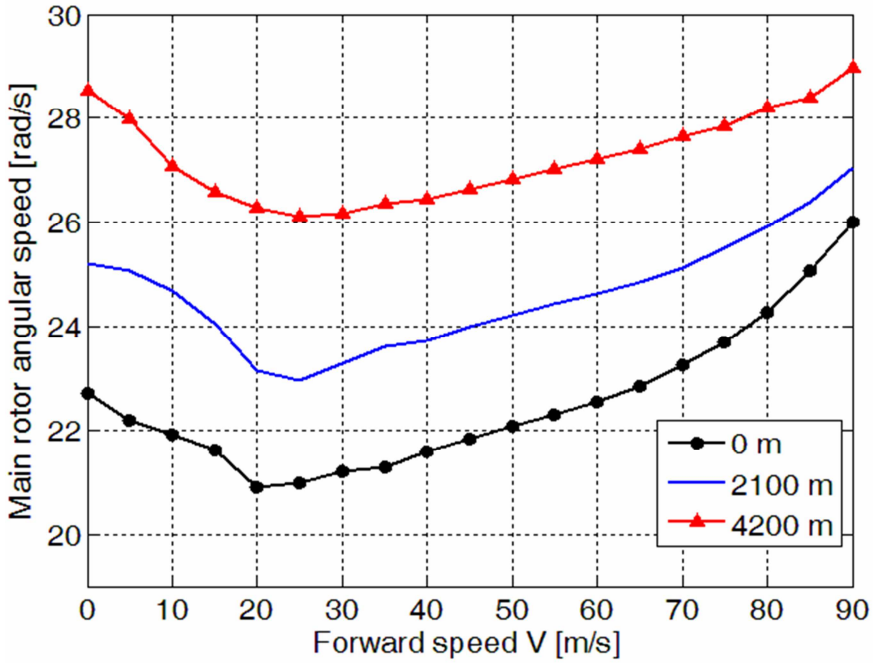

Figure 5.19. Main rotor optimal speed at different altitudes (W=7257 kg).

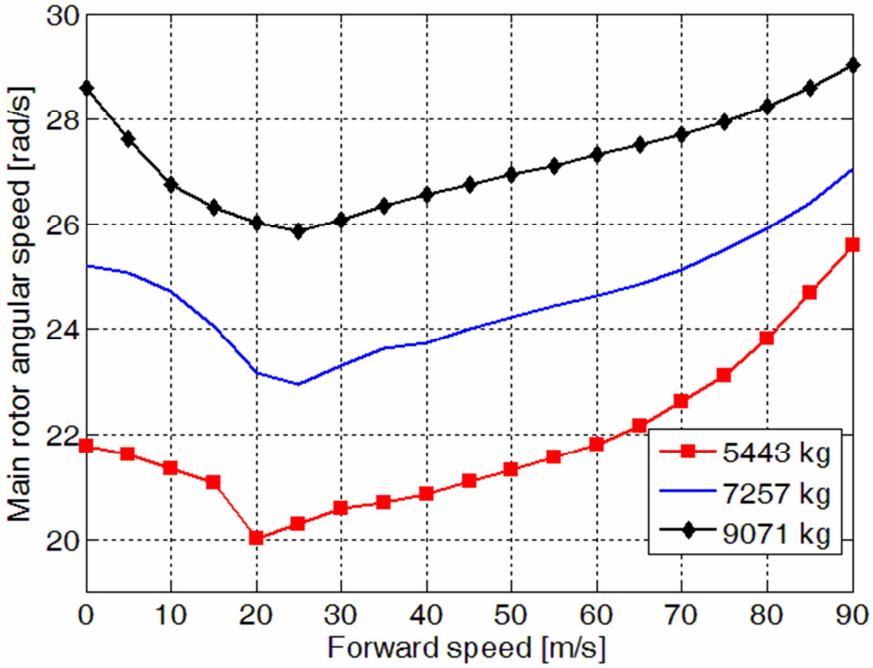

Figure 5.20. Main rotor optimal speed for different helicopter gross weights (h=2100 m).

5.5.4 Power Minimization vs Fuel Flow Minimization

In this last section it will be shown how neglecting to model the turboshaft engine would affect optimal main rotor calculation. Let us define the main rotor optimal speed minimizing total helicopter power as $\widehat{\Omega}_{MR}$, while we will refer to the usual optimal speed minimizing fuel consumption as $\widehat{\Omega}$. In Figure 5.21 fuel consumption reduction is calculated using the two different optimal speeds. It can be seen that in the optimization algorithm the main driving parameter is represented by main rotor power, since $\widehat{\Omega}$ follows quite nearly $\widehat{\Omega}_{MR}$. However, the engine simulation becomes relevant at low V region: the introduction of the turboshaft model requirements can be seen as a constraint to the main rotor optimization. In fact, if the power minimization algorithm is left free to vary Ω inside the low V region, main rotor power minimization is no longer equivalent to fuel consumption minimization. Moreover, if we take a look at the hovering condition, $\widehat{\Omega}_{MR}$ is even causing an increase in fuel consumption: in this condition, main rotor power minimization is counterbalanced by poor engine performance. This justifies the effort to model both main rotor and turboshaft engine performance to correctly determine the trend in fuel consumption reduction.

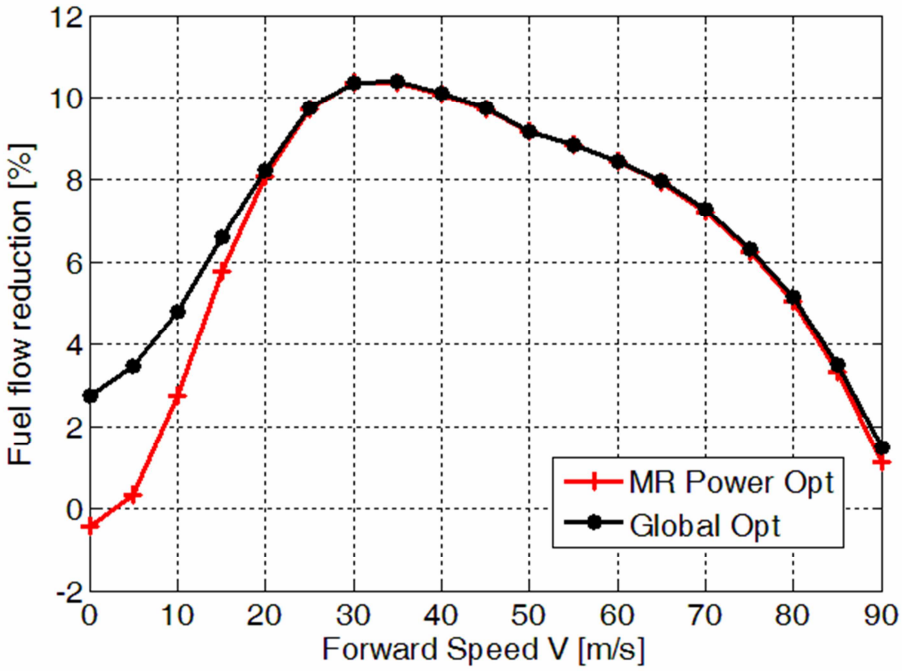

Figure 5.21. Comparison of fuel saving achieved by $\widehat{\Omega}$ and $\widehat{\Omega}_{MR}$ (W=7257 kg, sea level).

5.6 References

[1] G. A. Misté, A. Garavello, E. Benini, and M. Gonzalez-Alcoy, *A New Methodology for Determining the Optimal Rotational Speed of a Variable RPM Main Rotor/Turboshaft Engine System*, Proceedings of the American Helicopter Society 69th Annual Forum, Phoenix, Arizona, USA, May 2013.

[2] M. G. Ballin, *A high fidelity real-time simulation of a small turboshaft engine*, NASA Technical Memorandum 100991.

[3] A. Garavello, E. Benini, *Preliminary Study on a Wide Speed Range Helicopter Rotor/Turboshaft System*, AIAA Journal of Aircraft, vol. 49 no. 4, pp. 1032-1038), 2012.

[4] A. Duyar, Z. Gu, J.S. Litt, *A Simplified Dynamic Model of the T700 Turboshaft Engine*, NASA Technical Memorandum 105805.

[5] C. Ozsoy, A. Duyar, R. Kazan, R. Kiliç, *Power Turbine Speed Control of The GE T700 Engine Using The Zero Steady-State Self-Tuning Regulator*, Proceedings of International Conference on Intelligent Engineering Systems, INES '97, 15-17 Sep 1997, Budapest, pp. 371 – 378. ISBN: 0-7803-3627-5.

[6] J.J. Howlett, *UH-60A Black Hawk Engineering Simulation Program: Volume I-II*, NASA Contractor Report 166309-166310, December 1988.

[7] M.G. Ballin, *Validation of a Real-Time Engineering Simulation of the UH-60A Helicopter*, NASA, TM 88360, 1987.

[8] R.M. Buckanin, *Rotor System Evaluation: Phase I*, AEFA Project No. 85-15 Final Report, March 1988.

[9] www.sikorsky.com/Pages/Products/Military/BlackHawk/UH60M.aspx

[10] H. Yeo, W. Bousman and W. Johnson, *Performance Analysis of a Utility Helicopter with Standard and Advanced Rotors*, Journal of the American Helicopter Society, January 2005.

[11] W. G. Bousman, *Aerodynamic Characteristics of SC1095 and SC1094 R8 Airfoils*, NASA/TP–2003-212265, 2003.

[12] W. Johnson, *A Comprehensive Analytical Model of Rotorcraft Aerodynamics and Dynamics, Part 1*, NASA TM 81182, 1980.

[13] G. A. Misté and E. Benini, *Performance of a Turboshaft Engine for Helicopter Applications Operating at Variable Shaft Speed*, ASME Gas Turbine India Conference 2012 Proceedings, Mumbai.

[14] J. H. Steiner, *An Investigation of Performance Benefits and Trim Requirements of a Variable Speed Helicopter Rotor*, MSc Thesis, The Pennsylvania State University.

Chapter 6

Fixed Ratio vs Variable Speed Transmission

6.1 Introduction

As explained in the previous sections (and also in Refs. [1],[2]), the analysis of main rotor and turboshaft engine subsystems coupling is fundamental to correctly understand fuel saving possibilities. For each different helicopter flight condition (depending on advancing speed, helicopter weight, and ambient conditions) it is possible to find an optimal rotational speed of the main rotor $\widehat{\Omega}_{MR}$, which minimizes helicopter absorbed power. In addition, for each different power load condition it is also possible to find an optimal FPT speed value $\widehat{\Omega}_{FPT}$ (or RPM value $\hat{N}_{FPT} = \widehat{\Omega}_{FPT} / 2\pi$) which minimizes engine(s) fuel consumption. These two optimal speeds are different, depending on each subsystem characteristics, and vary with flight conditions. In order to achieve maximum fuel saving, it is clear that optimal helicopter operation should employ $\widehat{\Omega}_{MR}$ for the main rotor and $\widehat{\Omega}_{FPT}$ for the engine FPT. However, state of the art helicopters employ a fixed transmission ratio between engine and main rotor angular speeds, therefore stating the impossibility of optimal operation for both subsystems, since main rotor speed is strictly dependent on engine speed. There is a clear advantage in leaving the two subsystems free to rotate at their different optimal speeds, and this may be achieved employing a variable speed transmission, especially in the form of a CVT. No such transmission is currently available for the helicopter requirements; however, it is important to quantify the potential performance gains that could be obtained using a CVT. How much fuel can we save using a CVT instead of a FRT, always assuming optimal speed operation? We will address this question in the present section.

There is no study in the open literature which analyzes the advantages and drawbacks of the FRT and CVT concepts from a performance standpoint, which can be interesting to understand the worthiness of these two approaches for future

research. Therefore, the present section deals with the investigation of the different theoretical performance achievable by these two variable speed concepts. The impact of the two types of transmission upon overall helicopter performance is estimated through a comparison between a FRT and a CVT, both operating at their optimal speeds. This is done by using an optimization strategy able to find the optimal rotational speeds of main rotor and FPT for each flight condition (level flight from 0 to 90 m/s). As in Chapter 5, three different altitudes are considered, and three different gross weight configurations for the same helicopter (the UH-60) are simulated in order to understand in which particular flight conditions the two variable speed concepts achieve the best reductions in fuel consumption.

6.2 Reasons for the comparison

Different CVT possibilities for helicopter applications have been discussed in section 1.4. The existence of a great number of variator concepts and the lack of reliable information about variable transmission weight and efficiency does not permit to make sound hypotheses on performance of CVTs, which has to be integrated in the helicopter and turboshaft engine models.

Nevertheless, even without knowing weight and efficiency characterizing the CVT that has to be simulated, a valuable comparison between CVT and FRT can still be made. In fact, by employing in simulations the same weight and the same efficiency used to evaluate FRT helicopter performance, it is possible to compare the two variable speed concepts independently from different CVT types. It is clear that the CVT case will present the higher fuel saving: as stated above, it makes it possible for both main rotor and turboshaft engine to operate at their optimal speeds, whereas the FRT can only achieve a single intermediate value between these two. However, if the fixed ratio transmission case presents comparable values of fuel saving, it will emerge that only high efficiency and lightweight CVTs would be worth the research effort. If no efficient CVTs appear to be employable, a research devoted to FPT efficiency improvement at off-design speeds would seem to be the most reasonable choice to achieve fuel consumption reduction. Therefore, the analysis presented here may help choosing one of the two approaches depending on the research project performance goals and the estimated research costs. The two variable speed concepts, the FRT and the CVT, have been tested at their own optimal speeds and then compared to the constant RPM speed case to evaluate fuel consumption reduction.

6.3 CVT Optimal Ω Calculation Scheme

The optimization routine employed for the FRT case is described in section 5.4 and graphically exposed in Figure 5.7; it requires to introduce the engine and helicopter models inside the same optimization loop. In the CVT case, instead, since $\widehat{\Omega}_{MR}$ and $\widehat{\Omega}_{FPT}$ are independent, there is no need to couple the engine and helicopter models, which can be run individually; two separate optimization procedures are thus employed.

Firstly, an optimization routine has to find the $\widehat{\Omega}_{MR}$ minimizing the power load requested to the engine. Subsequently, the power output by this first optimization, P_{load}, is used as the input value for a second optimization loop containing the turboshaft engine model alone. This second routine computes the $\widehat{\Omega}_{FPT}$ which minimizes fuel consumption given a particular ambient condition. The process is illustrated in Figure 6.1.

We have understood that when using a CVT it is possible to operate at both FPT optimal speed and main rotor optimal speed. Before carrying out the simulation analysis outlined in Figure 6.1, let us first focus directly on the two different subsystems, starting from the turboshaft engine.

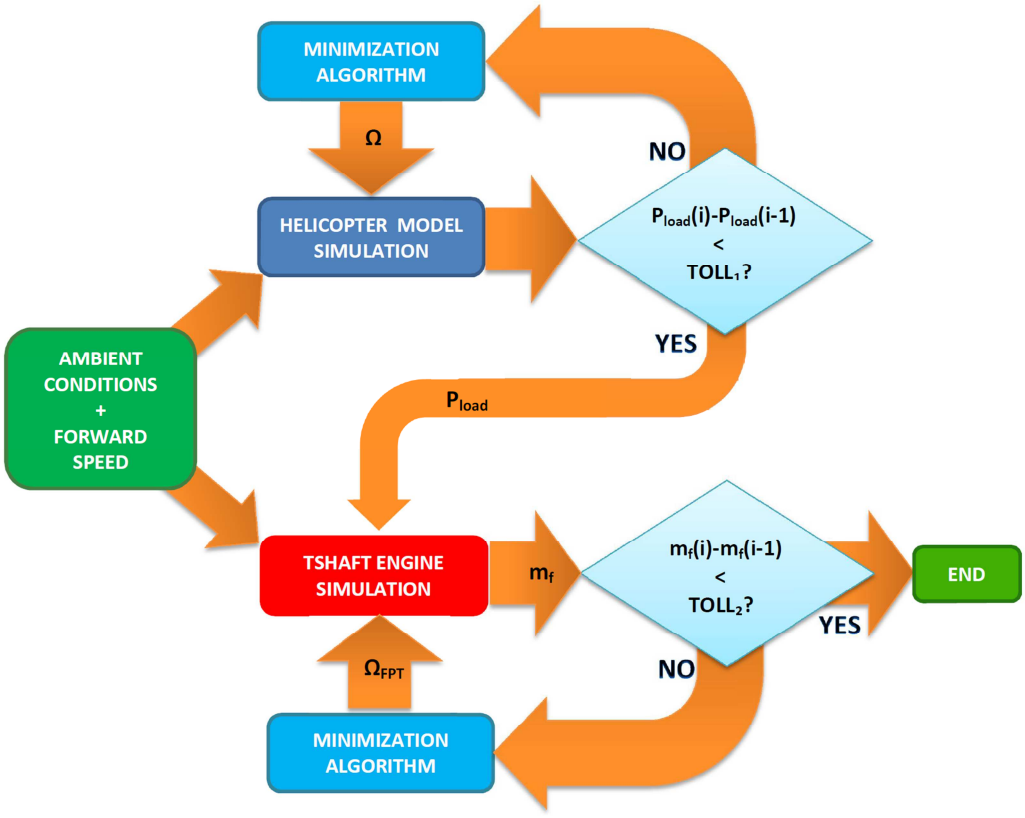

Figure 6.1. Optimal main rotor speed and optimal FPT speed determination process for a continuously variable transmission helicopter.

6.4 Optimal FPT Speed as a Function of Power Load

Since we know that a single optimum FPT speed exists for different power levels, we want to be able to determine the RPM value of the FPT (N_{FPT}) which minimizes SFC, for each assigned value of P_{load}. Using the resulting data of these simulations it is possible to draw, on the map of the various engine components, a new engine running line, which can be defined as engine-optimal.

We perform this study as if we were testing the GE T700 in a laboratory on the ground; we want to isolate the engine from the helicopter and characterize its performance sensitivity to FPT rotational speed. In the next sections, engine performance will be also subjected to the changes in flight conditions (altitude and Mach number) of the helicopter, which are not considered in this section. The condition here simulated at the engine inlet assumes standard air at sea level (*0 m*), with *T=288.15 K* and *Ma=0*. Performance results are exposed in Table 6.1 for two engine running lines: the first is a Constant N_{FPT} Running Line (CNRL), in which N_{FPT} is fixed at 20900 RPM; the second is the Optimized N_{FPT} Running Line (ONRL), in which N_{FPT} is determined using the minimization process. Performance gain achieved through optimization is illustrated in Figure 6.2-Figure 6.3. The improvement is evident, especially at low FPT pressure ratios (corresponding to low power loads), where a reduction in SFC up to 12% can be achieved. Note that in this simulation the relative percentage reductions in fuel flow and SFC are exactly the same, since the comparison between the two running lines is made at the same power P_{load}. In Figure 6.2 it is interesting to note that at 600 kW the design RPM value corresponds to minimum fuel flow; moving away from this value, optimal speed leads to a superlinear decrease in absolute fuel flow.

Constant N_{FPT} Running Line			
N_{FPT} [RPM]	P_{load} [kW]	η_{tot} [%]	SFC [kg/kWh]
20900	1343.8	29.9	0.2795
20900	1199.9	30.0	0.2784
20900	1100.0	29.8	0.2807
20900	1000.0	29.4	0.2845
20900	900.0	28.7	0.2912
20900	800.0	27.9	0.2995
20900	700.0	26.9	0.3101
20900	600.0	25.8	0.3244
20900	500.0	24.3	0.3442
20900	400.0	22.2	0.3769
20900	299.9	19.4	0.4316
20900	200.0	15.5	0.5376
20900	100.0	10.2	0.8206

Optimized N_{FPT} Running Line			
N_{FPT} [RPM]	P_{load} [kW]	η_{tot} [%]	SFC [kg/kWh]
24147	1343.8	31.0	0.2695
23789	1200.0	30.8	0.2709
23545	1100.0	30.5	0.2740
23258	1000.0	29.9	0.2797
22922	900.0	29.0	0.2880
22539	800.0	28.0	0.2978
22125	700.0	27.0	0.3096
20525	599.9	25.8	0.3243
18981	500.0	24.4	0.3428
17452	400.0	22.5	0.3715
16001	300.0	20.1	0.4152
13613	200.0	16.8	0.4969
11911	100.0	11.7	0.7145

Table 6.1. Performance parameters for Constant and Optimized N_{FPT} Running Line simulation.

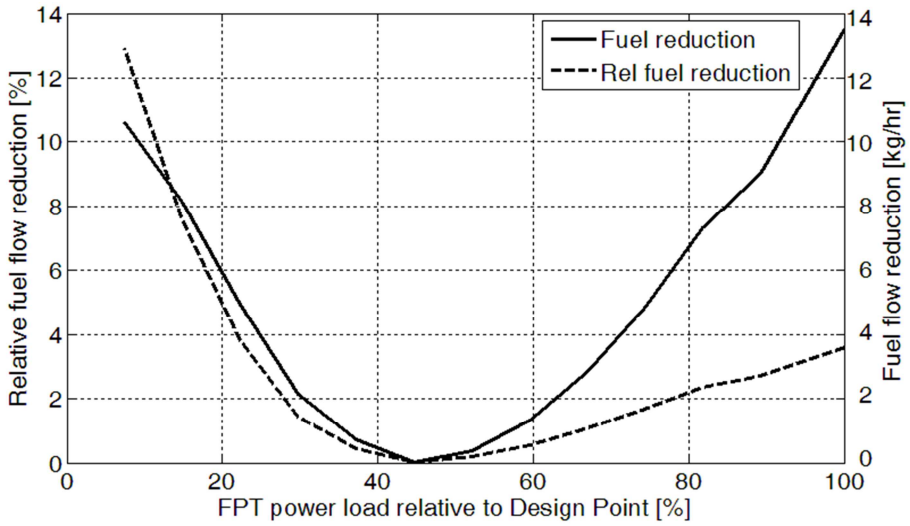

Figure 6.2. Relative fuel flow reduction vs. FPT power load obtained through optimization.

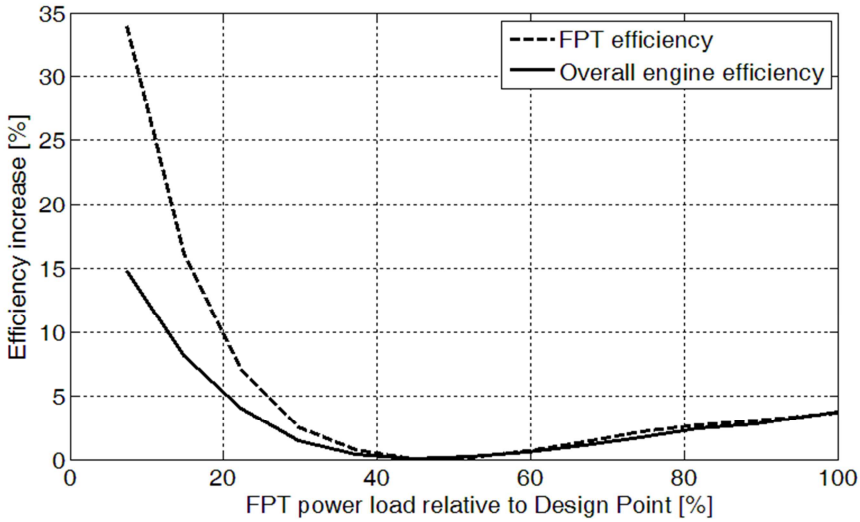

Figure 6.3. Effect of FPT efficiency variation on overall engine efficiency.

The absolute fuel flow reduction is very similar towards either higher or lower power loads. The relative fuel reduction, instead, is considerably greater at low external loads because lower power means also lower fuel consumption; therefore, the ratio between the absolute reduction and fuel flow must increase. Figure 6.3 illustrates how an increase in FPT efficiency is able to positively affect overall engine efficiency. It is interesting to observe that at higher loads a percentage FPT efficiency increase translates directly into an increment in engine efficiency of approximately the same amount. At low power, instead, a reduced impact on overall engine efficiency is encountered. This is mainly due to the reduction in maximum cycle temperature and pressure ratio, parameters to which engine

thermal efficiency is extremely sensitive. In the limit case, a turboshaft engine with infinitesimal external power load still needs some finite fuel to operate; in this limit condition, any FPT efficiency improvement would have no effect on the engine thermal efficiency, which would be tending to zero.

It is important to notice that the engine efficiency improvement is only due to FPT efficiency changes. The other engine components, i.e. compressor, combustor and GGT, do not present significant differences in their respective efficiencies when optimal speed and constant speed operation are compared. This teaches us an important lesson: in a two spool turboshaft engine, a variation in speed at the same power load affects almost exclusively FPT performance; the influence of the new matching conditions on the performance of the other engine components is negligible. This is also demonstrated in Figure 6.4-Figure 6.6, where the two engine running lines, the ONRL and the CNRL, are compared on compressor, GGT and FPT maps. Some observations can be made for each of these component characteristics.

6.4.1 Compressor Map

In accordance with gas turbine theory the ONRL lies almost in the same place of the CNRL. The difference is found to be in the shift of the individual equilibrium points on the same line. This means that N_{FPT} variation very slightly affects compressor stall margin and moves the operating points along the same curve searching for better performance. In the lower N_{corr} region of the map, the compressor is predicted to surge for both the running lines. The reason for this is given by the fact that these particular compressor and GGT cannot be matched under a certain rotational regime. This problem is usually solved in practice by employing variable inlet guide vanes or blow-off valves, whose effects are not included in these simulations. However, these regimes are found only in the starting phase of the engine, so that for the entire helicopter flight conditions considered, a reasonable stall margin is maintained.

6.4.2 GGT map

The observation made above is valid also for the GGT running lines: the ONRL and CNRL lie in almost the same place, and the operating points of the ONRL are moved along the same curve. Since the FPT is choked for most of the operating conditions of the engine, the operating points on the GGT are very close to each other (see section 3.3 for a reminder on operation of two turbine in series).

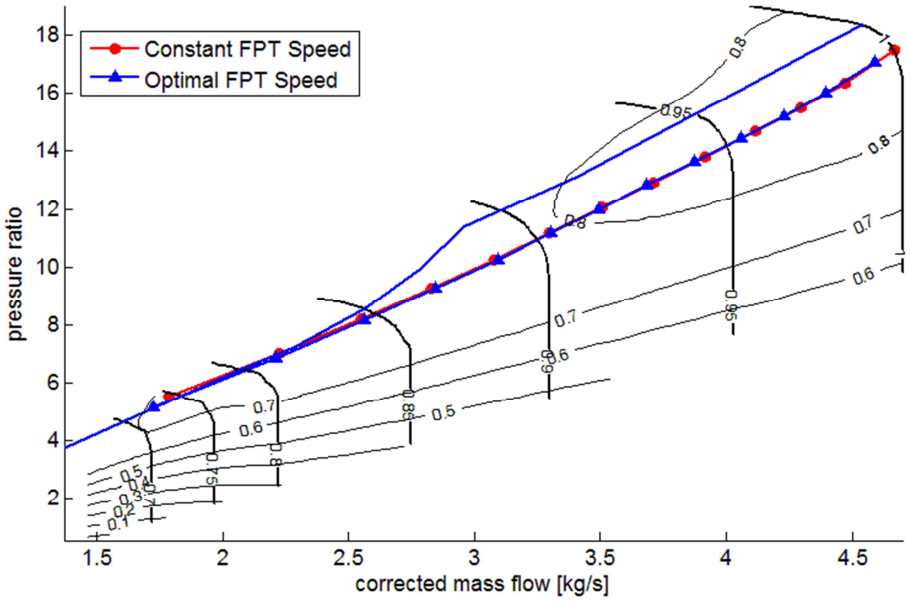

Figure 6.4. Comparison between Optimal N_{FPT} Running Line (ONRL) and Constant N_{FPT} Running Line (CNRL) on compressor characteristic.

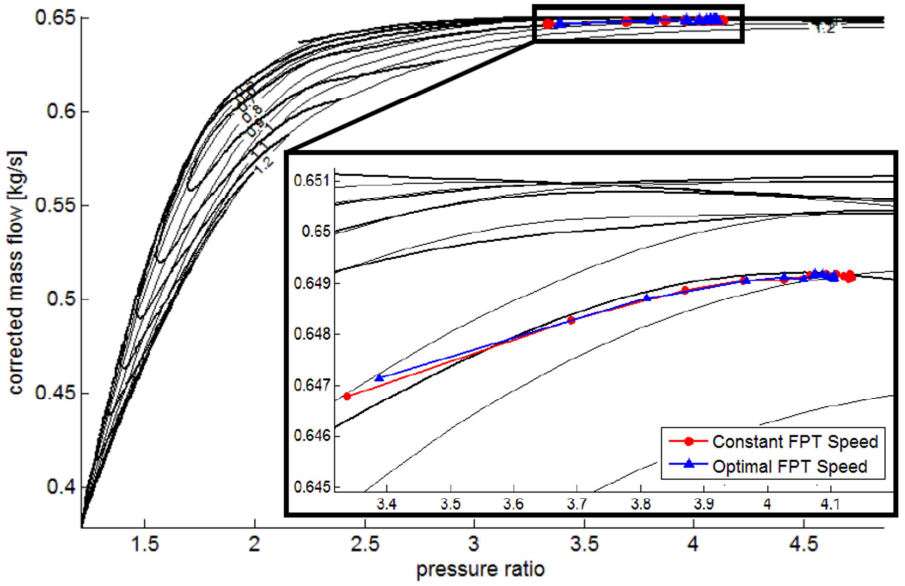

Figure 6.5. Comparison between Optimal N_{FPT} Running Line (ONRL) and Constant N_{FPT} Running Line (CNRL) on GGT characteristic.

6.4.3 FPT map

The most relevant variation in the running line is clearly observed inside the FPT map. The ONRL no longer lies in the same place as the CNRL because the optimization algorithm searches for the best FPT isentropic efficiency. In Figure 6.6 it is evident that the ONRL almost coincides with the FPT peak efficiency line; in fact, in every region of the map (and especially where the values of N_{corr} and

m_{corr} are nearly independent) the reduction of engine SFC is achieved almost exclusively by improving the FPT isentropic efficiency. Given the fact that N_{corr} change is not significantly affecting m_{corr}, there is not a big difference in the engine mass flow and therefore neither a big shift from the original operating points on the other component maps. In conclusion, the FPT running line is mostly affected by the variation in N_{FPT} because the minimization algorithm looks for areas in the map where the FPT efficiency is maximized.

An overview of Figure 6.6 suggests also that, for these particular component maps, the design point RPM of the FPT should be chosen slightly differently. In fact, to achieve maximum performance in design conditions, N_{FPT} should be increased from *20900* to *24147 RPM*. It is expected that, as the power required P_{load} is reduced, a concomitant reduction in N_{FPT} will produce an improvement in the overall efficiency of the engine. Actually, this is what happens in the low pressure ratio region. However, for higher power levels requested, the algorithm moves the minimum SFC points towards higher N_{FPT}, thus suggesting that there is a better design point choice for the engine other than the initial one. In this way the optimization algorithm implemented provides even further information, i.e. it indicates which is the maximum performance that can be reached by a particular engine configuration.

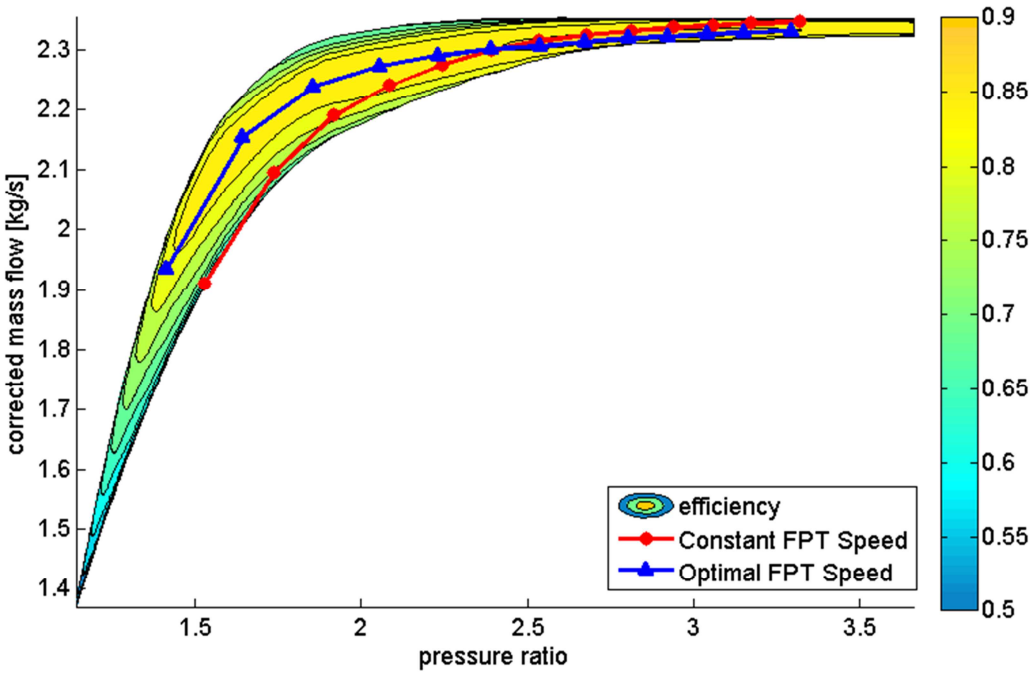

Figure 6.6. Comparison between Optimal N_{FPT} Running Line (ONRL) and Constant N_{FPT} Running Line (CNRL) on FPT characteristic.

6.5 Optimal Main Rotor Speed as a Function of Flight Conditions

The second subsystem to consider is the main rotor alone, since, as we have seen before, a CVT would allow the main rotor to reach its optimal speed independently from engine RPM. To carry out the analysis, the five steady state cases presented in section 5.5 are considered. The same flight conditions are again simulated, along with altitude sweep and gross weight variation, this time considering the main rotor speed optimization alone.

The most interesting output from the analysis is main rotor power. For this reason, a comparison between constant Ω_{MR} operation at *27 rad/s* and $\widehat{\Omega}_{MR}$ is made and the results are given in Table 6.2-Table 6.3. In Table 6.4, the optimal main rotor speed responsible for minimum power is reported.

	Constant $\boldsymbol{\Omega_{MR}}$ Helicopter Power Absorption [kW]				
V [m/s]	**h=0 m W=7527 kg**	**h=2100 m W=7527 kg**	**h=4200 m W=7527 kg**	**h=2100 m W=5443 kg**	**h=2100 m W=9071 kg**
0	1241.2	1315.6	1448.4	930.0	1787.8
10	1057.6	1139.2	1273.4	790.4	1571.2
20	813.2	876.4	995.4	613.4	1225.6
30	712.2	738.4	820.0	549.4	1005.0
40	724.4	717.4	767.0	572.2	934.0
50	828.6	785.4	810.2	668.2	978.8
60	1030.2	940.2	953.6	844.2	1142.4
70	1352.6	1197.8	1452.6	1124.0	1836.2
80	1861.8	1599.6	2527.8	1578.6	3137.4
90	2837.2	2304.4	3617.2	2758.0	4466.0

Table 6.2. Helicopter absorbed power at constant $\boldsymbol{\Omega_{MR}}$ (27 rad/s).

	Optimal $\boldsymbol{\Omega_{MR}}$ Helicopter Power Absorption [kW]				
V [m/s]	**h=0 m W=7527 kg**	**h=2100 m W=7527 kg**	**h=4200 m W=7527 kg**	**h=2100 m W=5443 kg**	**h=2100 m W=9071 kg**
0	1151.6	1270.2	1441.6	847.2	1779
10	959.4	1087.6	1262.8	700.4	1558
20	713	823.6	986.6	521.6	1214
30	615.8	690.4	813.6	458.4	997.6
40	626.6	670	763.6	475.6	930.6
50	719.2	730.4	809.8	555.6	978.6
60	898.6	872.6	949.2	706	1135.8
70	1195.4	1123.2	1209.8	955.8	1430.2
80	1694.6	1542.2	1647.6	1394.8	1925.4
90	2743.4	2300	2402.2	2589.2	2765.6

Table 6.3. Helicopter absorbed power at optimal $\boldsymbol{\Omega_{MR}}$.

	Optimal Ω_{MR}				
V [m/s]	**h=0 m W=7527 kg**	**h=2100 m W=7527 kg**	**h=4200 m W=7527 kg**	**h=2100 m W=5443 kg**	**h=2100 m W=9071 kg**
0	19.56	22.56	25.69	19.16	25.72
10	19.23	21.96	25.29	18.50	25.18
20	20.18	22.16	25.46	19.52	25.30
30	21.12	23.14	25.99	20.42	25.96
40	21.75	23.83	26.49	21.01	26.52
50	22.12	24.29	26.87	21.36	26.91
60	22.49	24.62	27.23	21.75	27.28
70	23.06	25.09	27.61	22.39	27.65
80	23.99	25.82	28.13	23.46	28.16
90	25.49	26.76	28.84	25.47	28.90

Table 6.4. Optimal $\boldsymbol{\Omega_{MR}}$ values.

A similar discussion to the one made in section 5.5.2 can be done; it is seen that for every flight condition the helicopter power at $\widehat{\Omega}_{MR}$ is considerably lower than the constant speed case, except for the high altitude or high weight cases; we therefore deduce that main rotor speed has been designed for the highest C_T values considered in our simulations, where *27 rad/s* appears to be a very good speed choice. However, still some benefits are encountered in these high C_T conditions: in fact, the constant speed case at high forward velocities is again affected by retreating blade stall, which instead is avoided by the optimal speed case: an extension of the operating envelope is achieved.

Figure 6.7-Figure 6.8 illustrate the relative reduction in helicopter power achieved by optimal main rotor angular speed operation, for different altitudes and weights (dashed lines). It is interesting to compare these values to the FRT case, where overall system optimal speed $\widehat{\Omega}$ was calculated as a compromise between main rotor and FPT optimal speed. For this reason, the power reduction obtained using $\widehat{\Omega}$ is also plotted (continuous lines). We see that for the hover condition and till *V<30 m/s* the coupled optimization (FRT) acts as a constraint to main rotor power optimization: in this low *V* region, engine performance is a relevant factor in the overall optimization and forces the rotor speed to higher values with respect to the unconstrained optimization, and thus higher power. Higher values of power in this region lead to lower fuel consumption, because FPT efficiency is increased.

Over *30 m/s*, instead, $\widehat{\Omega}_{MR}$ and $\widehat{\Omega}$ lead to almost the same power level. In this interval, $\widehat{\Omega}_{MR}$ and $\widehat{\Omega}_{FPT}$ are both increasing with *V* and main rotor performance is the leading factor driving the optimization. N.B.: when comparing CVT and FRT cases, equal minimum power does mean equal rotor efficiency, but it does not mean equal engine performance. In fact, the two transmission types are

characterized by different fuel consumption due to a different FPT speed. This will be better shown in the next section, where the FRT and CVT concepts are compared analyzing the different optimal speeds and the different fuel savings.

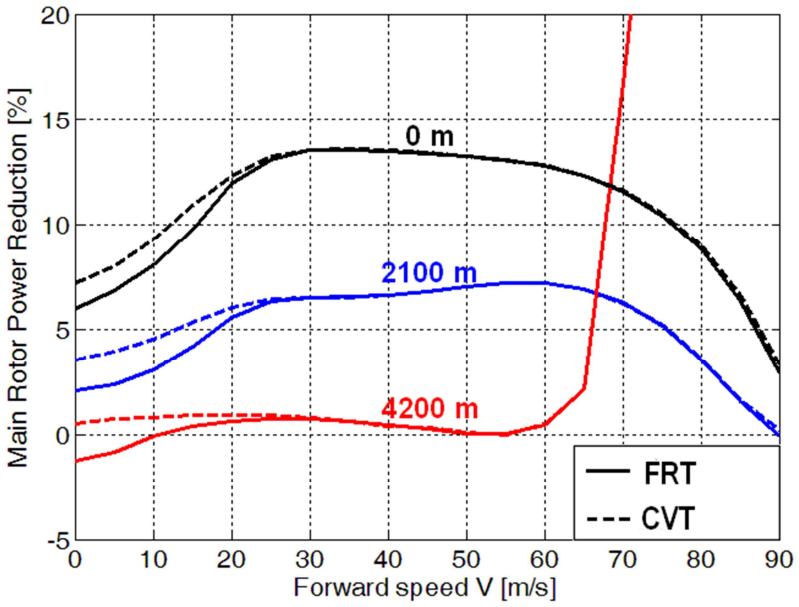

Figure 6.7. Helicopter power reduction at different altitudes achieved grace to $\widehat{\Omega}_{MR}$ (dashed line); for comparison, power reduction at optimal global speed $\widehat{\Omega}$, for the FRT case, is drawn (continuous line).

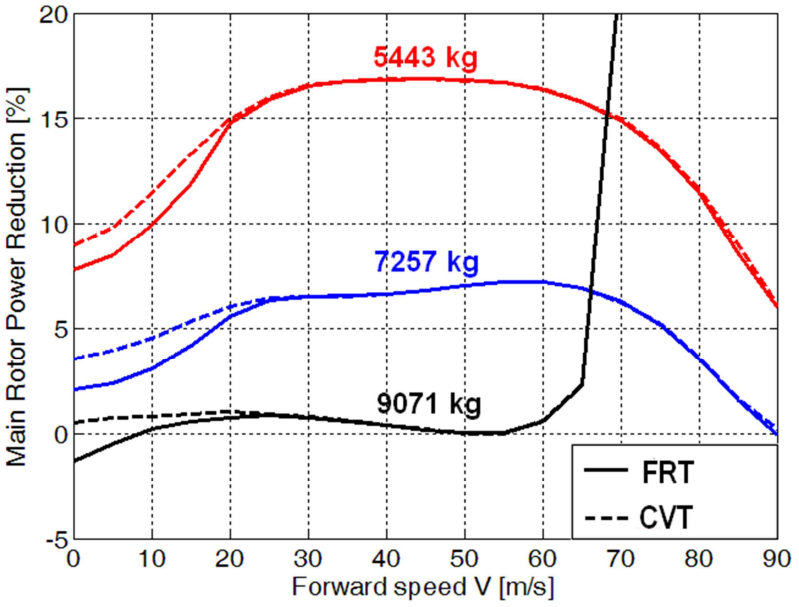

Figure 6.8. Helicopter power reduction at different weights achieved grace to $\widehat{\Omega}_{MR}$ (dashed line); for comparison, power reduction at optimal global speed $\widehat{\Omega}$, for the FRT case, is drawn (continuous line).

6.6 CVT and FRT Performance Comparison

The five steady state conditions presented in section 5.5 are simulated, this time considering the CVT approach. The CVT results are compared with the previous FRT output and the constant Ω (*27 rad/s*) case.

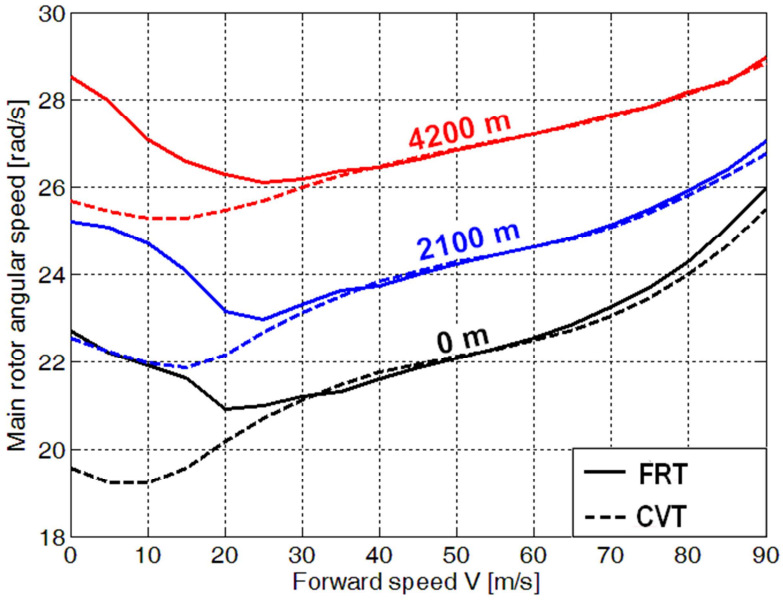

Figure 6.9. Optimal main rotor angular speeds at different altitudes for FRT and CVT cases (*W*=7257 kg).

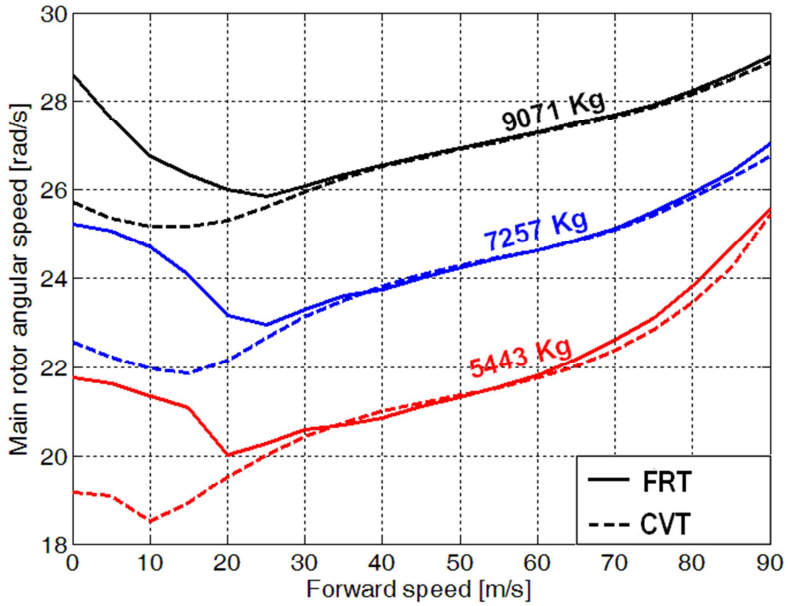

Figure 6.10. Optimal main rotor angular speeds at different helicopter gross weights for FRT and CVT cases (h=2100 m).

In order to calculate fuel consumption, the power output by TCOPTER (in Table 6.3) must be passed to the engine model. An optimization loop in TSHAFT computes the best rotational speed for the particular power level and ambient conditions required. Note that, due to the typical shape of the power curve, for $P<P_{hover}$ there are two different V values corresponding to the same power level (see Figure 5.15-Figure 5.16); instead, engine performance related to these two operating points will be different, because of the different inlet total conditions.

In Figure 6.9-Figure 6.10, the optimal main rotor speed $\widehat{\Omega}_{MR}$ is calculated for both the FRT and the CVT cases at different weights and altitudes. The UH-60 main rotor design speed is 27 rad/s. It can be observed that, at intermediate V values, $\widehat{\Omega}_{MR}$ is found to be lower than the design constant value for both FRT and CVT cases. This happens because of the increase in the blade angle of attack when operating at optimal speed: the optimization indicates that the best strategy is carried out when reducing blade profile power by lowering the rotational speed.

The dashed lines (CVT) can be viewed as the result of an unconstrained optimization on main rotor performance, whereas the continuous lines (FRT) are the result of a main rotor optimization constrained by engine speed linkage. Beyond the 30 m/s condition, there are no big differences between the FRT and CVT cases. This means that in this region main rotor efficiency is affecting overall helicopter performance more than turboshaft engine efficiency. On the other hand, near the hover condition there is a significant difference between the two transmission concepts, stating that FPT efficiency starts playing an important role in the optimization process: minimizing main rotor power is no more equivalent to minimizing fuel consumption.

In Figure 6.11-Figure 6.12 the optimal engine FPT speed is calculated for both the FRT and the CVT cases at different weights and altitudes. The GE T700 design speed is *20900 RPM*. In this case, a significant variation between the CVT and FRT cases is observed for the majority of the flight conditions (maximum discrepancy around 25%). Since the minimum in main rotor absorbed power occurs at intermediate speeds, helicopter operation near hover and at high V values implies high power levels requested to the engine. In these regions the FPT, once let free to seek for its maximum efficiency, reaches considerably higher rotational speeds; in fact, in order to maintain optimal stage incidence angles, the optimal FPT speed increases with increasing power levels. The dashed lines (CVT) can be viewed as the result of an unconstrained optimization on turboshaft engine performance, whereas the continuous lines (FRT) are the result of an engine optimization constrained by main rotor speed linkage.

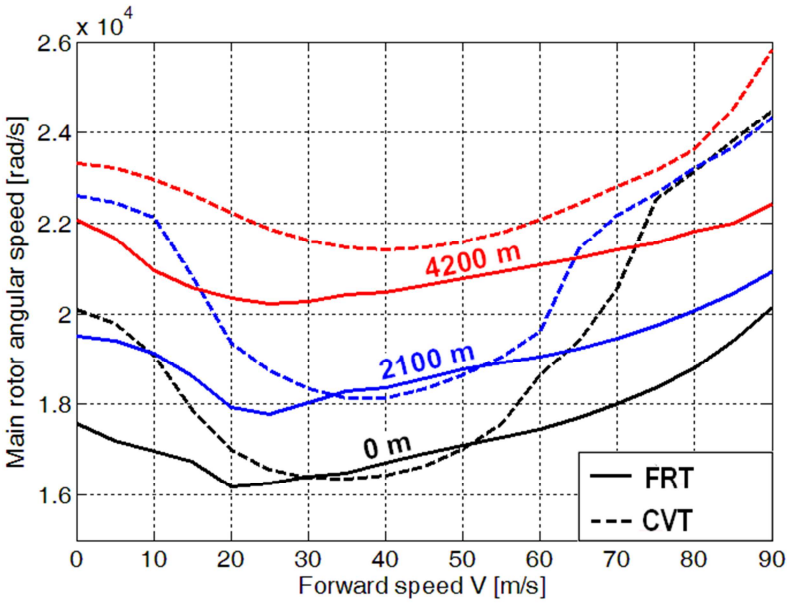

Figure 6.11. Optimal FPT speeds at different altitudes for FRT and CVT cases (*W*=7257 kg).

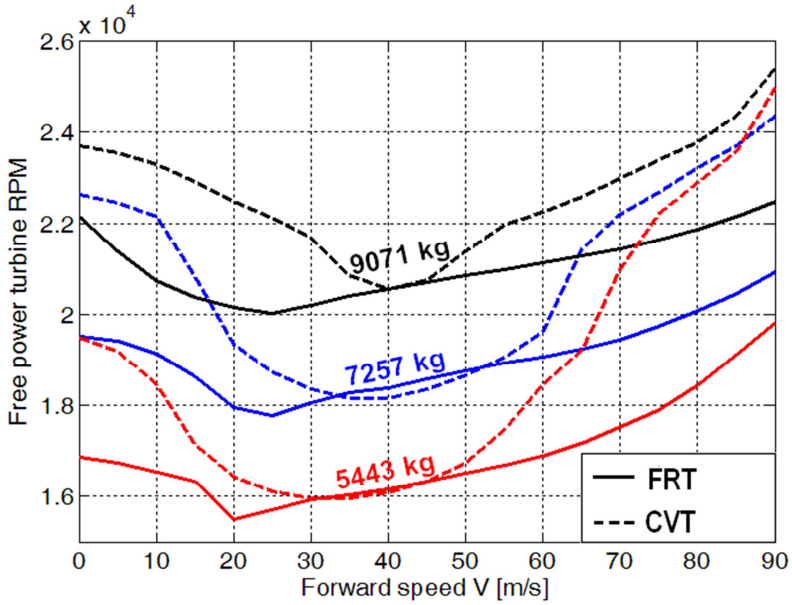

Figure 6.12. Optimal FPT speeds at different helicopter gross weights for FRT and CVT cases (h=2100 m).

In Figure 6.13-Figure 6.17 the most important performance results are presented. The percentages in fuel savings with respect to the constant design speed case (normal helicopter operation) are shown. In addition to the two optimized FRT and CVT cases, another possible design configuration is assessed, which employs a variable speed main rotor with constant speed FPT, at the usual design value of 20900 RPM. The figures represent valuable information clarifying

the different contributions to helicopter performance improvement given by the single subsystems optimization. From the figures below, the following considerations can be derived:

1. For every case considered, both optimal CVT and FRT speeds lead to better results, in terms of fuel consumption, at lower weights and lower altitudes, i.e. at lower C_T. This is mainly due to the fact that optimal operation at high C_T is found to be very close to the design speed conditions. Actually, the farther from the design conditions the more useful the optimization approaches presented. This is true for advancing speeds still far from the blade stall condition.
2. Once a CVT approach is chosen, it is worth to utilize the double optimization method exposed above. From a performance standpoint, it is inefficient to operate the FPT at its constant design speed in every flight condition, whilst the rotor is operating at its optimum. This choice also leads sometimes to a higher fuel consumption than the FRT case, as can be seen in Figure 6.13-Figure 6.17 (red line named CVT, Design N_{FPT}). If, driven by the desire to increase performance, we admit a complication of the helicopter hardware with the introduction of a CVT, we should also complicate the system control software, otherwise much of the gains with respect to the FRT case would be lost. For this reason, in the next part of the section, we will refer to the CVT case as only the double optimization case.
3. In Figure 6.15 and Figure 6.17, both $\widehat{\Omega}$ and $\widehat{\Omega}_{MR}$ produce a beneficial effect at high C_T and high V (beyond 65 m/s) regarding blade stall delay, which ultimately results in an extended helicopter flight envelope. In these operating regions, constant design speed operation is no more viable because of large diffused retreating blade stall. This condition corresponds to a deep increase in main rotor power due to blade drag, which becomes exaggeratedly high that the turboshaft engine is no longer able to afford it; in fact, to provide the high power load, the engine increases the fuel flow and exceeds the maximum cycle temperature permitted (which is left free to exceed the technological limits in the engine model). Variable speed operation, instead, still maintains an affordable fuel consumption and a reasonable turbine inlet temperature. For this reason, the very high fuel savings encountered in this particular case cannot be considered as realistic, since the comparison is made on a trimmed state that is virtually impossible to achieve. However, fuel saving is still useful to be plotted since it demonstrates that at very high

advancing speeds the variable speed rotor is able to trim the helicopter at acceptable power levels, whereas the constant speed rotor is not able to operate properly due to retreating blade stall. The optimization process (in both FRT and CVT cases) avoids retreating blade stall by increasing Ω_{MR} which in turn permits to decrease the blade angle of attack: this can be beneficial until sonic conditions are encountered at the advancing blade tip. The rotor power is maintained at acceptable levels, hence high gains of fuel consumption are displayed by the turboshaft model.

4. The highest fuel consumption reduction achieved by the optimizations (excluding the blade stall regions) is found to be almost 13% at intermediate advancing speeds (low C_P region). It is interesting to observe that this peak is common to both the CVT and FRT cases. Instead, the use of a variable speed main rotor with constant speed FPT prevents from reaching the maximum fuel reduction, stating that at intermediate speeds the FRT is more effective than mere main rotor and engine decoupling; but near cruise and hover conditions, the constant FPT speed approach, compared to FRT, results in better performance.
5. The CVT concept behaves better than the FRT over the entire advancing speed interval, as expected. However, at intermediate speeds the differences between the two approaches are negligible: in fact, the value of $\widehat{\Omega}_{FPT}$ divided by the fixed transmission ratio is close to $\widehat{\Omega}_{MR}$. This can be seen by comparing Figure 6.9 and Figure 6.11 (altitude sweep), and Figure 6.10 and Figure 6.12 (weight sweep). On the contrary, in hover and high speed cruise $\widehat{\Omega}_{MR}$ and $\widehat{\Omega}_{FPT}$ tend to diverge: the FRT has to find the best compromise between the different optimal speeds of the two subsystems. In fact, at high V values $\widehat{\Omega}_{FPT}$ increases more rapidly than $\widehat{\Omega}_{MR}$, since optimal engine operation requires a higher rotational speed with increasing power. Since higher engine power means higher engine mass flow, $\widehat{\Omega}_{FPT}$ has to be increased in order to maintain optimal turbine blade angles with respect to the flow. In addition, when close to hover, $\widehat{\Omega}_{MR}$ and $\widehat{\Omega}_{FPT}$ are even characterized by opposing trends. In fact, from intermediate to low V values the power requested to the engine is increasing, and hence also $\widehat{\Omega}_{FPT}$ increases; on the other hand, $\widehat{\Omega}_{MR}$ decreases to minimize blade profile power. The minimum value of $\widehat{\Omega}_{MR}$ is reached very close to hover, whereas the $\widehat{\Omega}_{FPT}$ minimum is found between the 30-50 m/s interval.
6. Even if the CVT presents better performance, no big differences with the FRT are encountered. For this reason, the efficiency and weight of the CVT

mechanism have to be comparable with current fixed ratio transmission technology, otherwise even a few percentage point variation in these quantities would be able to erase any CVT performance benefit.

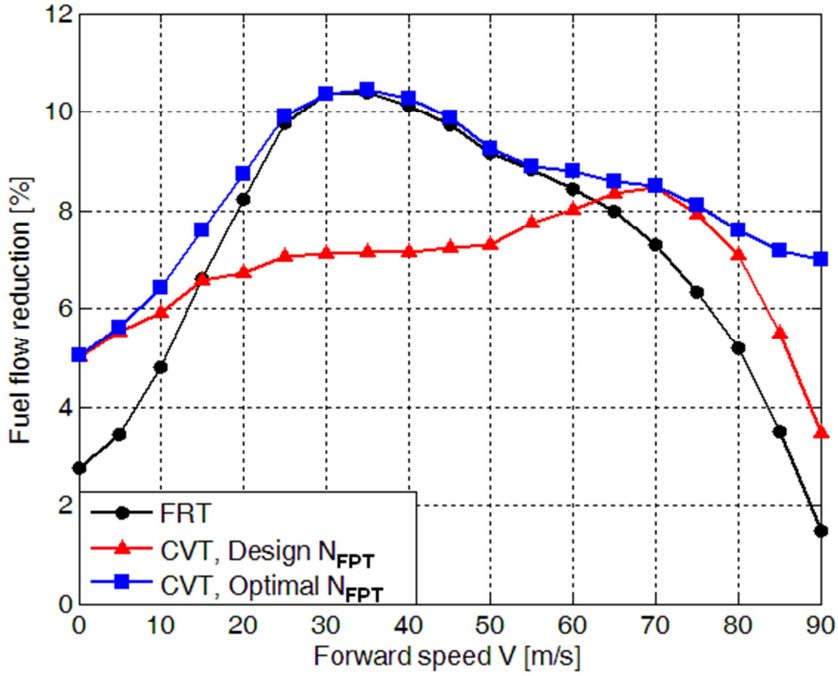

Figure 6.13. Fuel saving comparison for *W*=7257 kg, *h*=0 m.

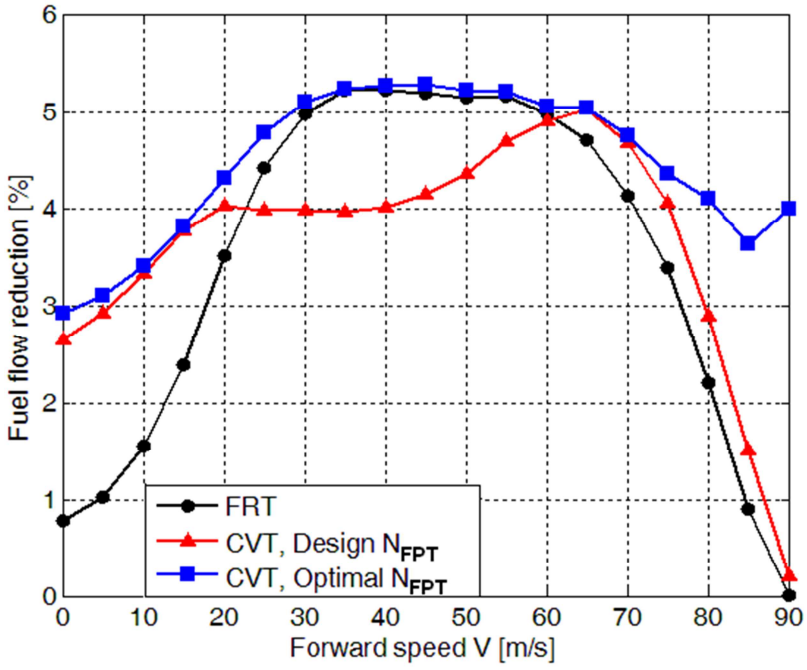

Figure 6.14. Fuel saving comparison for *W*=7257 kg, *h*=2100 m.

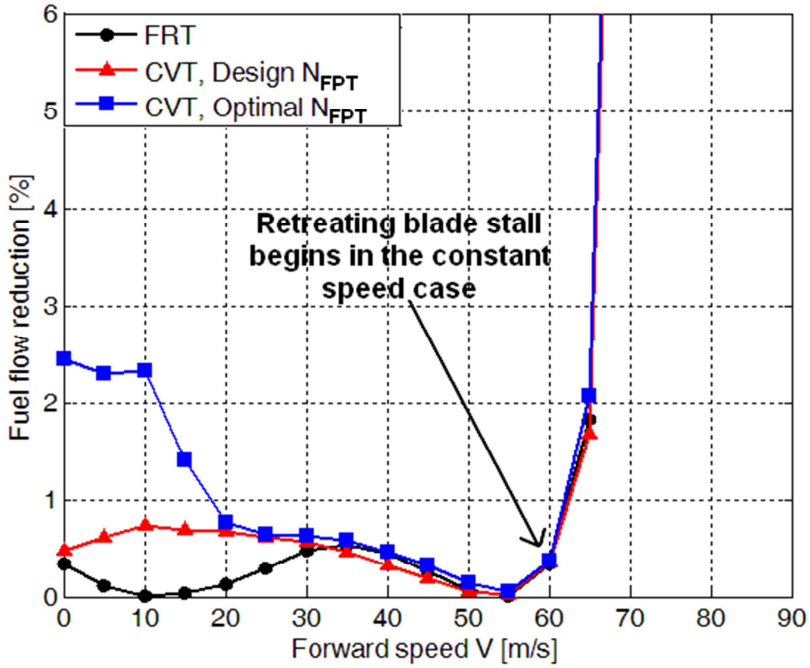

Figure 6.15. Fuel saving comparison for *W*=7257 kg, *h*=4200 m.

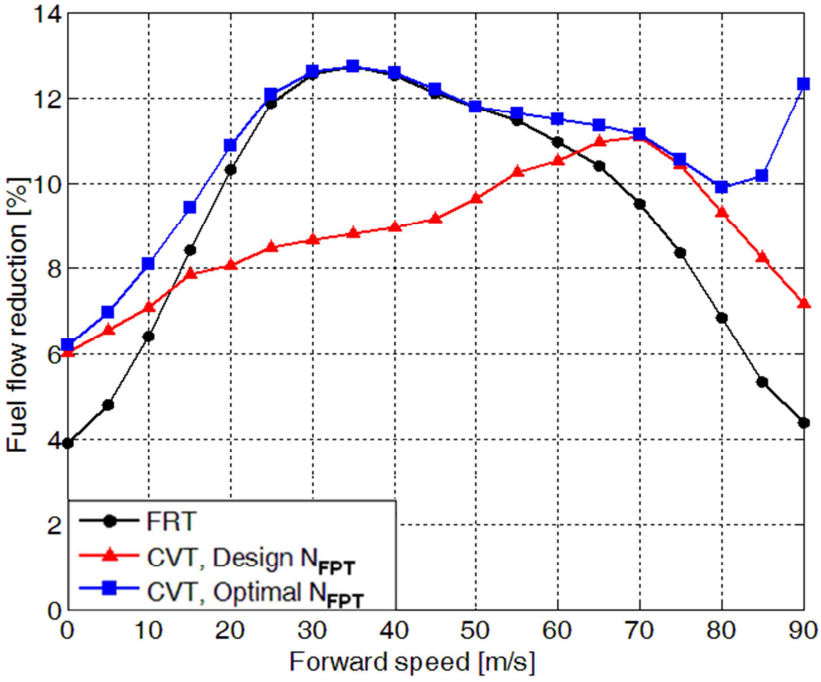

Figure 6.16. Fuel saving comparison for *W*=5443 kg, *h*=2100 m.

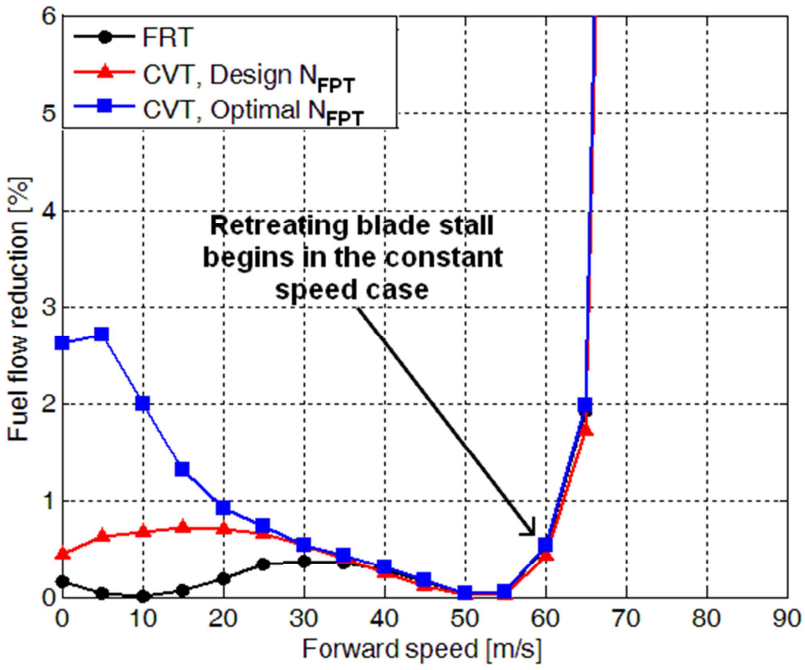

Figure 6.17. Fuel saving comparison for W=9071 kg, h=2590m.

6.7 Final Considerations

Two different approaches have been analyzed, the FRT and CVT concepts, and their performance results have been compared. Considerable reductions in fuel consumption (almost 13% maximum) have been reported for both FRT and CVT cases with respect to standard constant speed rotor operation. At high C_T values, fuel saving is reduced because optimal rotor speed is found to be very close to the design constant speed value.

It was found that FRT and CVT fuel savings are comparable for intermediate advancing speeds, but tend to diverge in the hover and high advancing speed regions, where CVT clearly outperforms FRT, with a maximum of 8% better fuel reduction. However, the CVT concept can represent a valuable alternative to FRTs only if the CVT mechanism is able to preserve state of the art FRT weight and efficiency. In fact, especially at high C_T values, a few percentage points drop in transmission efficiency or even additional weight would imply a higher fuel consumption than with the constant speed case. Since a large part of the helicopter operational time is usually spent in the hover and cruise conditions, CVT represents the best theoretical choice for VSRs; alas, it cannot be employed until a reliable, efficient and inexpensive CVT design will comply with rotorcraft industry requirements.

The FRT concept, instead, seems to be a more feasible way to reduce fuel consumption, especially for helicopter missions characterized by an extended operating time in the intermediate advancing speed region (surveillance, taxiing, sightseeing, etc.). Unfortunately, compared to the CVT, the FRT is not performing well in hover and high speed forward flight, which are the conditions of major interest for a helicopter designer. At this point, we should wonder: is there a way to improve the FRT concept? We will try to address this question in the next chapter.

6.8 References

[1] G. A. Misté and E. Benini, *Performance of a Turboshaft Engine for Helicopter Applications Operating at Variable Shaft Speed*, ASME Gas Turbine India Conference 2012 Proceedings, Mumbai.

[2] G. A. Misté, A. Garavello, E. Benini, and M. Gonzalez-Alcoy, *A New Methodology for Determining the Optimal Rotational Speed of a Variable RPM Main Rotor/Turboshaft Engine System*, Proceedings of the American Helicopter Society 69th Annual Forum, Phoenix, Arizona, USA, May 2013.

[3] G. A. Misté, E. Benini, *Turboshaft Engine Performance Comparison Between CVT and Fixed Ratio Transmission for a Variable Speed Rotor*, Proceedings of the 39th European Rotorcraft Forum (ERF), Moscow, Russia, September 2013.

Chapter 7

Improving the VSR Concept

7.1 VSR Improvement Concepts

In the previous chapter we have dealt with the advantages given by the utilization of a CVT. Variable speed transmission research is a really fascinating research topic, whose application is not only limited to the rotorcraft field. They could be very useful in a lot of technical fields: automotive, machinery, energy production. Wherever there is a need for a speed reduction, CVTs could let motors perform at their maximum efficiency, independently from the operational conditions. It is therefore a potential breakthrough technology, and it is surely worth to invest in this research field. From magnetic gears to electromechanical power split devices, there still is a great margin of improvement of the current variator technologies, which at the moment are not reliable, do not permit to withstand high values of torque, and are really inefficient if compared to well-designed fixed ratio transmissions. However, we have still many years ahead before the introduction of a CVT in rotorcrafts. We have seen that the CVT, in order to achieve performance benefits, must be characterized by efficiency and weight comparable to existing FRT. No such technology exists at the moment.

Following this, in the present chapter we will focus on the possibility to improve the VSR concept assuming to preserve the traditional FRT. There are many possible ways to achieve this; we will quickly have a look at three different possibilities.

7.2 Coaxial Rotors

Coaxial rotors have been among the first designs employed in the early development of rotorcrafts at the beginning of the 20th century. In fact the double counter-rotating rotor solution was the most intuitive way to balance the rotor torque on early vertical flying machines. However, in the 1940's, the traditional single rotor configuration was established mainly grace to Igor Sikorsky, who solved the torque balance problem by adding a tail rotor in the aft part of the

helicopter. All over the world this new type of VTOL machine was so successful that any other type of rotorcraft configuration (e.g. autogyros and coaxial helicopters) was relegated to a marginal industry production. There was a notable exception in Russia, where Nikolai Kamov pursued a successful coaxial helicopter design, which instead had been abandoned by the western countries. From the second half of the XX century till today, Russia has been the major producer of coaxial rotors, for even military or civil uses.

In the recent years, particular attention has been given by the rotorcraft community to coaxial rotors. Leader of this particular research field has been the Sikorsky Corporation, which from the beginning of the 70's started a new project on a coaxial rotor helicopter (XH59A) which led to the ABC^{TM} (Advanced Blade Concept) technology. The project was abandoned mainly due to excessive vibrational issues, but in the latest years it has been revived, with the onset of two important technology demonstrators: the X2TD [1], which developed new AVC systems to reduce vibrations [2] and its military version, the S97 Rider, which is planned to be tested in 2015 [3]. This potential breakthrough technology is based on a rigid (in flap and lag), counter-rotating, coaxial rotor system in which the retreating blades are offloaded at high speeds [1] (see Figure 7.1). One of the big limiting factors related to increasing the maximum advancing speed of traditional single rotor helicopters is given mainly by retreating blade stall, as we have seen in the previous chapters. It is much more relevant than compressibility effects due to a tip speed near *Ma=1,* because it usually appears before reaching the drag divergence Mach number. By offloading the retreating blades, the lift potential of the advancing blades can be more optimally exploited, and the high drag and torque generated by the retreating blades is significantly reduced. This can be clearly seen in Figure 7.1: on the retreating blade of a traditional helicopter, lift dissymmetry leads to additional induced drag and negative lift in the reverse flow zone near to the root; this zone becomes bigger as the forward speed is increased, till the onset of stall on a wide fraction of the rotor disk forbids stable trim conditions. In the coaxial rotor, instead, the retreating blades of both rotors produce almost no lift, minimizing induced drag.

Another important feature of the X2 technology is given by the possibility, at high speeds, to schedule a reduction in main rotor speed in order to enter in a "semi-autorotative" state to maximize rotor efficiency and reduce its absorbed power [1]. We see how rotational speed variation is implemented in this extremely innovative compound helicopter; we can therefore state that the X2TD is a rotorcraft successfully employing a VSR.

However, this particular “semi-autorotative” state needs an external force other than the rotor to maintain the high forward speed; in the X2TD this duty is accomplished by a rear propeller. In fact, an aft tilt of the rotor disk increases the autorotative state of the rotor, reducing rotor power requirements and increasing its efficiency, but it also increases the propulsive force that must be delivered by the propeller. Even in this case we have a choice of the optimal speed of the rotor: for a given operating condition there will be a particular rotational speed and rotorcraft attitude which minimize the total power consumed by the overall system; there will also be an optimal power split between coaxial rotor and propeller, to take into account in performance optimization.

In conclusion, the possibility to offload the retreating blade, without penalizing the balance of the rotorcraft, permits to increase rotor efficiency. It is sure that this type of technology will achieve higher advancing speeds with respect to conventional helicopters. However, it is still to be ascertained whether fuel consumption can be positively affected. Only a deeper study which integrates engine, coaxial rotor, and propeller models, compared to a helicopter of the same weight, could give us an answer.

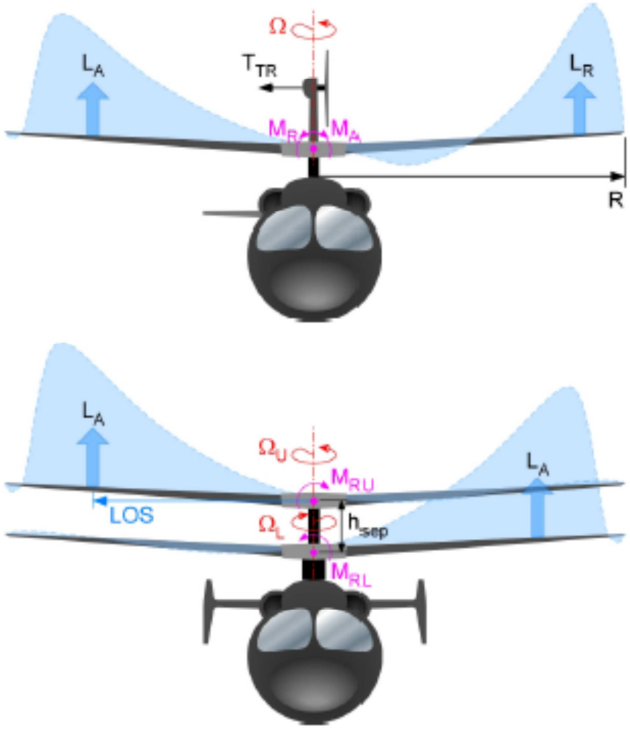

Figure 7.1. Comparison between traditional helicopter and coaxial rotor operation (from Bagai [1]).

7.3 Main Rotor Redesign

Main rotor blades are usually designed for a particular fixed speed. Thus, it makes sense to investigate the possibility to improve main rotor efficiency (and hopefully fuel saving) by means of an appropriate redesign of the main rotor blades, which must take into consideration the variable RPM capability. An optimization framework could be applied to a multi-objective problem regarding the minimization of fuel consumption contemporarily in hover and forward flight conditions, for different values of the coefficient of thrust.

The blade redesign process should be carried out maintaining a fixed rotor radius, otherwise the optimization process would tend to increase it indefinitely: in fact, for a specific value of thrust, a bigger radius is characterized by a reduced induced velocity (and thus power). The optimization framework suggested is able to perform blade shape modifications in terms of chord, twist and tip sweep, optimizing their distributions, as can be seen in Fig. 1. The possibility to assign different airfoil shapes at different sections of the blade should be also considered.

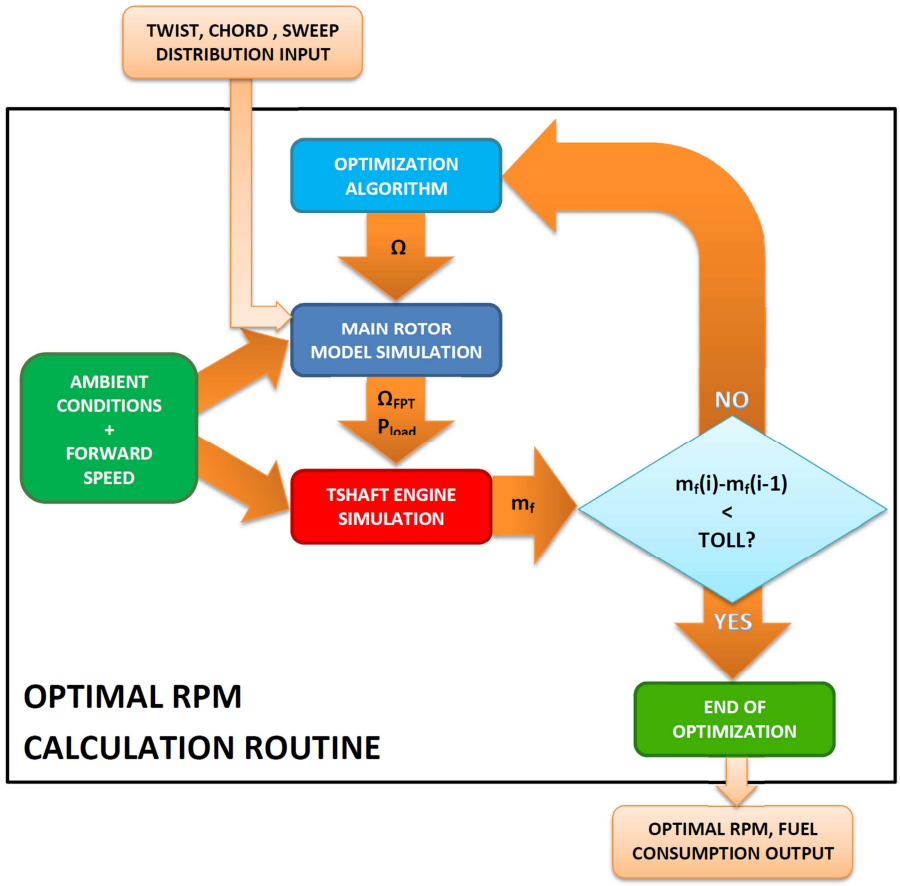

Figure 7.2. A suitable optimization process for main rotor blade redesign.

Figure 7.3. Blade shape optimization study by Massaro [5].

The design optimization process works as depicted in Figure 7.2: the optimization algorithm supplies main rotor twist, chord and sweep distributions to the optimal RPM calculation routine, which in turn outputs the multivariate objective function, i.e. fuel consumption related to the different flight conditions considered. Different configurations should be tested and the best compromise between hover and forward flight could be chosen by the designer. Since the problem is multi-variate and multi-objective by nature, a genetic optimization algorithm (or similar) is suggested, since the variable research space is very large and irregular. A good example of such optimization, without considering variable speed, is given in a paper of Massaro et al. [5]. The result of his optimization (given here as an example of the methodology), starting from a simple rectangular blade, is given in Figure 7.3.

Unfortunately, the helicopter model implemented in TCOPTER cannot be used to perform such an optimization. Even though it can be used for preliminary main rotor design considerations, the model described in Chapter 4 does not capture some important phenomena extremely important in the optimization process. In fact, BEMT is able to predict overall power performance within an acceptable grade of accuracy imposing a prescribed inflow and prescribed tip loss. Whenever we are trying to make a fine-tune optimization of the blade, these models are too inaccurate to capture small variations in power, which are strongly dependent on 3D flow effects. Only an upgrade to more complex models, employing panel methods or other more advanced vortex techniques, would be able to correctly capture the physics beyond the optimization. Computational fluid dynamics (CFD), due to its inherent computational cost, may be used only in the last phase of the optimization, in an advanced stage of the design, or even as a verification of the model output.

7.4 FPT Redesign

Another possible way to tackle the problem of optimizing the main rotor-turboshaft engine system is to define a hierarchy between the two subsystems. Let us assume that our objective is to maximize main rotor performance. The benefits related to optimal main rotor operation may be eventually cancelled by strong deviations from FPT design speed, which lead to higher turbine losses and thus higher fuel consumption. In fact, when FPT speed is far from the design value, the blade incidence angles are far from the optimal values and this implies an increment in blade profile losses. A possible way to overcome this problem is given by an appropriate redesign and optimization of the FPT stages, in order to decrease the stage efficiency sensitivity to RPM variation.

Previous studies on this subject can be found in literature; the work carried out by D'Angelo [6] is the first theoretical analysis upon the feasibility of a wide speed range turboshaft. Recent activities at the NASA Glenn Research Center are also pointed towards this objective: with the aim of assessing the feasibility of a variable speed tilt-rotor concept, Welch et al. [7] studied the redesign of the FPT in order to obtain a good performance on the entire RPM interval, from 100% (take off) to 54% (cruise). The new turbine design was characterized by high work factors in the cruise condition and wide incidence angle variations in vanes and blades among its entire operating range. Other related works from NASA can be found in Refs. [8],[9],[10],[11].

It is quite clear that turbine design is a long and iterative process, which cannot be resolved in a few simple steps. Simulating turbine off design performance is a challenging task, especially because it involves a number of different blade loss mechanisms that are still not completely understood. However, in this section we will try to understand if, by using some simplifying assumptions, it is possible to gather some information related to good variable speed turbine design. The first step of this process consists in obtaining a tool able to estimate turbine efficiency.

7.4.1 TDES: a Mean-Line Turbine Stage Performance Code

TSHAFT, the gas turbine simulation code exposed in Chapter 2, is a software able to perform the matching calculations of the different components inside a gas turbine engine. However, it needs the different component maps in order to predict engine behavior. In this section, a code which simulates only the axial

turbine component will be described. The output given by this code can be used to build a turbine component map to be used inside TSHAFT.

In the preliminary design phase of axial turbines, 1D mean-line analysis is extensively used in the industry to create a solid base for subsequent design optimizations, which usually employ more complex 2D-3D analyses and CFD viscous analyses. This phase is extremely important to obtain an initial sound design, and to decrease the time effort in the subsequent design phases [12]. For this reason, in order to compare different FPT designs, TDES, a mean-line analysis tool, has been implemented. The code is able to predict turbine single stage efficiency related to different designs by using empirical loss correlation models proposed by Craig and Cox [13]; some additional correlations are introduced to increase the accuracy in incidence loss calculations, following suggestions by Moustapha [14] and Bertini et al. [12].

TDES is capable of affording either subsonic or supersonic stage exit flow and performs the stage stacking by matching the different stages. It accepts the thermodynamic boundary conditions and the basic design geometry of the stages as an input (blade metal angles, solidities, duct diameters, etc.) and outputs turbine specific work, efficiency, pressure ratio, and corrected mass flow.

Each single blade row can be completely resolved by knowing the total conditions at the inlet along with the outlet pressure; this last parameter is preferred to the mass flow parameter, since it is able to give a more quick and reliable information regarding the choking conditions.

In a stator row, knowledge of the exit pressure makes it possible to calculate the outlet flow speed, initially assuming conservation of both total temperature and total pressure along the passage. If the first comes directly from the conservation of energy, the second assumption is equal to assuming isentropic flow, clearly unrealizable in practice. This exit total pressure value is needed only to start an iterating process using a fixed point numerical method, necessary to calculate the exit flow speed, which in turns is the essential input for calculating blade row losses. Along with the losses, the empirical model predicts also the angle flow deviation with respect to the blade metal angles. Once these values are known, the estimate on the exit total pressure can be refined until a certain tolerance is reached.

In a rotor row, the single difference from stators is given by the fact that the quantity conserved along the passage is rothalpy, instead of enthalpy (and hence total temperature). In axial turbomachinery, radial variations between the inlet and

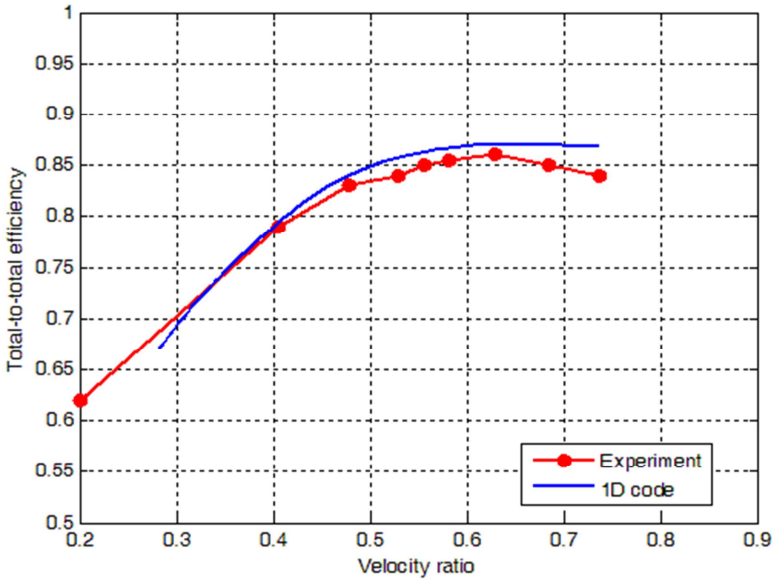

Figure 7.4. Validation of the TDES code on single stage A (data found in [15]).

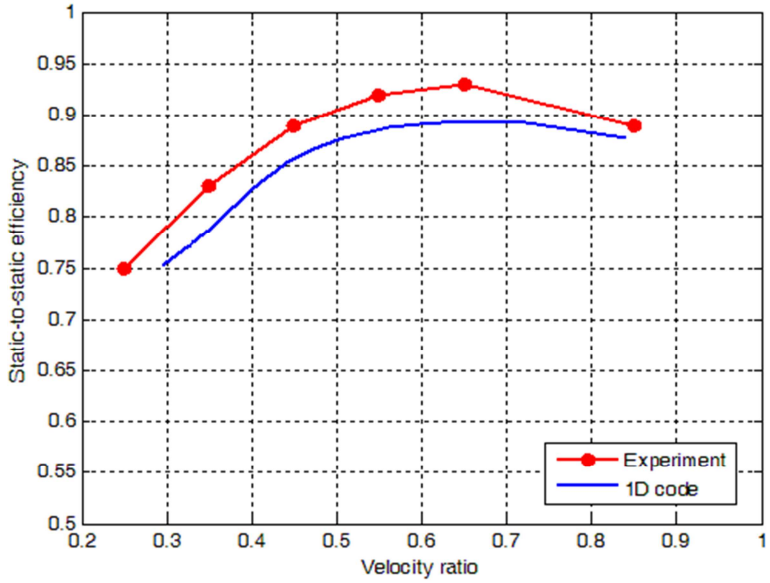

Figure 7.5. Validation of the TDES code on single stage B (data found in [15]).

outlet of a stage are often negligible, so this assumption is translated in the simple conservation of the relative total temperature.

Each row has to solve an iterative scheme which has to be treated with care since it must be able to switch between the subsonic and the choked regimes, that are characterized by a different modeling of blade losses.

In order to perform the stage stacking a nonlinear system of the type ***f(x)=0***, which can be solved in matrix form, is set. The values of static pressure between the successive blade rows are the independent variables of the system (***x***), and the

differences in mass flow between each row is the vector function to be set to zero, in order to preserve continuity. It is clear that the code is composed of a system of nonlinear equations with inside more iteration loops which all have to achieve convergence.

A quite satisfactory validation of TDES has been carried out on two different cascade geometries found in [15], each composed of a single rotor and a single stator. The results of the validation against experimental tests are exposed in Figure 7.4-Figure 7.5.

7.4.2 FPT Design Optimization Methodology

Now that an axial turbine performance code is available, it is time to introduce an optimization procedure able to perform a preliminary redesign of the FPT turbine stages taking into account the RPM variability. First of all, it is important to define the design variables that are to be changed with respect to the original FPT baseline design. Among the most significant parameters in a turbine stage there are the blade metal angles and solidities; these are therefore the parameters chosen to be varied by the optimizer. The remaining input variables are fixed in order to respect geometrical and structural constraints related to the original design or, as in the case of the stagger angle, are chosen using recommendations from literature [16]. In Table 7.1 the different input and output variables managed by the TDES code are reported for clarity.

Design Input Variables	Fixed Input	Output
Blade metal angles	Number of blades	Specific work
Blade solidities	Stagger angles	Efficiency
	Duct dimensions	Pressure ratio
	Hub-Tip ratios	Corrected mass flow

Table 7.1 Single cascade input and output variables in the TDES code for the design optimization.

The optimization procedure is structured as outlined in Figure 7.6. The optimizer gives initial values for the design input variables related to each stator/rotor cascade composing the turbine. In the GE T700 case, there are two stages, therefore four cascades leading to 11 free design input variables[§]. The TSHAFT model is run using as external load parameters the optimal RPM and power calculated by the main rotor model. The values of total pressure and total

[§] The inlet angle at the first stage is assumed to be zero; it is an arbitrary assumption, since the previous gas generator turbine may leave a swirl component inside the flow.

temperature at the inlet of the FPT are passed to TDES, which in turn is able to compute the FPT performance data in terms of work, efficiency and mass flow. The TSHAFT matching procedure to calculate the engine fuel consumption thus uses TDES as a subroutine in its iterative process. Fuel flow is passed back to the optimizer and represents the objective function to be minimized.

The insertion of the TDES model inside TSHAFT seems to be quite "academic", and it sure does not appear a practical choice. In fact, the resulting optimization routine is characterized by several nested iteration loops and nonlinear systems. Unfortunately, if a reliable prediction of few percentage points in fuel consumption is needed, the utilization of such routine is mandatory; in fact, a change in FPT performance influences all the engine matching parameters, leading to different FPT inlet conditions.

The optimization procedure chosen can be multi-objective, and it is executed for more than one flight condition, in order to let the designer decide the best compromise in consumption between different operating points. For the GE T700 case, three points have been chosen: hover, design cruise and best endurance condition. The algorithm that is suggested to be used in the optimization process is a genetic algorithm; other choices can be made, but it is strongly recommended to use global derivative-free optimization algorithms.

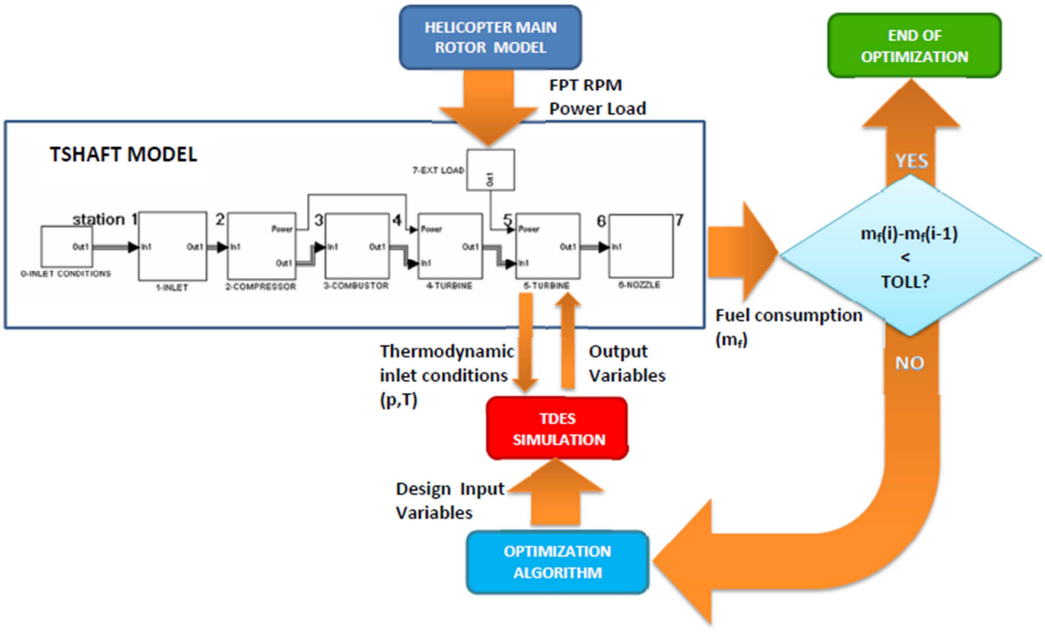

Figure 7.6. FPT redesign optimization procedure.

7.4.3 GE T700 FPT Mean-line Redesign Study

Before applying the optimization of section 7.4.2 to the T700 case, it is important to have a good starting choice for the baseline FPT configuration. Since not all the data were known to build the baseline configuration, several adjustments to the design input variables have been made in order to obtain a turbine design matching the experimental data of the engine. A reverse-engineering study has been carried out using the few design data available in the open literature. The meridional section of the turbine duct, taken from [17], has been used to fix the relative dimensions between hub and shroud; the absolute value of these dimensions has been derived from the turbine exhaust area computed using the design air mass flow in TSHAFT. The most difficult challenge has been encountered in the estimation of the different blade metal angles; this task has been accomplished by means of an error minimization with respect to the FPT performance data calculated with TSHAFT. The procedure employed consisted in a real optimization in which the functions to minimize were the errors in power output and air mass flow. The procedure involves much less calculations with respect to that discussed in section 7.4.2: in fact, the inlet total conditions, this time, can be considered fixed and belonging to the T700 design point.

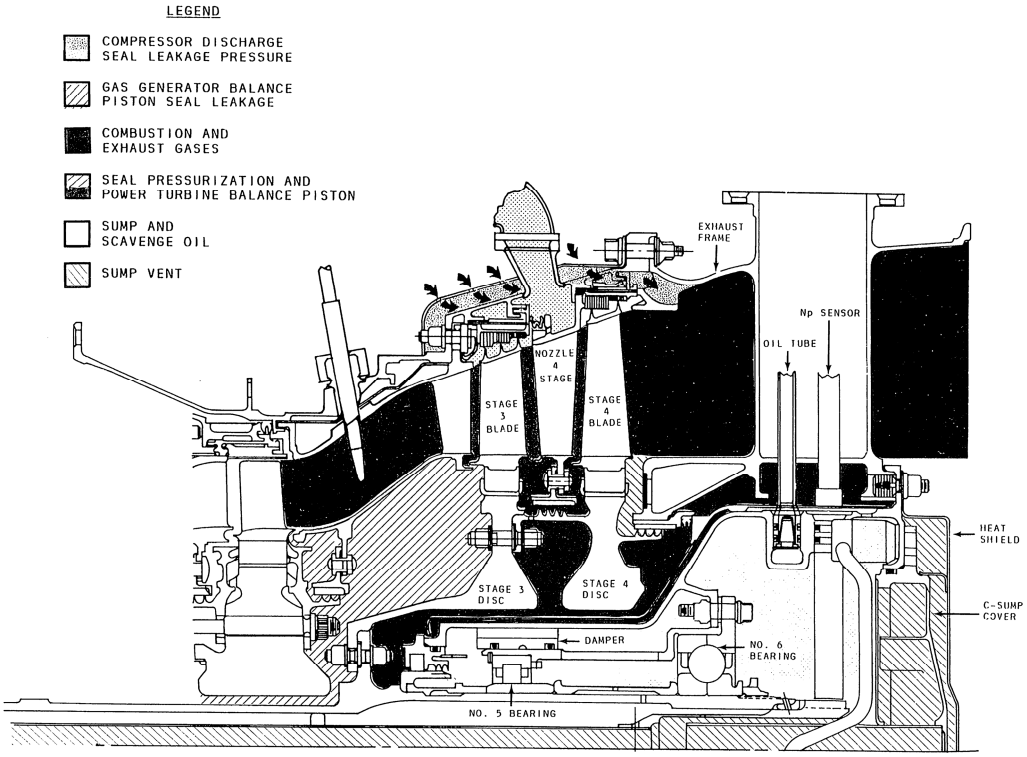

Figure 7.7. Meridional section of the GE T700 power turbine [17].

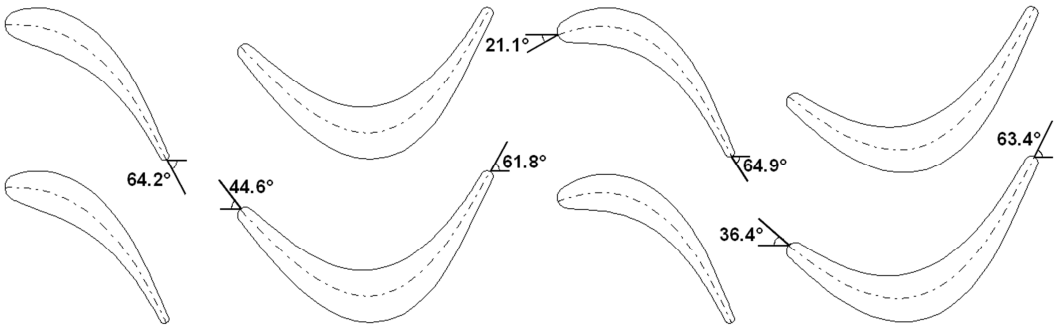

Figure 7.8. Blade angles found through T700 performance error minimization.

The blade angles adjustment has been carried out with a genetic algorithm; the individual configuration which was found closer to the T700 design performance is illustrated in Figure 7.8, where an indicative representation of the mean-line section of the turbine stages is given. Note that a considerable flow turning is present inside the rotor, especially in the first stage; this is indicative of high values of the work coefficient, which is quite common in aeronautical applications[§]. It is clear that there is no unique solution to this optimization problem; therefore, the mean-line blade angles obtained represent just one of the possible design solutions able to achieve the T700 design performance objective of the minimization.

Once the mean-line geometry of the turbine was selected, several TDES simulations were run in different off design conditions, at different corrected mass flows and pressure ratios: these data have been organized and tabulated to create a map of the turbine to be used in TSHAFT simulations.

The new turbine map has been inserted inside the GE T700 engine model and a new comparison with experimental results from Table 5.3, and the previous rescaled map, is made in Figure 7.9. This figure can be also viewed as an additional validation to the TSHAFT and TDES models. Among all, fuel consumption is the most interesting variable to be used as a comparison with experimental tests: a good agreement is reported between this methodology and the experiments.

The baseline configuration obtained in this way can serve as a benchmark for the optimization process. The optimization routine described in section 7.4.2 was run in the two most interesting operating points, hover and cruise forward flight

[§] In aeronautical turbines, the increase in the stage work coefficient is chosen to minimize the number of stages: this allows for a reduction in weight and volume of the engine.

(80 m/s), at an altitude of 2100 m. The values of main rotor power and engine rotational speed can be derived respectively from Table 6.3 (half of the power, since the UH-60 is a twin engine helicopter) and Table 6.4 (multiplying by the transmission ratio).

Unfortunately, the optimization process was not successful, so that it is not possible to say whether some specific design considerations could be derived from the present analysis. In fact, the reason for the optimization failure is numeric: it is not due to non-feasible designs, which are discarded artificially assigning a high value of the objective function; it is due to the TDES insertion inside TSHAFT. In fact, when the latter is seeking for the zeros of the matching nonlinear system, it can try out-of-map values of pressure ratio and corrected mass flow which make TDES crash. This did not happen with a map in the form of a look-up table; in fact, when the algorithm (usually at the starting point of the iterations) requests an out-of-map evaluation, the look-up table allows for extrapolation. The present numerical problem has still to be solved and is under current investigation.

Moreover, following suggestions by Aungier [18], the mean-line model, in order to capture some variable speed effects, should be upgraded at least to a through-flow analysis code, taking into account the streamline variations of the flow variables. This is mainly due to the fact that at high off-design conditions, the flow at peripheral radii (hub and tip) plays an important role in determining overall turbine losses, and a mean-line performance code may give questionable results.

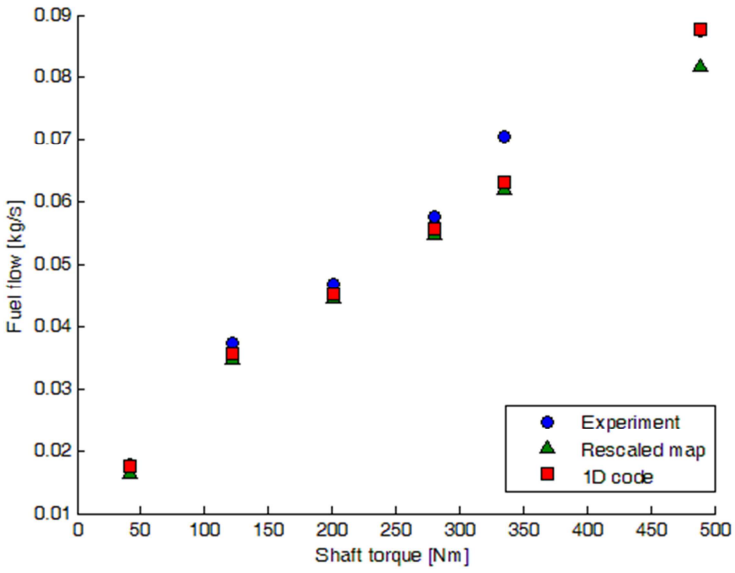

Figure 7.9. TSHAFT engine model validation coupled with TDES model: fuel flow comparison with experimental data and rescaled characteristic map.

7.5 References

[1] A. Bagai, *Aerodynamic Design of the X2 Technology Demonstrator™ Main Rotor Blade*, Presented at the 64th Annual Forum of the American Helicopter Society, International, Montreal, Canada, April 29-May 1, 2008.

[2] D. Walsh, S. Weiner, K. Arifian, T. Lawrence, M. Wilson, T. Millott and R. Blackwell, *High Airspeed Testing of the Sikorsky X2 Technology™ Demonstrator*, Proceedings of the 67th Annual Forum of the American Helicopter Society, Virginia Beach, VA, May 4 2011.

[3] http://raider.sikorsky.com/raider_technology_demonstrator.asp

[4] D. Halley, *ABC Helicopter Stability, Control and Vibration Evaluation of the Princeton Dynamic Model Track*, 29th Forum of the American Helicopter Society, Washington, D.C., May, 1973.

[5] A. Massaro, A. D'Andrea, E. Benini, *Multiobjective-Multipoint Rotor Blade Optimization in Forward Flight Conditions Using Surrogate-Assisted Memetic Algorithms*, Presented at the 37th European Rotorcraft Forum, Gallarate, Italy, Sep. 13-15, 2011.

[6] M. D'Angelo, *Wide speed range turboshaft study*, NASA Contractor Report 198380, General Electric Company,1995.

[7] G. E. Welch, A. B. McVetta, M. A. Stevens, S. A. Howard, P. W. Giel, A. A. Ameri, W. To, G. J. Skoch, and D. R. Thurman, *Variable-Speed Power-Turbine Research at Glenn Research Center*, American Helicopter Society 68th Annual Forum Proceedings, Fort Worth, May 1-3, 2012.

[8] G. E. Welch, 2010, *Assessment of Aerodynamic Challenges of a Variable-Speed Power Turbine for Large Civil Tilt-Rotor Application*, NASA/TM-2010-216758, 2010.

[9] S. S. Chen, *Preliminary Axial Flow Turbine Design and Off-Design Performance Analysis Methods for Rotary Wing Aircraft Engines; II-Applications*, NASA/TM-2009-215651, 2009.

[10] M. Suchezky, G. S. Cruzen, *Variable-Speed Power-Turbine for the Large Civil Tilt Rotor*, NASA TR2011-02-28-0724, 2011.

[11] C. A. Snyder, C. W. Acree, *Preliminary Assessment of Variable Speed Power Turbine Technology on Civil Tiltrotor Size and Performance*, Proc. American Helicopter Society 8th Annual Forum, Fort Worth, Texas, May 1-3, 2012.

[12] F. Bertini, E. Ampellio, M. Marconcini, M. Giovannini, *A Critical Numerical Review of Loss Correlation Models and Smith Diagram for*

Modern Low Pressure Turbine Stages, Proceedings of the ASME Turbo Expo 2013, June 3-7, 2013, San Antonio, Texas, USA.

[13] H. R. M. Craig, H. J. A. Cox, *Performance Estimation of Axial Flow Turbines*, Proc. Inst. Mech. Eng., 71, 1971.

[14] H. Moustapha, M. F. Zelesky, N. C. Baines, D. Japikse, Axial and Radial Turbines, Concepts NREC, White River Junction, Vermont, 2003.

[15] N. Wei, *Significance of Loss Models in Aerothermodynamic Simulation for Axial Turbines*, Doctoral Thesis, Royal Institute of Technology, Stockholm, 2000.

[16] S. C. Kacker, U. Okapuu, *A mean-line prediction method for axial-flow-turbine efficiency*, Journal of Engineering for Gas Turbunies and Power, vol. 108, pp.277-284, April 1982.

[17] VV. AA., *T700-GE-701C Engine Unique Data (A Comparison with T700-GE-700/701 Engines)*, GE Aircraft Engines Student Guide.

[18] R. H. Aungier, *Turbine Aerodynamics: Axial-Flow and Radial-Flow Turbine Design and Analysis*, ASME Press, New York, 2006.

Chapter 8

Conclusions and Future Work

Variable Speed Rotors (VSRs) represent a viable way to considerably reduce fuel consumption in rotorcrafts. Various studies in the open literature and practical implementations, on both helicopter UAVs and tilt-rotors, confirm this statement.

In the present doctoral thesis, VSRs have been thoroughly discussed from a performance standpoint. In addition to the qualitative analysis of the potential benefits, a real case has been simulated, in order to provide quantitative estimations of the fuel consumption reductions achievable in practice.

The present study represents the first attempt in the open literature in which helicopter and turboshaft engine models have been coupled with the aim to understand the operating rotational speed values able to achieve the best VSR performance, not only from the main rotor aerodynamic perspective.

The performance tools needed to adequately simulate coupled helicopter and turboshaft engine operation have been implemented for this purpose. Validation results demonstrate that for the numerical analyses carried out, the approximations applied are reasonable, ensuring a good reliability of the simulation output.

An optimization methodology has been created with the aim to compute the optimal rotational speed able to minimize fuel consumption of the overall main rotor-turboshaft engine system. In a practical implementation, this speed would be achieved by using a more complex control logic which would adjust engine RPM depending on the particular flight condition.

Two different approaches have been analyzed, the FRT and CVT concepts, and their performance results have been compared. Considerable reductions in fuel consumption (almost 13% maximum) have been reported for both FRT and CVT cases with respect to standard constant speed rotor operation, especially at intermediate values of advancing speed (minimum helicopter power condition). At high thrust coefficient values, fuel saving is reduced because optimal rotor speed is found to be very close to the design constant speed value. However, in

these “high and heavy” conditions, it has been found that optimal speed operation allows to extend the helicopter flight envelope, delaying retreating blade stall onset, which instead occurs at constant speed without permitting a realistic trim of the helicopter.

It was found that FRT and CVT fuel savings are comparable for intermediate advancing speeds, but tend to diverge in the hover and high advancing speed regions, where CVT clearly outperforms FRT, with a maximum of 8% better fuel reduction. For the same engine and helicopter configuration, the theoretical maximum fuel saving attainable by the FRT concept is asymptotically defined by CVT performance. However, the CVT concept can represent a valuable alternative to FRTs only if the introduced CVT mechanism is able to preserve state of the art FRT weight and efficiency. In fact, especially at high C_T values, a few percentage points drop in transmission efficiency or even additional weight would imply a higher fuel consumption than with the constant speed case. In any case, no such transmission is currently available for the helicopter requirements; research on the FRT concept, instead, seems to be a more feasible solution to reduce fuel consumption in the short term.

To increase the VSR performance operating with a standard FRT, especially in hover and high speed forward flight, a possible solution may come from a redesign of the free power turbine stages. In the present thesis, a first attempt in the redesign of the GE T700 power turbine has been made, with promising results, which will have to be confirmed by future more accurate analyses.

The model approach presented in this thesis can be employed not only in VSR studies, but also as a useful tool in the preliminary design phase of an entire helicopter, because it is able to assess the goodness of different engine-rotor couplings. In fact, in order to obtain future performance improvements in the rotorcraft field, a continuously growing importance will be given to the optimal integration of the different subsystems inside the helicopter.

The VSR technology, with additional limitations, appears to be readily applicable to helicopters in service nowadays; it is also already employed by some manufacturers, but its application is mainly driven by the goal of reducing noise, not fuel consumption. In fact, in our study it has been found that a reduction in fuel consumption of about 7-8% can be obtained within the ±15% range of the nominal engine speed. By constraining speed variation to this limit, the increase of structural and vibrational problems would be reduced, since the main rotor would be still working very near to its operating envelope. Nevertheless, the

problems eventually arising could be solved by the introduction of composite materials in the airframe and possible active vibration control techniques.

However, to assess the feasibility of the VSR, a more complete and comprehensive analysis of the helicopter, including aeroelastic analysis, must be undertaken, in order to quantify the related vibrational issues. Accuracy should be increased also on the aerodynamic side by introducing a dynamic stall model; in fact, the actual model is capable of predicting retreating blade stall by using airfoil static stall characteristics. It is a conservative estimate which in practice guarantees an acceptable stall margin, since dynamic stall, compared to static stall, is usually encountered at higher angles of attack.

The natural development of this work will be oriented towards a refinement of the current helicopter model. Various interesting research fields extend from the introduction of more complex inflow models to the implementation of dynamic stall characteristics. The need for an aeroelastic model, capable of analyzing the vibrational problems arising when eventually reaching critical speeds, is also mandatory.

It would be also of major importance to study how a main rotor variable speed could affect noise emissions. For instance, noise reduction could be inserted as a secondary goal in a future multi-objective optimization approach.

The need for a deeper research in this particular field, motivated by new regulations on fuel consumption and emissions reduction, is even more supported by the fact that the promising results obtained with these simulations are related to a helicopter design which is not particularly recent. It is true that the results obtained in the present work are specifically valid for the UH-60 helicopter, but there is no reason to think that similar reductions may be difficult to achieve with other helicopter configurations. With innovative helicopter designs, maybe employing wide-speed range power turbines and rotor blades expressly designed for variable speed rotors, the fuel savings achieved could be much higher than those encountered in the present analysis.

Finally, collaboration of different interdisciplinary research groups on this subject is strongly desirable, since both FPT efficiency improvement and innovative CVT design implementation need to employ a diversified set of skills and knowledge.

Appendix: Component Map Interpolation Procedure

A.1 Introduction

Integrating map reading procedures inside gas turbine simulation programs represents one of the key points to correctly predict engine off-design performance. In fact, the majority of problems in developing an adequate gas turbine simulation model are related to inaccuracies in the prediction of component characteristics [1].

Because of its technical and physical features, the most challenging component to simulate is the axial compressor. Turbine map interpolation is a simpler task because it can usually be performed with simple bilinear interpolation. When gridded data is not available, some concepts valid for compressor maps could also be used for turbines. However, in the vast majority of their operational life, gas turbines operate in choked conditions, so that turbine performance prediction results in a simpler task to be managed. For this reason, in the subsequent part of this appendix we will only treat compressor interpolation problems, since they are much more important for the scope of overall engine performance prediction accuracy. The stability of an off-design performance simulator strongly depends on the method used to interpolate compressor maps. Usually, axial compressor and turbine characteristics found in literature are obtained from experimental data by measuring the values of pressure ratio and corrected mass flow at constant rotational speed lines; isentropic efficiency is also measured at the same points. Eqs. (1.66)-(1.69) represent a formal definition of the four variables used in the construction of performance maps. Once tabulated, these values are the data source used to draw component maps. Every operational point on a traditional compressor map is determined by the knowledge of only two of these four variables: this means that the remaining quantities have to be determined by finding a relationship with the former. This holds true only if the effects of Reynolds number, working fluid changes, variable geometry, inter-stage bleeds, flow distortions, volume packing and heat transfer are neglected [2].

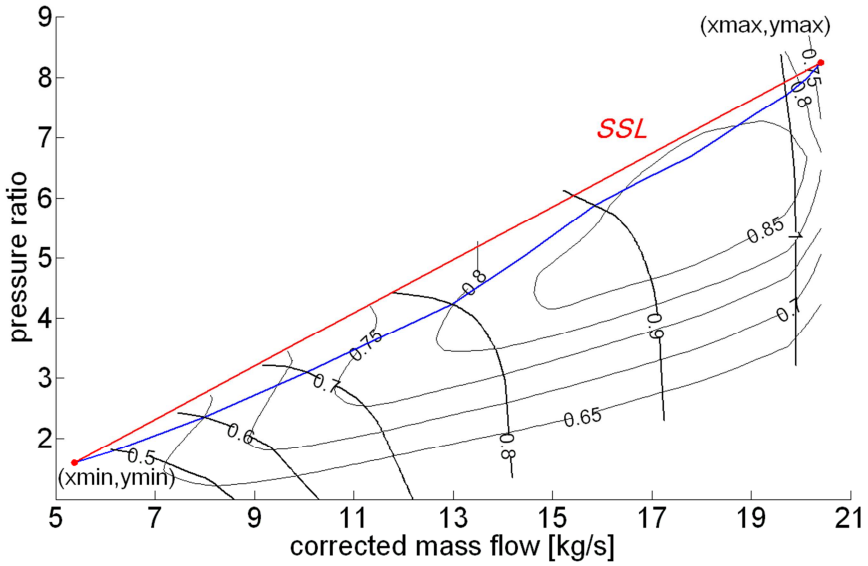

Figure 8.1. Axial compressor map: Straight Surge Line (SSL), a map construction parameter, is in red, whereas the surge line is in blue.

Due to the shape of compressor maps (see Figure 8.1 as example), potential troubles encountered in compressor map interpolation are [3]:

1. Nonuniqueness: in choosing the two variables to define the operating point, it is necessary that the variables are not collinear and that each pair of variables produces a unique operating point [2]. This property in general does not hold for any combination of the four variables tabulated in a usual compressor map.
2. Ill-conditioning: small changes in one variable may produce large changes in the other free coordinate variable (e.g. small mass flow variations imply large variations in pressure ratio near the choking condition).
3. Inaccurate knowledge of low speed operating conditions: when spool speed is extremely low, a compressor can behave as a stirrer (temperature rises, pressure drops) or as a turbine, in conditions such as windmilling (temperature and pressure drop). Under these particular conditions, isentropic efficiency is no more usable as a map variable because it reaches a discontinuity when the pressure rise is zero. Instead of using efficiency to define the relationship between work input and pressure ratio, other variables, such as temperature or enthalpy rise (or even temperature ratio), should be used [2],[4].

The most common approach to solve the first two above-mentioned problems is using auxiliary coordinates [5],[6]. An additional parameter (usually named β), without any specific physical meaning, is introduced, so that the two variables

which define completely any operating point become corrected speed and β. One of the advantages in using β is the possibility to interpolate on a rectangular domain.

Several methods have been recently developed which do not employ the β parameter. For a more thorough description of these unconventional approaches, see Ref. [7]. However, even if some of these methods seem to be competitive, β parameter utilization is still the most diffused interpolation method in gas turbine simulation programs mainly because of its simplicity and reliability. One of the reasons is given by the fact that β is used as a variable in performance calculations to avoid convergence problems. In fact, the stability of the Off Design performance simulator strongly depends on the definition of β and the question arises on how it influences the simulation results. In his gas turbine simulation program, Kurzke [5] suggests utilization of parabolic β lines, while the software implemented at NLR uses oblique lines with a slope similar to the average slope of the surge line. In the two preceding methods every single β line is a different univariate function. Since it is necessary to apply a numerical procedure to calculate intermediate β values, this approach can be defined "numerical", in contrast to a more complex definition of β as a multivariate function, which will be further called "analytical". An analytical method for β parameter definition has been implemented inside TSHAFT. Beta hereafter is defined as a multivariate analytical function of both the corrected mass flow and pressure ratio, while the shape of the β lines, instead of being fixed, can be modified by the user simply adjusting four variable parameters. The advantages of an analytical definition rely on having the possibility to rapidly calculate β values in every point of the map. An example of application is the possibility to calculate an estimate of the interpolation error in a very simple way. Furthermore, based on this estimate, the analytical and adjustable nature of β permits to choose automatically a particular shape that locally minimizes the interpolation error. The reason for this formulation is:

1. to reduce the need for human input in the fitting process;
2. to provide the user a quantitative tool to distinguish the quality of different interpolations performed with different shapes of the β function.

Within TSHAFT, a traditional scaling procedure is applied. First the scaling factors are derived from comparison between real Design Point and the one given by the original map and then the scaled map can be obtained by multiplying the

derived scaling factors with the Off Design point map data of the original performance maps.

A.2 The Beta Function

In the present method β is built analytically as a function of two real variables $\beta=f(x,y)$, where x is the pressure ratio and y the corrected mass flow. The main advantage of an analytical approach lies mainly in the possibility to calculate an accurate value of β at any time, once pressure ratio and corrected mass flow are known. This also allows for a simple estimation of the interpolation error.

Two types of functions are implemented: one (linear) that can be used for the majority of cases, and another one (composite) to be employed where the particular shape of the maps does not allow the former to achieve acceptable results. In the following a description of the two different types is given.

A.2.1 Linear β

The β function is simply a plane which cuts the xy plane at an angle so that its contour $\beta=1$ is almost coincident with the surge line. To this purpose, such line is defined using the following:

$$y = m_{surge}\,x + q_{surge} \tag{A.1}$$

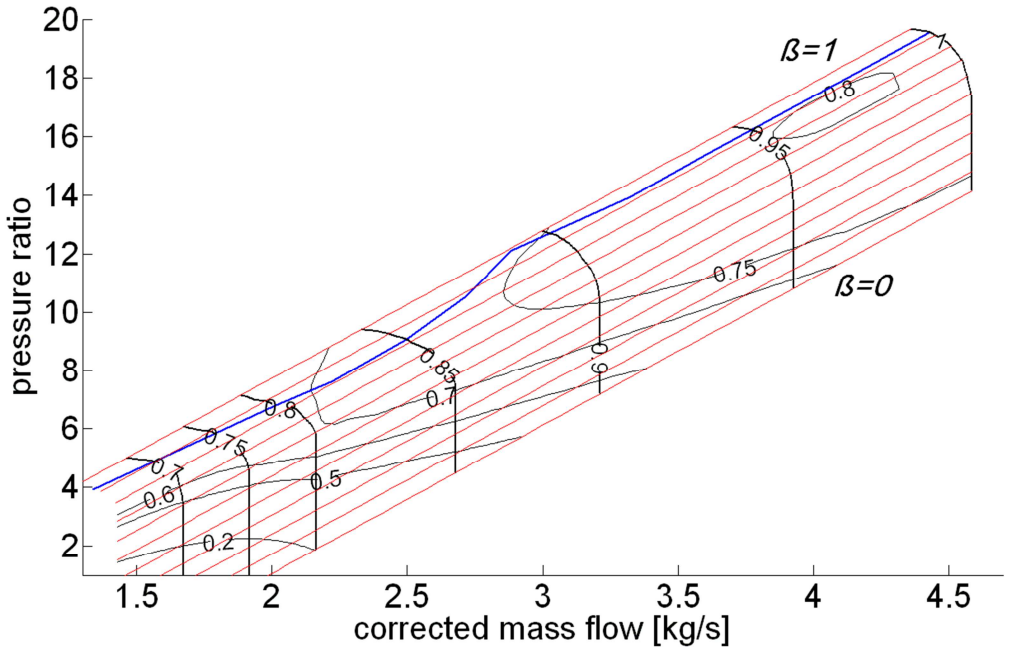

Figure 8.2. Linear method for β function (β lines in red).

The slope m_{surge} and the ordinate q_{surge} of this line, which for convenience will be called "straight surge line" (SSL) are visible in Figure 8.1 (in the previous section), and can be derived as follows:

$$m_{surge} = \frac{y_{\max} - y_{\min}}{x_{\max} - x_{\min}} \tag{A.2}$$

$$q_{surge} = y_{\min} - m_{surge} x_{\min} \tag{A.3}$$

where x and y are referred to the two extreme points of the surge line. An example of a β function built in this way is shown in Figure 8.2.

A.2.2 Composite β

The β function is composed of two parts, one radial and the other tangential. The idea is to build a function that is the sum of two functions with the following properties: the first must have radial contour lines, the second circular contours. In Figure 8.3, the idea behind this type of construction can be better understood.

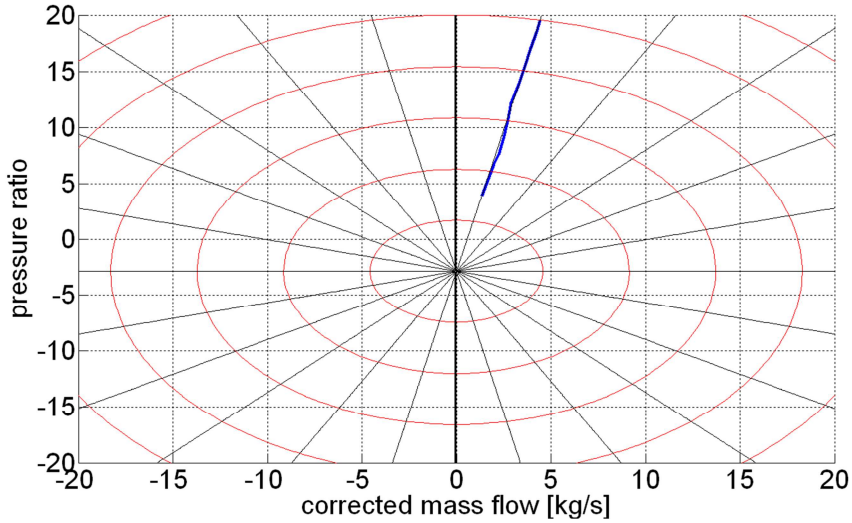

Figure 8.3. β function construction in Composite mode (surge line in blue, radial part in red, tangential in black).

Through the adjustment of four parameters (line density *n*, translation *p*, curvature *c*, initial angle *a* for $\beta=0$) it is possible for the user to change the arrangement of the β lines properly, having more degrees of freedom than with the linear method. To meet the required properties, $f(x,y)$ should be constant along

each line coming out from a center C; for all the points belonging to one of these lines the slope *m* calculated with reference to C is constant:

$$m = \frac{y - y_C}{x - x_C} \tag{A.4}$$

This is a possible β function: in fact, if β is defined in the same way as *m* above, it will have radial contour lines. To make it a little more suitable to our purpose, the parameters *p*, *n*, m_0 are added, ensuring that the line $\beta=1$ is coincident with the SSL for $p=1$:

$$\beta_{rad} = p\left(\frac{\frac{y - y_C}{x - x_C} - m_0}{m_{surge} - m_0} \right)^n \tag{A.5}$$

This function is centered in C. Note that m_0 is the initial slope for $\beta=0$. The parameter *a*, which must be entered by the user, is the angle corresponding to the line $\beta=0$, so we have $m_0=tan(a)$. The parameter *n*, being an exponent, is responsible for curve density, and *p* is used to adjust the line $\beta=1$.

The above mentioned method is characterized by a particular behavior, which is here referred to as line thickening: as the slope of the contour lines increases, the same happens for their density in the map. It is obvious that β, being essentially a measure of the slope, between 45° and 90° passes from the unit value towards infinity; so, if the SSL slope is high, there will be a high concentration of β lines in the neighborhood of the unit value. This possibility may be more or less desirable depending on the case. It may be positive, since it allows a higher concentration of β lines in the area around the operating line. It can be negative, when a very large number of β lines is needed in order to obtain an acceptable interpolation in areas far from the operating line (e.g. in a transient analysis).

An attenuation of this behavior can be achieved by normalizing data on the two axes or, alternatively, by using the Arctan method, in which:

$$\beta_{rad} = p\left(\frac{\arctan\left(\frac{y - y_C}{x - x_C} \right) - a}{\arctan\left(m_{surge} \right) - a} \right)^n \tag{A.6}$$

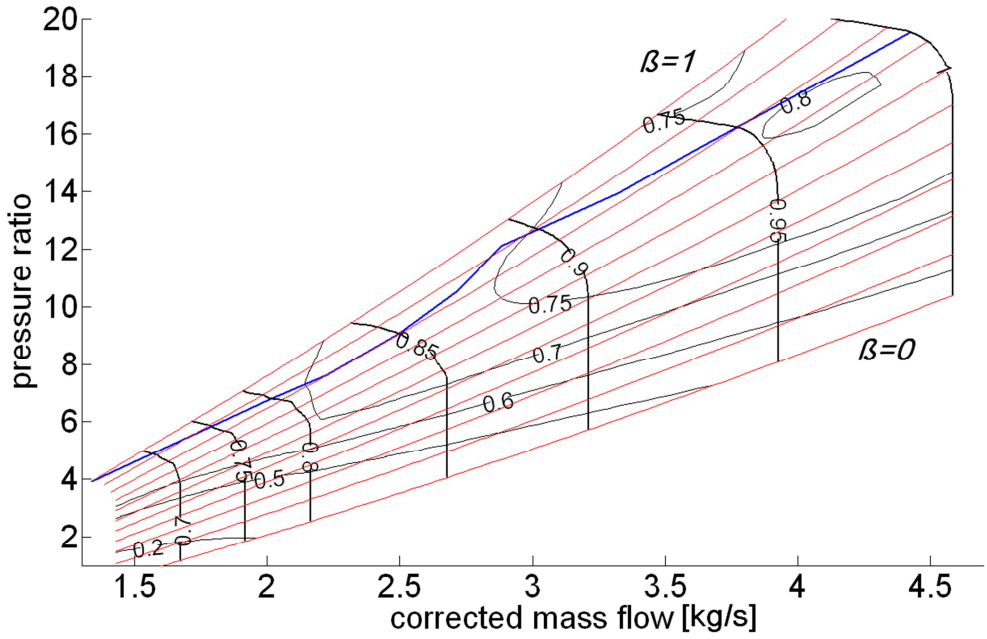

Figure 8.4. Composite method for the β function with $n=3$, $p=0.93$, $c=0.35$, $a=60°$.

In this case, when $a \neq 0$, the β lines undergo a pure rotation without line thickening. In addition, due to all lines being equally spaced in the angular direction, there will not be any line thickening along with increasing inclination.

Let us now analyze the tangential part. This is introduced to provide a curvature to the β function when required by the user. A function $f(x,y)$ with circular contour lines is needed and it is evident that a possible function to perform this task is a paraboloid centered in C:

$$f(x,y) = (x - x_C)^2 + (y - y_C)^2 \tag{A.7}$$

It is convenient to normalize the function to force its maximum values to be less than or equal to unity inside the map. So, the radius connecting C to the end upper point of the surge line is chosen as the reference length, and β_{tan} consequently becomes:

$$\beta_{tan} = \frac{\sqrt{(x - x_C)^2 + (y - y_C)^2}}{\sqrt{(x_{\max} - x_C)^2 + (y_{\max} - y_C)^2}} \tag{A.8}$$

The use of square root linearizes the increase in β_{tan} along the radial direction (in fact, the function becomes a cone). Finally, the complete definition of the composite β function is:

$$\beta = \beta_{rad} - c\beta_{\tan} \tag{A.9}$$

where c is a curvature parameter, entered by the user, which determines the higher or lower influence on β of the tangential part. An example of a line construction using the composite method is given in Figure 8.4.

A.3 Interpolation

In order for the β lines to be correctly set up, they must intersect the speed lines; to this purpose, first a 1D interpolation of each speed line is needed for all the corrected speed regimes, N_{corr}. This preliminary operation requires a parametric interpolation as a function of a non-dimensional value t to avoid non-uniqueness (well represented in Figure 8.5).

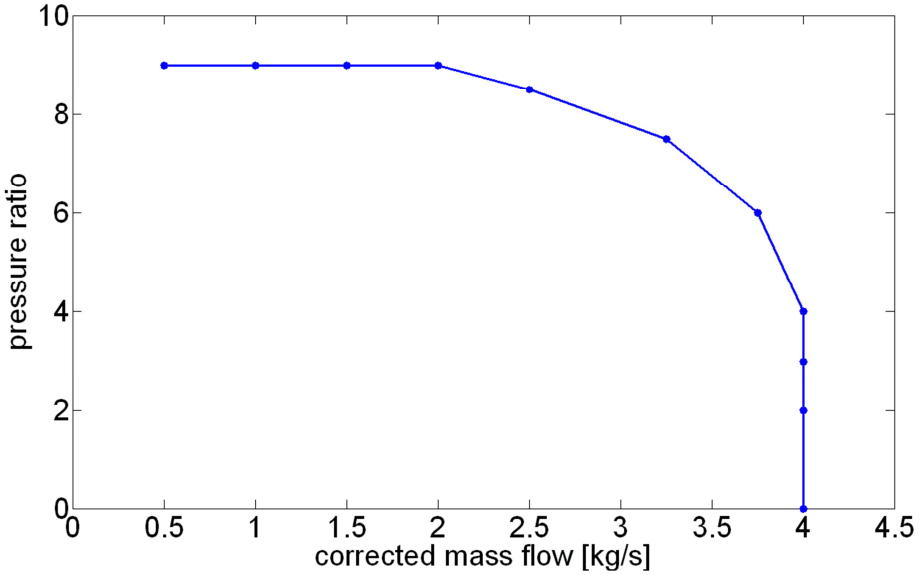

Figure 8.5 Nonuniqueness example in the choice of the interpolation variables: neither pressure ratio or corrected mass flow can be used as the independent variable. The former cannot be employed near the surge region, the latter in choking conditions.

The same procedure is to be implemented also on the actual compressor efficiency so that a single value of t identifies one unique value for the three quantities m_{corr}, r_{comp} and η_{comp}, i.e. corrected mass flow, pressure ratio and efficiency. These become real functions of t:

$$\begin{cases} m_{corr} = x = p_1(t) \\ r_{comp} = y = p_2(t) \\ eff = p_3(t) \end{cases} \tag{A.10}$$

where p_1, p_2 and p_3 are polynomials created by an interpolation routine. Note that if the experimental data are noisy, it is better to elaborate a smoothing procedure of the same data before performing interpolation.

Now the intersection points between beta and speed lines have to be calculated. While the speed lines are in a fixed number v, because they have been already defined earlier by map data, the β lines, as contour lines of an analytic function, are virtually infinite. It is a user's task to choose the number λ of β lines required to calculate the intersection points used in the subsequent 2D interpolation. In the method, $\beta=0$ is set as the first line of intersection, and then all the lines that are multiple of the value $1 / (\lambda-1)$ up to the top β line ($\beta=1$) are used. The β lines assigned for interpolation are chosen only in the range $0 \leq \beta \leq 1$: all external values, whether they may have to be calculated, are extrapolated. This forces the user to construct a function possessing β values between 0 and 1 for the entire range of m_{corr} and r_{comp} of interest, since the interpolation accuracy is far superior to that of extrapolation.

It seems quite obvious that a large number of β lines can ensure greater accuracy; however, beyond a certain λ no major improvements are obtained. Once the number of β lines is decided, the calculation of the intersection points is performed. For each speed line the λ intersection points with the selected β lines are computed by solving the following system:

$$\begin{cases} \beta\big(x(t), y(t)\big) = \beta_0 \\ x = p_1(t) \\ y = p_2(t) \end{cases} \tag{A.11}$$

This system can be solved numerically. The solution obtained is one specific value of t. This value, substituted in the interpolating polynomials p_1, p_2 and p_3, permits the calculation of the values of m_{corr}, r_{comp} and η_{comp} for each point of intersection.

Once the system for all speed lines is solved, a new set of data is obtained, which can be distributed on a regular grid, formed by all the $v \times \lambda$ couples (β, N_{corr}). For each point of this grid all the values of the quantities m_{corr}, r_{comp} and η_{comp} are known: finally it is possible to implement three different 2D interpolations on the domain of the two variables (β, N_{corr}). Linear interpolation can be adopted, but also higher order approximations can be used.

A.4 Interpolation Error

A criterion for choosing the best method of interpolation is here addressed together with how to determine the good rules for building a β function that minimizes the interpolation error. For this purpose, a quantitative method is developed to determine *a priori* a valid estimate of the interpolation error. The following metric indexes are used:

1) Maximum absolute error: for each m_{corr}, r_c and η_{comp} it identifies the point of maximum absolute deviation (may be three different points) between measured and interpolated values;
2) Maximum relative error: for each m_{corr}, r_c and η_{comp} it identifies the point of maximum relative deviation between actual and interpolated values. For example, for m_{corr} we have:

$$err_{max-rel} = \frac{\left| m_{corr-real} - m_{corr-interp} \right|}{m_{corr-real}} \quad \text{(A.12)}$$

3) Mean relative error: for each m_{corr}, r_c and η_{comp} it calculates the average of the relative deviation values between measured and interpolated values.

The two global relative errors, mean and maximum (calculated over all the values of m_{corr}, r_{comp} and η_{comp}), represent a quantitative indication of the quality of the type of interpolation used. These errors provide a valid measure of the interpolation accuracy, which can be used to compare different methods.

A.5 Interpolation Error Minimization

To simplify the choice of a correct β function, an optimization method is introduced in the present method to find the interpolation parameters which locally minimize the mean interpolation error using a Sequential Quadratic Programming (SQP) algorithm. This procedure is also supported by the fact that interpolation error minimization, either mean or maximum, as previously seen, is of utmost importance to perform a good performance simulation. The mean error can be expressed as a function of all the previous cited curve parameters (*n*, *m*, *p*, *a*). It is clear that such an algorithm cannot guarantee the achievement of a global minimum. In fact, this procedure is better used to optimize the β function shape when a reasonable starting set of parameters is defined, otherwise sometimes it could lead to incorrect results, which by the way can always be detected through a visual observation of the map output.

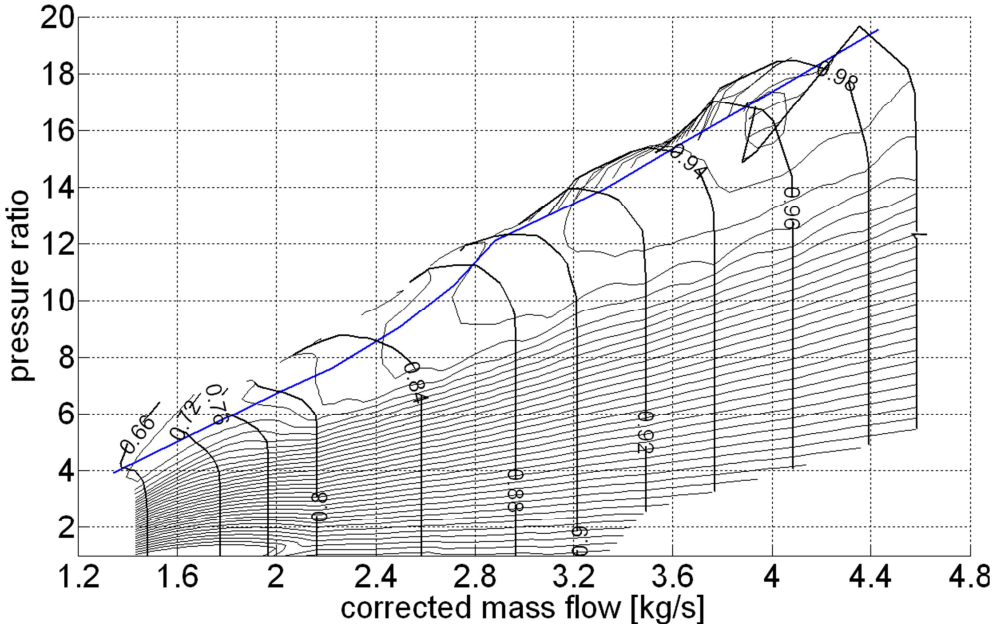

Figure 8.6. Example of map built with a very bad initial curve parameter set.

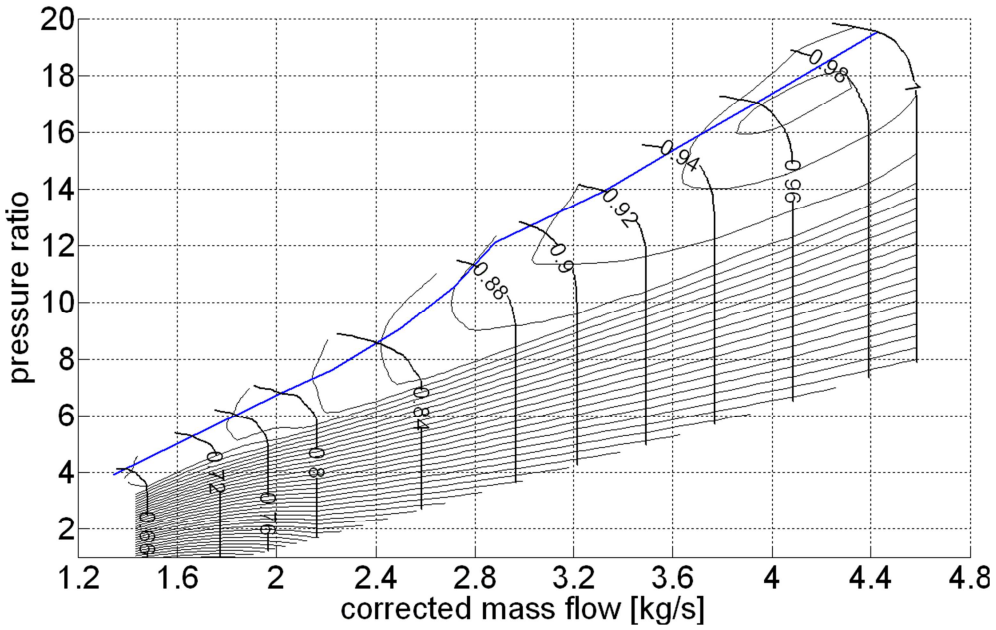

Figure 8.7. Final map resulted from interpolation error minimization. Note that the same experimental points of Figure 8.6 are used.

Nevertheless, the abovementioned minimization routine is useful not only to locally optimize a particular parameter set, but also to provide a reasonable set of curve parameters starting from a very bad initial set. To assess the power and the limitations of this method, in Figure 8.6 an extremely inaccurate initial map output is created using the Composite method. Executing the minimization routine

leads to the map output of Figure 8.7; since the maximum error changes from over 100% to 0.823% and the overall mean error from 3.295% to 0.058%, the new parameter set represents a consistent improvement compared to the previous one. What is of particular interest in the future development of the optimization routine is the possibility to implement a more complex minimization function, capable to take into account other important criteria, (those outlined in the introduction), not only the mean interpolation error. Remember that experimental data is always affected by measurement uncertainty and sometimes an interpolated map which minimizes the interpolation error is not always the best choice for the engineer. However, to make a further step towards automation in compressor map interpolation, it is necessary to quantify adequately every single criterion.

A.6 References

[1] M. Orkisz, S. Stawarz, *Modeling of Turbine Engine Axial-Flow Compressor and Turbine Characteristics*, Journal of Propulsion and Power, Vol. 16, No. 2, March-April 2000.

[2] G. Jones, P. Pilidis, B. Curnock, *Compressor Characteristics in Gas Turbine Performance Modelling*, Proceedings of ASME Turbo Expo 2001, June 4-7 2001, New Orleans.

[3] A. M. El Gammal, *An algorithm and Criteria for Compressor Characteristics Real Time Modeling and Approximation*, Journal of Engineering for Gas Turbines and Power, Vol. 113, January 1991

[4] C. Riegler, M. Bauer, J. Kurzke, *Some Aspects of Modeling Compressor Behavior in Gas Turbine Performance Calculations*, Journal of Turbomachinery, Vol. 123, April 2001

[5] J. Kurzke, *How to get component maps for aircraft gas turbine performance calculations*, ASME paper 96-GT-164, Birmingham 1996.

[6] P.P. Walsh and P. Fletcher, *Gas Turbine Performance*, Blackwell Publishing, 2004.

[7] G. A. Misté and E. Benini, *Improvements in Off Design Aeroengine Performance Prediction Using Analytic Compressor Map Interpolation*, International Journal of Turbo & Jet-Engines, Vol. 29, No. 2, ISSN (Online) 2191-0332, ISSN (Print) 0334-0082, DOI: 10.1515/tjj-2012-0012, May 2012.